CENTRO DE INVESTIGACIONES
EN ÓPTICA, A.C.

EXPERIMENTAL STUDY OF THE GENERATION OF HIGH-ENERGY NOISE-LIKE PULSES AND THEIR APPLICATION TO SUPERCONTINUUM GENERATION

DOCTORADO EN CIENCIAS (ÓPTICA)

Asesores: ***Dr. Olivier Pottiez***

Dr. Juan Carlos Hernández García

Estudiante: ***M.C. Jesús Pablo Lauterio Cruz***

– Versión definitiva. Incluye cambios sugeridos por revisores. –

Vo. Bo. Asesor	Vo. Bo. Co-asesor	22 de septiembre de 2017
		Fecha

Septiembre de 2017
León, Guanajuato, México

Experimental Study of the Generation of High-energy Noise-like Pulses and Their Application to Supercontinuum Generation

by

Jesús Pablo Lauterio-Cruz, M.Sc.

A thesis submitted in partial fulfillment of the requirements
for the degree of

Doctor of Philosophy in Optical Sciences

Advisor: Dr. Olivier Pottiez

Co-advisor: Dr. Juan Carlos Hernández-García

Centro de Investigaciones en Óptica, A.C.
Loma del Bosque 115, León, Guanajuato 37150, México

September 29, 2017

The research presented in this thesis was carried out at the Centro de Investigaciones en Óptica A.C. (CIO), in collaboration with the División de Ingenierías Campus Irapuato–Salamanca, Universidad de Guanajuato (DICIS-UG). Funding was provided by the Consejo Nacional de Ciencia y Tecnología, México (CONACyT): through the scholarship 209564; by "Fronteras de la Ciencia" program (grant 471) and "Ciencia Básica" project 253925 at CIO; "Ciencia Básica" project 257691 and Cátedras CONACyT project 3155 at DICIS-UG.

Abstract

In this research work we obtained experimentally very wide and flattened supercontinuum (SC) spectra using noise-like pulses (NLPs) as pump in standard single-mode fiber (SMF, non-zero dispersion at 1550 nm, low nonlinear coefficient). NLPs were produced by two different configurations of all-fiber figure-eight lasers (F8Ls). On the one hand, we demonstrated experimentally (this was confirmed by our simulations) that NLPs allow SC generation even with moderate input powers (few tens of mW) in long lengths of fiber not optimized for this purpose like the SMF, since the nonlinear processes integrate over long lengths and are still operating and widening the spectrum even after hundreds of meters; besides, adding a piece of high-nonlinearity fiber (HNLF), optical spectra covering about 1000 nm with a very good flatness and a very high dynamic range were produced. On the other hand, we obtained record pulse energies as high as 300 nJ in a scheme where the polarizing element is absent; without a strict polarization control, NLPs could avoid pulse splitting when pump power is increased, generating a SC of more than 200 nm directly at the laser output. In addition, by increasing the harmonic mode locking (HML) order and extending the length of the cavity, we were able to flatten the spectrum to less than 3 dB over 160 nm. These results show that NLPs could be useful to develop cheap SC light sources for diverse applications like optical coherence tomography (OCT) or optical device testing; such sources would compare favorably to others that require expensive laser diodes or photonic crystal fibers, increasing the cost.

Keywords: noise-like pulses, supercontinuum generation, figure-eight laser.

A mi madre

Sin ti

no sería quien soy.

Sin ti

no estaría donde estoy.

Acknowledgments

I am very grateful to my advisor, Dr. Olivier Pottiez, for all his teachings, patience and infallible guidance: no student could ask for a more diligent advisor. I thank very much to Dr. Juan Carlos Hernández García, my co-advisor, for all his support, and for all his time and dedication, especially when I was taking my first steps. I also thank Dr. Yazmin Bracamontes Rodríguez for all her valuable advice and technical support.

I am grateful to the members of my pre-doctoral and doctoral committees: Dr. Yuri Barmenkov, Dr. Alejandro Martínez, Dr. David Monzón, and Dr. Evgeny Kuzin (from INAOE); their experience, comments and suggestions were invaluable for this work. I am very grateful to Dr. Francisco Villa and Dr. Amalia Martínez for his friendship, time and understanding. I thank to all the researchers who directly or indirectly were part of my training. And I also thank the administrative and technical CIO staff for their valuable service.

I thank my friends and my colleagues at the CIO, for those talks, recreation and learning. And I thank each and every one of my friends at DICIS-UG, for generating an excellent environment in the laboratory and also outside of it. I also thank Dr. Julian Estudillo and Dr. Roberto Rojas for their valuable assistance.

I am very grateful to the CONACyT for the economic support provided in these four years through the doctoral scholarship 209564 and to the CIO, for its infrastructure and necessary resources to carry out this research work.

I thank my mother, Paulina, and my sister, Ana Paulina, for their concern and care, and for the endless love and support that they have given me throughout the years.

Last but not least, I thank my wife and life partner Mariana, for her love, great patience, support in hard times and her kilos of encouragement since we started this adventure called *Doctorate*.

Contents

List of Figures

List of Acronyms

As assistance to the reader, the following list of acronyms used in this thesis is included.

Acronym	**Term**
ASE	amplified spontaneous emission
a.u.	arbitrary units
ccw	counter-clockwise
cw	clockwise
CW	continuous wave
DCF	dispersion compensating fiber
DF	doped fiber
DFWM	degenerate four-wave mixing
DSR	dissipative soliton resonance
EDF	erbium-doped fiber
F8L	figure-eight laser
FL	fiber laser
FWHM	full-width at half-maximum
FWM	four-wave mixing
GNLSE	general nonlinear Schrödinger equation
HML	harmonic mode locking
HNLF	high-nonlinearity fiber
HOS	higher-order solitons
HWR	half-wave retarder
ISO	optical isolator
MI	modulation instability

ML	mode locking
NALM	nonlinear amplifier loop mirror
NLP	noise-like pulse
NLSE	nonlinear Schrödinger equation
NOLM	nonlinear optical loop mirror
NPE	nonlinear polarization evolution
NPR	nonlinear polarization rotation
OCT	optical coherence tomography
OSA	optical spectrum analyzer
PC	polarization controller
PCF	photonic crystal fiber
PI-ISO	polarization-independent isolator
PMF	polarization-maintaining fiber
PML	passively mode locked
POL	optical polarizer
QWR	quarter-wave retarder
RK4IP	fourth-order Runge–Kutta in the interaction picture (method)
SA	saturable absorber
SC	supercontinuum
SFS	self-frequency shift
SMF	single-mode fiber (standard fiber)
SPM	self-phase modulation
SRS	stimulated Raman scattering
SSF	split-step Fourier (method)
SWH	significant wave-height
USP	ultrashort pulse
VWR	variable-wave retarder
WDM	wavelength-division-multiplexing (coupler)
XPM	cross-phase modulation

List of Publications

During the present research work, the articles cited below, sorted by date, were published. At the end of each one, the corresponding reference in the present thesis is shown.

1. O. Pottiez, H. Ibarra-Villalón, Y.E. Bracamontes-Rodríguez, E. García-Sánchez, J.P. Lauterio-Cruz, J.C. Hernandez-Garcia, M. Bello-Jimenez and E.A. Kuzin, "Soliton formation from a noise-like pulse during extreme events in a fibre ring laser", *Laser Phys. Lett.* **14**, 105101 (2017). Ref. [9]

2. J.P. Lauterio-Cruz, O. Pottiez, Y.E. Bracamontes-Rodríguez, J.C. Hernández-García, E. García-Sánchez, M. Bello-Jimenez and E.A. Kuzin, "Comparative study of supercontinuum generation using standard and high-nonlinearity fibres pumped by noise-like pulses", *Laser Phys.* **27**, 65107 (2017). Ref. [17]

3. Y.E. Bracamontes-Rodríguez, O. Pottiez, E. García-Sánchez, J.P. Lauterio-Cruz, H.E. Ibarra-Villalón, J.C. Hernández-García, M. Bello-Jiménez, G. Beltrán-Pérez, B. Ibarra-Escamilla and E.A. Kuzin, "Dual noise-like pulse and soliton operation of a fiber ring cavity", *J. Opt*. **19**, 35502 (2017). Ref. [57]

4. J.C. Hernández-García, J.M. Estudillo-Ayala, O. Pottiez, J.D. Filoteo-Razo, J.P. Lauterio-Cruz, J.M. Sierra-Hernandez and R. Rojas-Laguna, "Flat super-continuum generation by a F8L in high-energy harmonic noise-like pulsing regime", *Laser Phys. Lett*. **13**, 125104 (2016). Ref. [55]

5. E. Garcia-Sanchez, O. Pottiez, Y.E. Bracamontes-Rodriguez, J.P. Lauterio-Cruz, H.E. Ibarra-Villalon, J.C. Hernandez-Garcia, M. Bello-Jimenez and E.A. Kuzin, "Complex dynamics of a fiber laser in non-stationary pulsed operation", *Opt. Express* **24**, 18917 (2016). Ref. [7]

6. E. García-Sanchez, O. Pottiez, Y.E. Bracamontes-Rodríguez, J.P. Lauterio-Cruz, H.E. Ibarra-Villalón, J.C. Hernández-García, M. Bello-Jiménez, and E.A. Kuzin, "A temporal insight into the rich dynamics of a figure-eight fiber laser in the noise-like pulsing regime", *Laser Phys. Lett.* **13**, 105106 (2016). Ref. [53]

7. J.P. Lauterio-Cruz, J.C. Hernández-García, O. Pottiez, J.M. Estudillo-Ayala, E.A. Kuzin, R. Rojas-Laguna, H. Santiago-Hernández and D. Jauregui-Vazquez, "High energy noise-like pulsing in a double-clad Er/Yb figure-of-eight fiber laser", *Opt. Express* **24**, 13778 (2016). Ref. [4]

8. H. Santiago-Hernández, O. Pottiez, M. Duran-Sanchez, R.I. Alvarez-Tamayo, J.P. Lauterio-Cruz, J.C. Hernández-García, B. Ibarra-Escamilla and E.A. Kuzin, "Dynamics of noise-like pulsing at sub-ns scale in a passively mode-locked fiber laser", *Opt. Express* **23**, 18840 (2015). Ref. [6]

In addition, the following conference papers were also published.

9. Y.E. Bracamontes-Rodriguez, O. Pottiez, H. Ibarra-Villalón, J.P. Lauterio-Cruz, B. Ibarra-Escamilla and E.A. Kuzin, "Simultaneous emission of noise-like pulse and solitons from a fiber laser", in *OSA Frontiers in Optics* (2017), p. JTu3A.103.

10. J.P. Lauterio-Cruz, J.C. Hernández-García, J.M. Estudillo-Ayala, O. Pottiez, R. Rojas-Laguna, J.D. Filoteo-Razo, L.F. Samano-Aguilar and D. Jauregui-Vazquez, "Numerical analysis of the supercontinuum spectrum generation in a couple of photonic crystal fibers with different structure by using the RK4IP method", in *Proc. of SPIE* (2016), p. 97431I.

11. L.F. Samano-Aguilar, J.C. Hernandez-Garcia, J.M. Estudillo-Ayala, R. Rojas-Laguna, O. Pottiez, J.D. Filoteo-Razo, J.P. Lauterio-Cruz and D. Jauregui-Vazquez, "Highly Efficient Self-Q-Switched Erbium-Ytterbium Fiber Laser Operating at High Output Powers", in *OSA Frontiers in Optics* (2016), p. JTh2A.32.

12. F.J. Valle-Atilano, J.M. Estudillo-Ayala, J.D. Filoteo-Razo, J.C. Hernández-Garcia, J.P. Lauterio-Cruz, D. Jáuregui-Vázquez, B. Ibarra-Escamilla, R. Rojas-Laguna, O. Pottiez and E.A. Kuzin, "Polarization study of a supercontinuum light source for different wavelengths through a photonic crystal fiber", in *Proc. of SPIE* (2016), p. 973115.

Chapter 1. Introduction

Passively mode locked fiber lasers (PML-FL) are simple, compact and low-cost sources that have long been studied for the production of a wide variety of optical pulses like conservative solitons, dispersion-managed solitons, similaritons, dissipative solitons, dissipative soliton resonance (DSR) pulses and noise-like pulses (NLPs), due to their significance in scientific research and industry.

In particular, the study of NLPs, reported for the first time since two decades ago [1], has attracted much attention in recent years due to their distinctive features, such as being highly energetic [2–4] and displaying a wide optical spectrum; but also, presenting a quite stable global behavior on large time scales, but at the same time showing a chaotic behavior at the local level as they are formed by thousands of ultrashort pulses (fs-ps) [5], which makes that this regime is considered by many authors as partial or incomplete mode locking. Nonetheless, the properties of these pulses allow the study of some less stationary regimes [6,7] including the study of extreme optical events [8,9]. In addition, due to the behavior already mentioned, the development of diverse applications in the fundamental mode locking operation has also been carried out; for instance, low-coherence spectral interferometry [10], materials processing [11], sensing [12], bio-imaging [13], and supercontinuum (SC) generation [4,14–17]. In the latter topic, the use of NLPs as pump to generate very broad and flat spectra has been promoted by several researchers motivated by the need to improve supercontinuum sources in terms of efficiency and low cost.

In the particular framework of SC generation, where narrowband optical signals undergo a broad spectral widening as a result of the combination and interaction of multiple nonlinear optical phenomena [18], NLPs offer some advantages over ultrashort pulses (USPs) and conventional ns-long pulses. In particular, it is well known that in a dispersive medium, an USP disperses very quickly and its peak power vanishes which causes the early extinction of nonlinear effects. Hence, SC

generation with these pulses requires that the nonlinear spectral widening occur over a very short initial distance in the material, requiring fibers with high nonlinear coefficient and specially adapted dispersion properties, such as photonic crystal fibers (PCF) [19], which are generally very expensive. In contrast, despite their fine internal structure (sub-ps), NLPs are very long so they do not disperse rapidly and their peak power remains high over long distances; therefore, nonlinear effects are integrated over much longer fiber lengths, allowing SC generation even in fibers whose nonlinear and dispersive properties are not optimized for this purpose, such as standard single-mode fiber (SMF) [17], as it is shown in the present thesis. On the other hand, conventional ns-pulses undergo spectral broadening initially driven by modulation instability (MI), which progressively transforms the long pulse into a packet of USPs [19]; in general terms, this fragmentation stage is omitted when NLPs are used, because from the beginning there is a packet of USPs with a large spectral width. Besides, the spectrum flatness of conventional ns-pulses is usually reduced by the presence of a pronounced peak of residual pump and the required input peak power usually scales as a few kW [20]. Another advantage of NLPs over other PML pulses is their high energy per pulse: about 1000 times more than that of a soliton [2–4], which is important in the frame of SC generation, because a SC once generated can hardly be amplified without drastically reducing the bandwidth.

On the other hand, in addition to experimental works on SC generation, numerical studies have been carried out by using different pulses as pump [21,22] either to better understand the nonlinear processes involved or to propose better broadband sources, by modeling the pulse propagation in optical fiber solving numerically the nonlinear Schrödinger equation (NLSE) or its general form (GNLSE). For such purpose some numerical methods have been developed, including the Split-Step Fourier (SSF) [23], the Runge–Kutta (RK) scheme introduced by Blow and Wood [24], some variants of them, and the Fourth-Order Runge–Kutta in the Interaction Picture (RK4IP) method [25,26]. Although the latter was originally developed to model the Gross–Pitaevskii equation [27], which describes the dynamics of Bose–Einstein condensates, due to its similarity with the GNLSE, the algorithm was applied

for propagating a pulse in optical fibers, placing the time and space variables in opposite roles. Nonetheless, in spite of the benefits offered by all these methods, very few works using them for modeling SC generation have been published, being even much less the amount of literature that focuses on the use and study of NLPs.

In an attempt to fill the gap, in the present thesis, NLPs were achieved both experimentally and numerically with the intention of using them as pump to generate broad and flattened spectra.

In order to understand the nonlinear processes involved in these nonlinear phenomena, some basic concepts are presented in Chapter 2, as well as a brief overview on NLPs in the frame of SC generation.

In Chapter 3, fairly stable NLPs obtained from a figure-eight laser (F8L) made almost entirely of conventional fiber are presented. By means of another F8L cavity, high-energy pulses were obtained (over 300 nJ) which triggered the generation of broad and flattened spectra directly at the laser output.

Then in Chapter 4, those NLPs obtained from the two different F8L architectures were used as the seed for SC generation. Through the pulses produced with the first laser, spectra covering almost 1000 nm were generated, when NLPs were amplified at the laser output and propagated in a nonlinear medium externally composed of spools of specific lengths of SMF and high-nonlinearity fiber (HNLF). On the other hand, using the high-energy NLPs from the second cavity, flatter spectra were obtained by increasing the harmonic mode locking (HML) order and the length of the SMF spool in the sing section. Finally, fundamental mode locking (ML) pulses were propagated in a spool of HNLF to obtain a SC spectrum of more than 450 nm without an external amplifier.

Lastly, the numerical work is presented in Chapter 5. In a F8L model, more than 1000 NLPs were obtained. In this process, a very complex and rich dynamics was observed by taking some sequences of consecutive pulses which was compared to our previously reported experimental works, both sets of results being consistent. The

other hundreds of pulses were propagated numerically in sections of SMF in order to generate SC averaged spectra, finding similarities with the experimental results of Chapter 4. For these developments, two numerical methods were used: the Split-Step Fourier and the Fourth-Order Runge–Kutta in the Interaction Picture.

Chapter 2. Basic concepts and a brief overview on SC generation via NLPs

The objective of this Chapter is to present a brief overview about noise-like pulses (NLPs) and supercontinuum (SC) generation, displaying first some basic concepts that are necessary to understand some processes involved in them. Sections 2.1 to 2.3 present the concept of optical pulse and its main features. Nonlinear effects in optical fibers are presented in Section 2.4 meanwhile in Section 2.5 are showed the pulses produced in passively mode locked fiber lasers (PML-FL). Sections 2.6 and 2.7 present the mode locking techniques and the kinds of PML-FL. Finally, Section 2.8 shows the state of the art on SC generation using NLPs.

2.1 Optical pulse

A *pulse* of light is a concentrated packet of electromagnetic waves dependent on time and space. In particular, lasers are capable of generating optical pulses (pulsed light) or continuous wave (CW) beams. In the first case, there is a wide range of pulses that varies according to their duration, shape (temporal and spectral), and energy. Neglecting spatial dependence, the electric field of a pulse can be represented as

$$\mathcal{E}(t) = \frac{1}{2}A(t)\exp(i[\omega_0 t - \phi(t)]) + c.c. \tag{2.1}$$

where $A(t)$ is the amplitude, ω_0 is the carrier frequency, y $\phi(t)$ the phase. If we only preserve the complex amplitude, we will have

$$E(t) \approx A(t)\exp\big(-i\phi(t)\big). \tag{2.2}$$

From Eq. (2.2) we have that the intensity and phase are, respectively,

$$I(t) = |E(t)|^2 \qquad \text{and} \qquad \phi(t) = -ArcTan\left(\frac{Im[E(t)]}{Re[E(t)]}\right). \tag{2.3}$$

By way of illustration, a representation of a Gaussian pulse is shown in Fig. 2.1. Here we must clarify that, although in this figure only the amplitude of the envelope can be observed, it is actually a complex function that also contains information about the phase (Cfr. Eq. (2.1)).

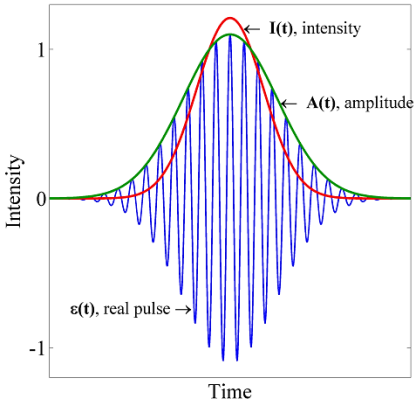

Fig. 2.1. Gaussian pulse profile, its envelope and intensity.

In the case of USPs, the order of magnitude of its duration is from 100s of fs to ps. This means that its envelope covers hundreds or thousands of periods of light (of the order of ~fs in the near IR), which can hardly be represented.

2.2 Chromatic dispersion

It is a linear phenomenon where photons interact with the bound electrons of a medium. Because the optical spectrum of an ultrashort pulse is not monochromatic but contains multiple wavelength components (has nonzero bandwidth), which travel at different velocities in presence of dispersion, the pulse tends to broaden temporally (Fig. 2.2). In a material such as the silica of the optical fibers the amount of dispersion depends on the wavelength.

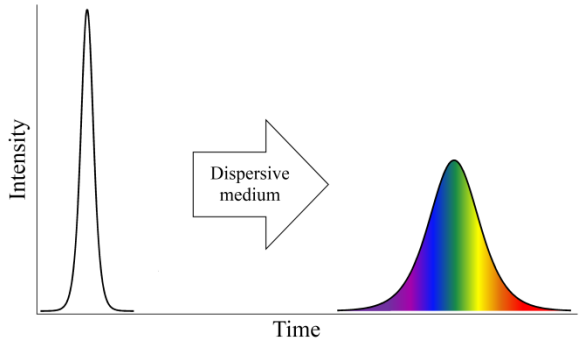

Fig. 2.2. Dispersion of a pulse after passing through a dispersive medium. Before the dispersion, the pulse is narrow; then, the multiple wavelength components are scattered.

In order to describe the dispersion, we shall write the fundamental mode propagation constant β for a pulse around a carrier frequency ω_0 in Taylor series expansion, at which the pulse spectrum is centered:

$$\beta(\omega) = n(\omega)\frac{\omega}{c} = \beta_0 + \beta_1(\omega - \omega_0) + \frac{1}{2}\beta_2(\omega - \omega_0)^2 + \cdots \tag{2.4}$$

with

$$\beta_m = \left(\frac{d^m\beta}{d\omega^m}\right)\Big|_{\omega=\omega_0} \qquad (m = 0, 1, 2, \ldots). \tag{2.5}$$

For $m = 1$ and $m = 2$ in Eq. (2.5), β_m is related to the refractive index: $\beta_1 = 1/v_g = n_g/c$, where v_g is the *group velocity* (dependent on the wavelength) and n_g is the *group index*. And while the group velocity describes the displacement of the envelope of an optical pulse, the parameter β_2 (expressed in $\mathrm{ps}^2/\mathrm{km}$) represents how much the group velocity is dispersed, i.e., how much the pulse broadens temporally. This phenomenon is known as *group-velocity dispersion* (GVD), where β_2 is the GVD parameter [23]; GVD is usually defined as the derivative of v_g with respect to the wavelength, this is $dv_g/d\lambda$. It is important do not to confuse GVD with *group delay dispersion* (GDD): also written as D_2, GDD is the second derivative of

the change in spectral phase ϕ (expressed in ps^2); but also, GDD = $L \cdot$ GVD, with L the length of a medium. While GVD is related to matter, GDD is related to light.

In addition to β_2, it is common to use the dispersion parameter D (expressed in $\mathrm{ps/nm/km}$), which is related to β_2 and n, and has always the opposite sign:

$$D = \frac{d\beta_1}{d\lambda} = -\frac{2\pi c}{\lambda^2}\beta_2 = -\frac{\lambda}{c}\frac{d^2 n}{d\lambda^2}. \tag{2.6}$$

Something important to mention is that both parameters, β_2 and D, vanish at the *zero-dispersion wavelength* λ_{ZD} occurring near 1.27 μm for pure fused silica, as depicted in Fig. 2.3(a). Although for a fiber, λ_{ZD} moves slightly above (1.312 μm) due to the guide dispersion contribution, as depicted in Fig. 2.3(b). For wavelengths shorter than λ_{ZD} ($\lambda < \lambda_{ZD}$), the fiber exhibits what is called *normal dispersion*, where $\beta_2 > 0$ and $D < 0$; this means that components of the pulse with shorter wavelengths (higher frequencies) travel slower than components with longer wavelengths (lower frequencies) of the same pulse. The opposite occurs in the *anomalous dispersion* regime ($\lambda > \lambda_{ZD}$) in which $\beta_2 < 0$ and $D > 0$; this regime allows the balance between nonlinear and dispersive effects which supports the propagation of conservative solitons (see Subsection 2.5.1).

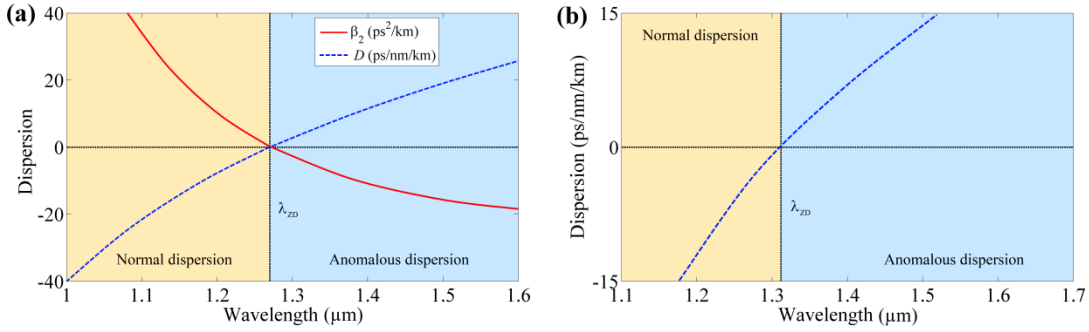

Fig. 2.3. (a) Variation of β_2 and D with the wavelength for pure fused silica ($\lambda_{ZD} \approx 1.27$ μm); (b) variation of D with the wavelength for standard fiber ($\lambda_{ZD} \approx 1.31$ μm).

Chromatic dispersion should not be confused with another type of dispersion called *modal dispersion*. In this phenomenon, the group velocity in a multimode fiber depends not only on the frequency but also on the mode of propagation involved. Besides, there is another type of dispersion that depends on the polarization in the optical fiber, which occurs when the light propagates slightly differently for the modes polarized on the x and y directions: the *polarization mode dispersion*. It occurs due to defects in the fibers, temperature variations or mechanical stress, causing changes in the state of polarization, even though the fibers are designed to have a rotational symmetry and do not present birefringence.

2.3 Instantaneous frequency and Chirp

The *instantaneous frequency* $\omega(t)$ is a time-dependent frequency variable which can be defined as the temporal derivative of the instantaneous oscillation phase ϕ:

$$\omega(t) = \frac{d\phi}{dt}. \tag{2.7}$$

The *chirp* C can be understood as the time variation of the instantaneous frequency along the optical pulse, which corresponds to a temporal separation of frequencies within the envelope of the pulse, expressed as the derivative of Eq. (2.7):

$$C = \frac{d}{dt}\omega(t) = \frac{d^2\phi}{dt^2}. \tag{2.8}$$

As an example, we consider the case of a Gaussian pulse for which the incident field has the general form

$$A(z,T) = |A(z,T)| \exp[i\phi(z,T)], \tag{2.9}$$

or in particular

$$|A(z,T)| = \exp\left(-T^2/2{T_0}^2\right), \qquad \phi(z,T) = \frac{C(z)T^2}{2{T_0}^2}. \tag{2.10}$$

Then, the incident field of a linearly chirped Gaussian pulse is

$$A(z,T) = \exp\left[-(1 - iC)\,T^2/2{T_0}^2\right]. \tag{2.11}$$

In this case, if $C > 0$, the instantaneous frequency increases from the leading to the trailing edge and we have an up-chirped pulse; if $C < 0$, we have a down-chirped pulse; and if $C = 0$ in Eq. (2.11), we get Eq. (2.10): an unchirped, transform-limited pulse (with no phase modulation) [23]. All possible cases with linear chirp are presented in Fig. 2.4, illustrating the different behaviors depending on the dispersion amplitude and sign. It is worth mentioning that a uniform chirp (linear instantaneous frequency), in a pulse that initially has no chirp, is produced by chromatic dispersion; non-uniform chirps are produced by third-order nonlinear phenomena (see Fig. 2.5).

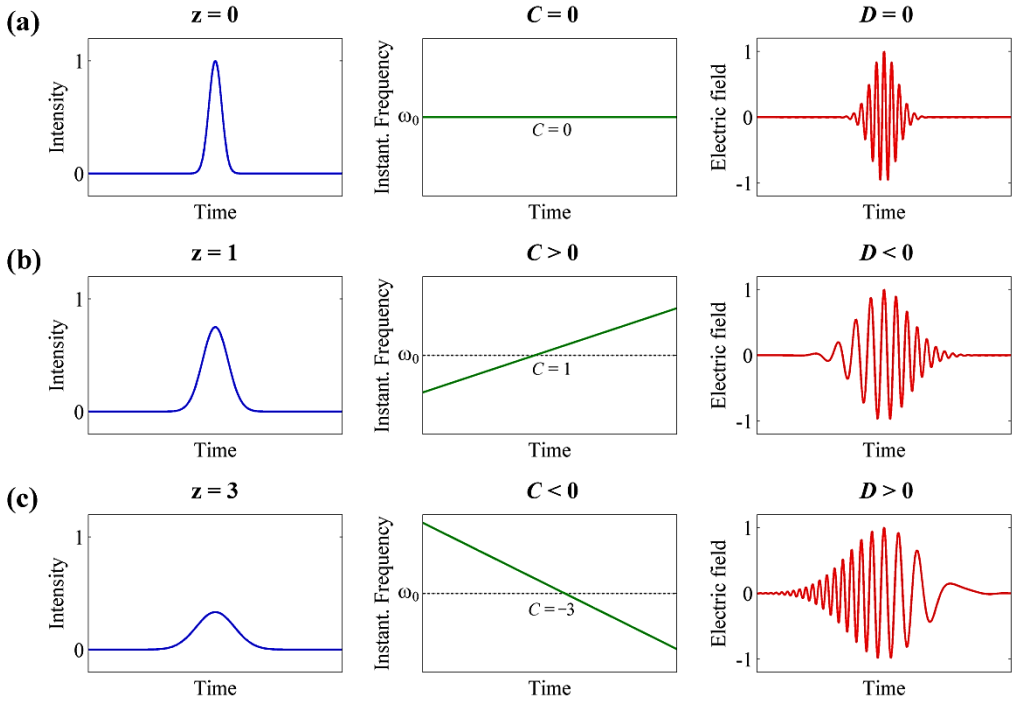

Fig. 2.4. Gaussian pulses: (a) initial ($z = 0$) transform-limited pulse intensity profile, instantaneous frequency (zero slope) and electric field; (b) pulse broadened by normal dispersion (positive chirp); (c) pulse broadened by anomalous dispersion (negative chirp) (a value of $|D|$ larger than in (b) yields larger chirp and pulse duration).

2.4 Nonlinear effects in optical fibers

When an intense electric field interacts with dielectric materials such as fibers, they behave as nonlinear media. The origin of the nonlinear response is related to the anharmonic movement of electrons bound under the influence of an applied field. As a result, the total polarization $\vec{P}$ induced by electric dipoles is not linear in the electric field $\vec{\mathcal{E}}$, but satisfies a more general relationship, written in the form of power series expansion:

$$\vec{P} = \varepsilon_0\left(\chi^{(1)}\vec{\mathcal{E}} + \chi^{(2)}\vec{\mathcal{E}}\,\vec{\mathcal{E}} + \chi^{(3)}\vec{\mathcal{E}}\,\vec{\mathcal{E}}\,\vec{\mathcal{E}} + \cdots\right), \tag{2.12}$$

where ε_0 is the vacuum permittivity and $\chi^{(j)}$ is a tensor of rank $j+1$ and means the jth order susceptibility. The linear susceptibility $\chi^{(1)}$ represents the dominant contribution to $\vec{P}$, and the second-order susceptibility $\chi^{(2)}$ is responsible for such nonlinear effects as second-harmonic generation, optical parametric amplification, sum-frequency generation, among other; however, $\chi^{(2)}$ vanishes in media having inversion symmetry at molecular level like silica (SiO_2). For this reason, the third-order nonlinear effects ($\chi^{(3)}$) are those which take importance in the study of pulses in optical fibers.

2.4.1 Optical Kerr effect

The nonlinear optical Kerr effect is a phenomenon with an instantaneous response in which, due to the interaction with an intense electric field, the refractive index of the medium changes. It can be written as

$$\begin{aligned} n(\omega, I) &= n_0(\omega) + \frac{3}{8}\frac{\chi^{(3)}}{n_0}|E(t)|^2 \\ &= n_0 + n_2 I(t) \end{aligned} \tag{2.13}$$

with I as the intensity of the electric field, n_0 as the linear refractive index and n_2 as the second-order nonlinear refractive index (Kerr coefficient); the nonlinear

index for fused silica is

$$n_2 = 3 \times 10^{-20}\ \mathrm{m}^2/\mathrm{W}. \tag{2.14}$$

It is important to remark that the Kerr effect is a self-induced effect in which the *phase velocity* (velocity at which the phase of any one frequency component of the wave will propagate) depends on the intensity of the same wave. This effect is manifested in optical fibers, even with relatively low intensities, due to the small mode area (especially in standard fiber) and the long lengths used [28].

2.4.2 Self-phase modulation

This nonlinear phenomenon is a consequence of the Kerr effect, where light in a nonlinear material undergoes instantaneously a nonlinear delay in its phase (*phase shift*) as a consequence of its own intensity. This is

$$\Delta\phi_{NL} = n_2 I(t)\frac{2\pi}{\lambda}L = n_2 I k_0 L = \gamma P L, \tag{2.15}$$

where L is the fiber length, γ (expressed in $\mathrm{W}^{-1}\mathrm{km}^{-1}$) is the nonlinear coefficient

$$\gamma = \frac{2\pi n_2}{\lambda A_{eff}}, \tag{2.16}$$

P is the power and A_{eff} the effective modal area

$$A_{eff} = \frac{\left(\iint_{-\infty}^{\infty}|F(x,y)|^2 dxdy\right)^2}{\iint_{-\infty}^{\infty}|F(x,y)|^4 dxdy}. \tag{2.17}$$

Hence, the phase of an optical pulse changes by

$$\Delta\phi = (n_0 + n_2 I)k_0 L = \Delta\phi_L + \Delta\phi_{NL}. \tag{2.18}$$

As the index changes the phase (time dependent) of the wave, a spectral broadening of the pulse occurs [29]. Hence, the initial pulse acquires a temporally varying instantaneous frequency: a non-uniform chirp along the pulse (unlike the case of the chromatic dispersion). In contrast, the temporal profile of pulse intensity (in

particular, duration) does not change (contrary to dispersion, where the temporal profile changes and the spectral one does not). Under the effect of self-phase modulation (SPM) the instantaneous frequency displays an "S" shape, as can be seen in Fig. 2.5 (Cfr. Fig. 2.4); however, near the pulse peak, the instantaneous frequency curve is approximately linear with a positive slope.

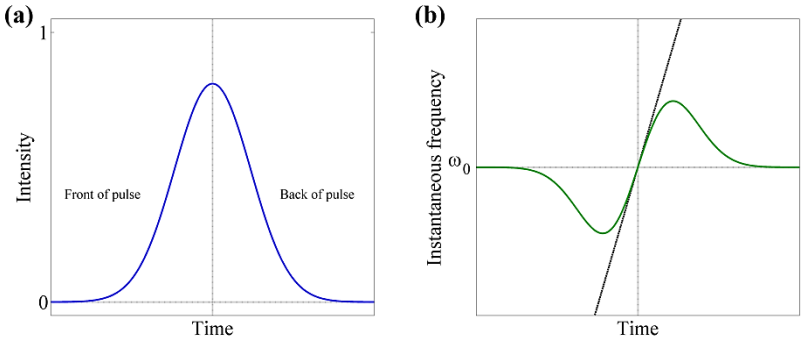

Fig. 2.5. (a) Gaussian pulse which has experienced SPM, and (b) its instantaneous frequency (non-uniform chirp but approximately linear near the peak).

2.4.3 Cross-phase modulation

In this nonlinear optical effect a light beam "A" can affect the phase of a copropagating beam "B" through the Kerr effect. This can be described as a change in the refractive index:

$$\Delta n^{(B)} = 2n_2 I^{(A)}, \tag{2.19}$$

where the intensity $I^{(A)}$ of the beam A causes a refractive index change in the beam B, with n_2 the nonlinear index. Cross-phase modulation (XPM), which is always accompanied by SPM, induces nonlinear coupling among overlapping optical pulses, and induces also asymmetric chirp and spectral broadening [30]. In the frame of the latter, by means of a polarizer in the laser cavity, the wings of the pulse are clipped making shorter the pulse; besides, different nonlinear phase shifts for the

two polarization components of a pulse allow mode locking through nonlinear polarization rotation (NPR, see Subsection 2.7.1.1).

2.4.4 Stimulated Raman scattering

When light is scattered in a medium there are two possibilities: there may exist energy exchange with the material (Raman scattering), or such an exchange may not occur (Rayleigh scattering). The Raman scattering meanwhile, leads to two possible outcomes: absorption of energy by the material when an optical photon hit it (Stokes) or loss of energy (anti-Stokes) [23]. A representation of these interactions is shown in Fig. 2.6. At the beginning, the Raman scattering is a spontaneous process of coupling of light with the molecular vibrations of the medium in which it propagates. Nonetheless, the Stimulated Raman scattering (SRS) takes place when an excess of Stokes photons that were previously generated by spontaneous Raman scattering are present or added to the excitation beam. This third-order phenomenon then creates a Stokes band on the longer wavelength side, shifted by 13.2 THz (≈ 440 cm^{-1}) which means ~113.5 nm at 1550 nm from the center of the pulse spectrum, as depicted in Fig. 2.7 [24,32,33]. If a pulse has a wide bandwidth (10s of nm), the SRS redistributes the energy from the higher frequency components to the lower ones of the pulse. As a result, the spectrum is shifted to longer wavelengths and loses symmetry; this phenomenon is known as *self-frequency shift* (since no other pulse is involved).

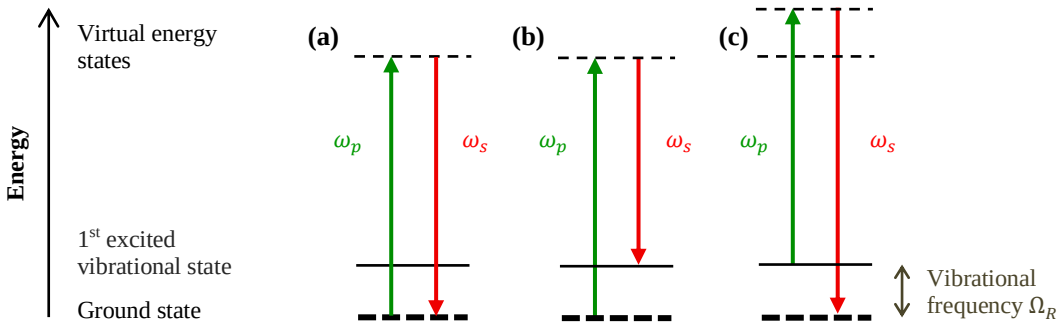

Fig. 2.6. Light scattering: (a) Rayleigh scattering, (b) Stokes Raman scattering and (c) anti-Stokes Raman scattering.

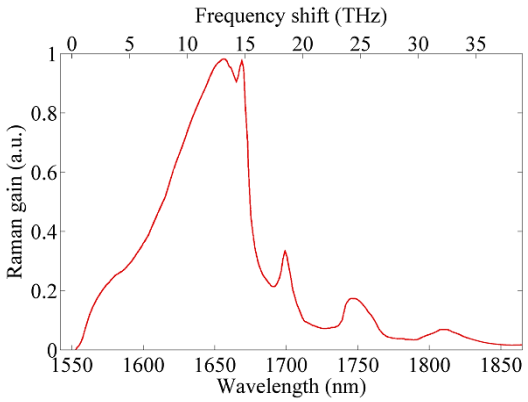

Fig. 2.7. Raman gain response spectrum $g_R(\Omega)$ for fused silica with pump at 1550 nm.

2.4.5 Modulation instability

It is a nonlinear parametric process whereby the small fluctuations of a continuous waveform are reinforced by the presence of nonlinearities, giving rise to the generation of spectral sidebands (Fig. 2.8; see also Fig. 2.10) and the eventual rupture of the waveform into USPs; this means, modulation instability (MI) manifests itself as breakup of the CW or quasi-CW radiation into a train of USPs [19,23]. MI, which in particular can be initiated by two CW beams with slightly different wavelengths, is very useful for producing USP trains allowing tuning of the pulse repetition rate [31].

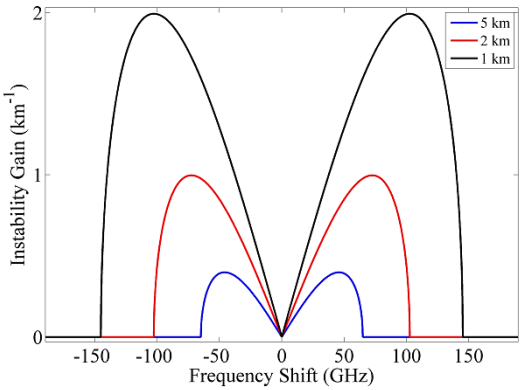

Fig. 2.8. MI gain spectra for three values of L_{NL} when a CW beam is launched into a fiber with β_2 = –5 ps^2/km.

And although MI is initiated by SPM, the most important condition for its happening is to have anomalous-GVD regime, at least in standard single-mode fiber (SMF). The gain spectrum of modulation instability is written as

$$g(\Omega) = |\beta_2 \Omega| \sqrt{\Omega_c^2 - \Omega^2}, \tag{2.20}$$

where Ω is the frequency of perturbation and $\Omega_c = 2/\sqrt{|\beta_2| L_{NL}}$, with L_{NL} the length over which dispersive or nonlinear effects become important for pulse evolution [23].

2.4.6 Four-wave mixing

It is a phase-sensitive third-order parametric phenomenon, which implies that it is strongly affected by phase matching conditions. In combination with SPM, XPM, and SRS, four-wave mixing (FWM) can generate very strong spectral broadening in fibers, toward longer but also toward shorter wavelengths: sidebands spaced at equal frequency intervals from the pump frequency [34]. It should be mentioned that under phase matching conditions, FWM can suppress SRS because the threshold of the former is lower than that of the latter [23].

FWM can occur if at least two photons of different wavelengths interact together in a nonlinear medium. The interactions between these three wavelengths produce one new wavelength. By energy conservation, the relation among the frequencies of these four photons is given by

$$\omega_{ijk} = \omega_i + \omega_j - \omega_k \qquad (i, j \neq k), \tag{2.21}$$

where ω_i and ω_j are the pumping light frequencies, and ω_k is the signal light frequency (probe light), interacting to generate a fourth frequency ω_{ijk}.

If we assume that Eq. (2.21) presents all different frequencies, the phenomenon is called *non-degenerate* FWM, illustrated in Fig. 2.9(a). This is

$$\omega_4 = \omega_1 + \omega_2 - \omega_3. \tag{2.22}$$

On the other hand, if we assume in Eq. (2.21) that the two pumping photons have identical frequencies ($\omega_1 = \omega_2$), we shall have the *degenerate four-wave mixing* (DFWM), illustrated in Fig. 2.9(b), where these two photons are annihilated while other two (ω_3 and ω_4) are created simultaneously shifted toward the blue and red sides. So, Eq. (2.21) becomes

$$\omega_4 = 2\omega_1 - \omega_3. \tag{2.23}$$

It is worth mentioning that in addition to the frequencies of the photons involved, it is also necessary to consider the conservation of momentum $\vec{k}$; the phase-matching conditions are depicted in Fig. 2.9 (bottom).

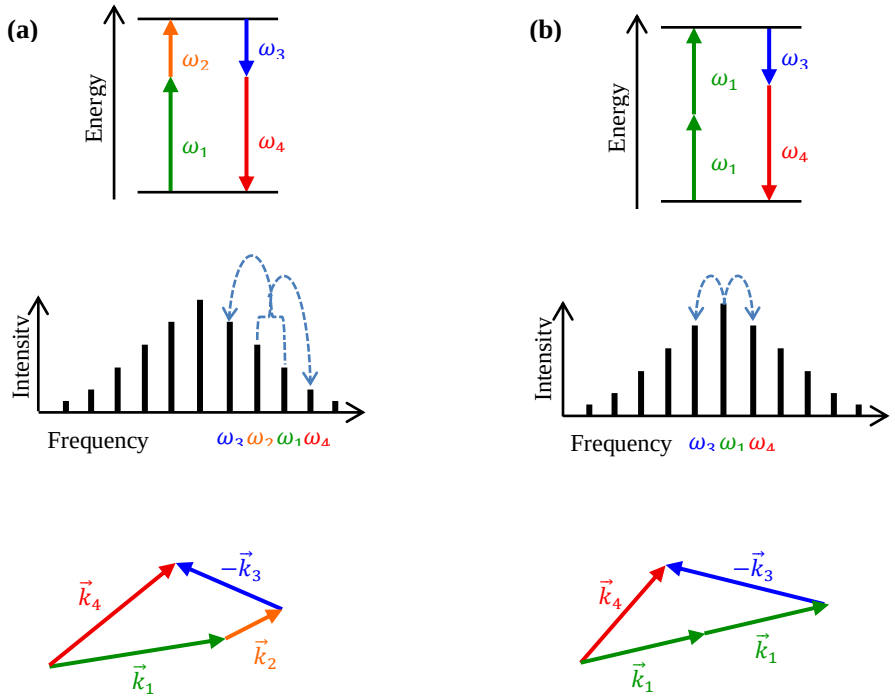

Fig. 2.9. Energy level diagrams (top), schematics in the frequency domain (middle), wave-vector matching diagrams (bottom): for (a) non-degenerate FWM and (b) DFWM.

Figure 2.10(a) shows a phase matching diagram for a specific HNLF (Fig. 1 in [34]), where FWM is observed in the normal dispersion regime whereas MI (see Subsection 2.4.5) is observed in the anomalous regime. The representation of a comparison of FWM and MI parametric generation is shown in Fig. 2.10(b) (Fig. 2 in [34]).

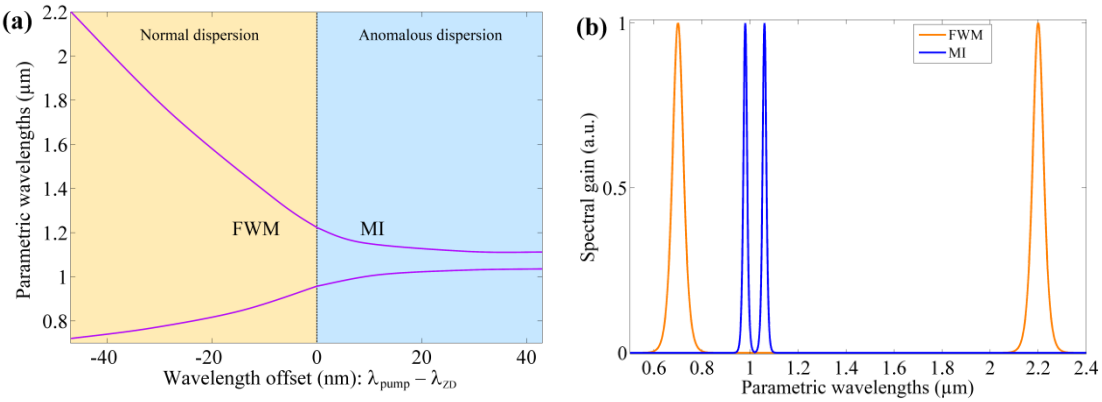

Fig. 2.10. (a) Example of a nonlinear phase matching diagram showing FWM (left) and MI (right) processes; (b) spectral gain generated at the indicated parametric wavelengths of (a), for FWM and MI.

2.5 Optical pulses in passively mode locked fiber lasers

The stationarity of the pulse in a laser cavity is due to a balance between several optical effects: saturable absorber, gain, loss, gain bandwidth limit, Kerr effect, and chromatic dispersion, among others.

One of the advantages offered by fiber lasers (FL) and in particular by passively mode locked fiber lasers (PML-FL) is the great variety of pulses (long, short and ultrashort) that can be produced. Among the pulses generated by this kind of lasers (see Section 2.7 for types of PML-FL) are conservative solitons, dispersion-managed solitons, similaritons, dissipative solitons, dissipative soliton resonance (DSR) solitons, and noise-like pulses (NLPs).

2.5.1 Soliton

The term soliton was coined in 1965 [35], to reflect the particle-like nature of those solitary waves that are robust against perturbations and remain intact even after mutual collisions, being a static solution of the nonlinear wave equation (in nonlinear integrable systems); this solution is remarkable because it retains in shape and velocity after colliding with another equal one and remains intact when interacting with radiation waves.

Solitons have been discovered and studied in many branches of physics including optics; here, a soliton is a special kind of wave packet which can propagate undistorted over long distances, where the GVD parameter β_2 is constant along the fiber [23]. This is possible because the dispersive effects are balanced by the nonlinear Kerr effect. These solitons are called *conservative solitons* because their existence is not based on the exchange of energy between them and their propagation medium (negligible levels), but on the balance between dispersion and the Kerr effect (two conservative effects). Such a balance is carried out in anomalous dispersion ($\beta_2 < 0$ or $D > 0$), where the equation for the evolution of the envelope admits solutions [36].

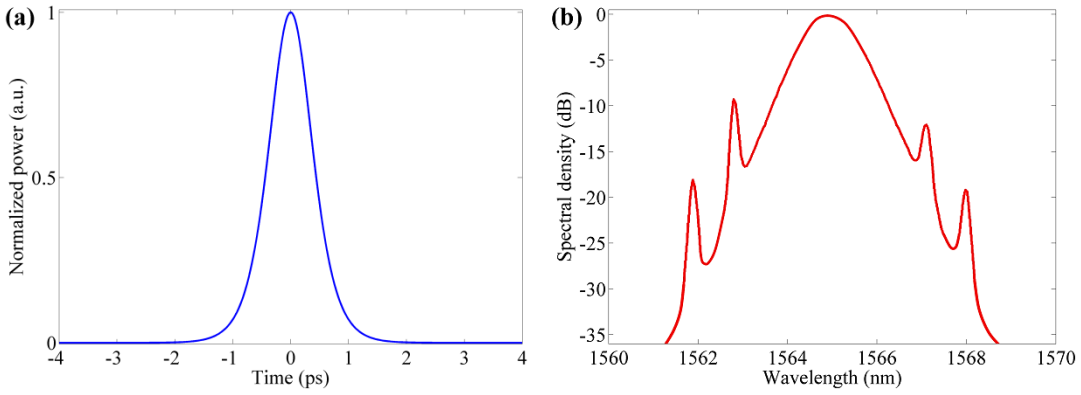

Fig. 2.11. (a) Temporal profile of the fundamental soliton ($N = 1$) and (b) a typical spectrum showing the Kelly sidebands.

The temporal profile of the fundamental soliton ($N = 1$) shows an unchirped sech^2-shape (assuming that the GDD is constant), whereas its duration is of the order of 1 ps (Fig. 2.11(a)) and its energy per pulse of the order of 100s of pJ in fibers; otherwise ($N > 1$), a higher-order soliton (HOS) which carry higher energy, suffer a periodic evolution on its temporal profile. In general, as typical signature of these USPs, the spectrum presents some lateral peaks known as *Kelly sidebands* (Fig. 2.11(b)). Nonetheless, in presence of only anomalous dispersion and SPM the spectrum is smooth and these bands do not appear; they appear when solitons are disturbed, as it happens in a laser cavity where there are more effects present (filters, attenuation, amplification, etc.). This perturbation implies an adjustment of the soliton parameters that loses a fraction of its energy in the process, which constitutes the *dispersive waves*: disturbances whose energy is redistributed (dispersed) as they propagate, because the different components of the perturbation travel at different speeds. At certain particular wavelengths, the dispersive waves resonate with the soliton, amplifying them, forming the aforementioned Kelly sidebands.

2.5.1.1 Dispersion-managed soliton

This pulse has different properties from those of an ordinary soliton: its amplitude and width oscillate in a periodic way but also its instantaneous frequency, by which it presents chirp. The "dispersion management" technique consists of using a periodic dispersion map by combining fibers (in practice just two kinds of fibers with opposite signs of β_2 are needed [37], as shown in Fig. 2.12) with different characteristics, so that the average GVD in the cavity is quite low whereas the local GVD at every point along the cavity is relatively large [23]. On average, these variations compensate each other by alternating dispersion. Hence, this pulse is temporally compressed and stretched periodically during its course in the cavity (alternating positive and negative chirp values), which gives a "breathing" effect to the pulse, so they are so-called *breathing solitones*. By locating the output port in the right position we can get transform-limited pulses directly at the laser output. This type of pulses due to its formation process can reach energies of the order of nJ.

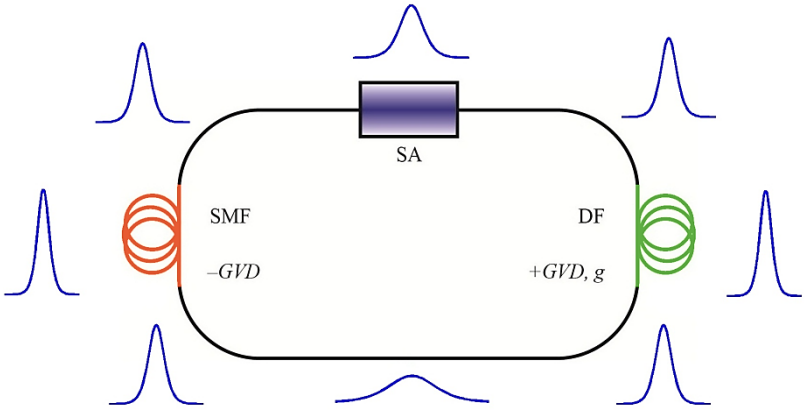

Fig. 2.12. Evolution of a soliton in a ring cavity using the dispersion management technique.

2.5.2 Similariton

A similariton (also called *self-similar pulse*) is an USP that has a temporal intensity profile with a parabolic shape, not only near the pulse center, but also well towards the wings up to the point where the intensity vanishes [41], as depicted in Fig. 2.13. Unlike conservative solitons that are static solutions of the nonlinear wave equation and maintain their shape, width and amplitude, similaritons are asymptotic solutions of the nonlinear wave equation and maintain their shape but not their width or amplitude.

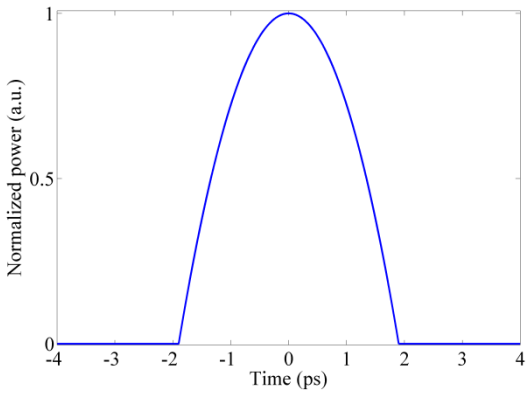

Fig. 2.13. Parabolic temporal profile of a similariton.

One of the characteristics that makes similaritons interesting is in fact their parabolic shape which makes them resistant to wave breaking inside the cavity (the limited energy of USPs is generally due to wave breaking, a consequence of excessive nonlinearity) [42]. The presence of normal dispersion tends to linearize the chirp accumulated by the pulse, which increases the spectral bandwidth but does not destabilize the pulse; and because of this linearity, the pulses allow to be compressed at the laser output. In similariton lasers, the growth of the duration can be counteracted by compensating the dispersion, by the saturable absorber or by filtering effects by the gain bandwidth [43]. This type of pulses reaches peak energies up to few 10s of nJ.

2.5.3 Dissipative soliton

This type of pulses (Fig. 2.14), unlike conservative solitons, requires a balance between parametric gain and fiber losses; this means that there are dispersion, nonlinear effects and also energy exchange with the medium [38]. Specifically, the energy, profile and chirp of a dissipative soliton are predetermined by the equation parameters, rather than by the initial conditions. They can arise not only in anomalous dispersion but also in normal dispersion, in combination with a positive nonlinear

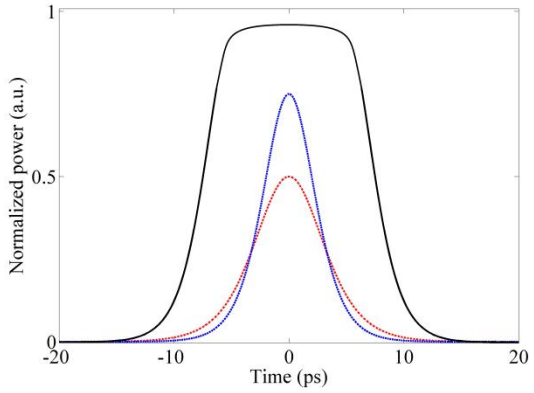

Fig. 2.14. A few examples of temporal profiles of dissipative solitons.

index if there is also a spectral band pass filter effect and a strong optical gain (to compensate the energy losses through the filter). Dissipative solitons (among which are the Brillouin solitons), allow to operate diverse regimes in mode locked cavities through tunings in the system, generating stable high repetition pulses typically for telecom applications, or high-energy pulses for industry and medicine applications.

It should be mentioned that high-energy dissipative solitons have been obtained, up to 10s of nJ [39]. Although the pulses have a significant chirp, they can be compressed at the laser output (e.g. using a pair of prisms or grating compressors) because the chirp is linear, something that does not occur with the dissipative soliton resonance pulses (described below). Once compressed several dozen times outside the laser, they produce transform-limited pulses with durations below the ps, and with peak powers of the order of 100s of kW and even MW after dechirping [40].

2.5.3.1 Dissipative soliton resonance soliton

Under the dissipative soliton resonance (DSR) generation, this square pulse can exist in normal or anomalous dispersion, increasing its nonlinear gain broadening in the time domain while its peak power remains constant. In other words, the pulse amplitude is held while the energy is accumulated by the expansion of its temporal width, so that it has a rectangular profile up to hundreds of ns, increasing greatly its energy without breaking, as shown in Fig. 2.15. For example, it has been reported DSR pulse energies up to 6.5 µJ with a F8L [44] and energies greater than 3 µJ with a scheme called figure-9 laser [45] (which is really nothing less than a linear scheme Fabry-Perot type, with a NALM used in reflection on one end and a simple Sagnac mirror in the other); however, in these specific cases fits the possibility that the authors are overestimating the energy per pulse, taking into account some "noise" which is not part of the pulse. However, in the frame of the complex cubic-quantic Ginzburg-Landau equation (which governs this type of pulses), it was theoretically shown that with certain laser parameter selections, the energy of this kind of pulses could increase indefinitely. Nonetheless, as a great disadvantage, the

DSR solitons present a nonlinear chirp, which makes them difficult to compress at the laser output. It is worth mentioning that the shape of these pulses can be confused with the envelope of noise-like pulses (described below), so the measurement of the spectrum and the autocorrelation trace is essential to differentiate them; for DSR pulses, the corresponding autocorrelation trace has a triangular profile [46].

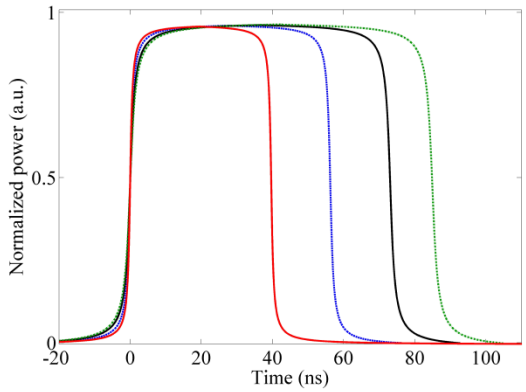

Fig. 2.15. Evolution of a DSR soliton by increasing its energy; the temporal width extends to the right, remaining the peak power.

2.5.4 Noise-like pulse

A noise-like pulse (NLP) is a ~ns-long wave packet containing thousands of pico- or femtosecond sub-pulses [1], displaying a very rich and complex internal dynamics at short time scales (Fig. 2.16(a)) but exhibiting a fairly stable overall behavior at large time scales (Fig. 2.16(b)).

Because of the complex internal dynamics of NLPs, we can get a precise idea of their internal structure only by means of numerical simulations (see Chapter 5), because an experimental measurement able to see its internal details is not possible with the current optoelectronics; even with ultrafast oscilloscopes we can only measure the envelope. With respect to this last point, an appropriate characterization of NLPs is essential because in practice, its profile can be confused with that of other pulses.

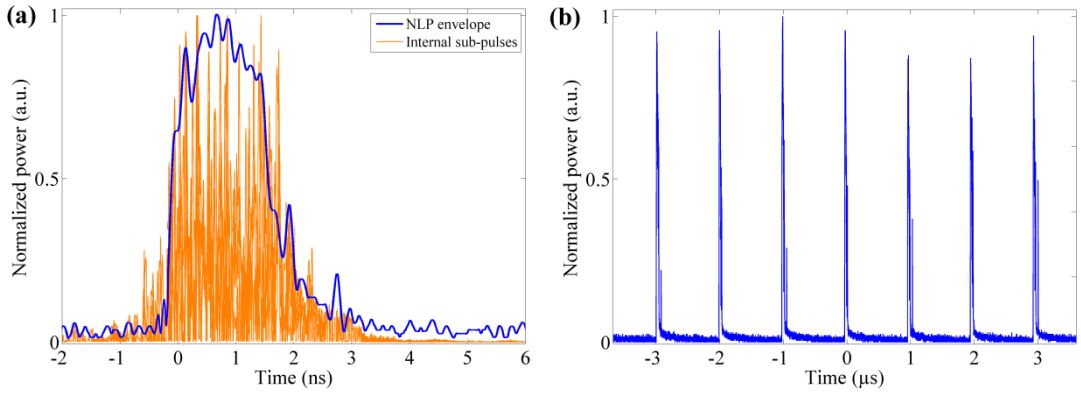

Fig. 2.16. (a) Experimentally measured envelope of a NLP and numerically simulated internal sub-pulses; (b) fairly stable pulse train.

Hence, in addition to show a quite stable envelope (Fig. 2.16), NLPs present as typical signature [5] a broad and smooth average spectrum of the order of 10 nm of extension at 3 dB or much more (Fig. 2.17(a)), and a double-scaled autocorrelation trace with an ultrashort coherence spike riding upon a wide pedestal (Fig. 2.17(b)). The spike in the autocorrelation trace reflects the averaged internal temporal granularity of the main packet, whereas the pedestal extension represents the entire temporal extension of the pulse burst.

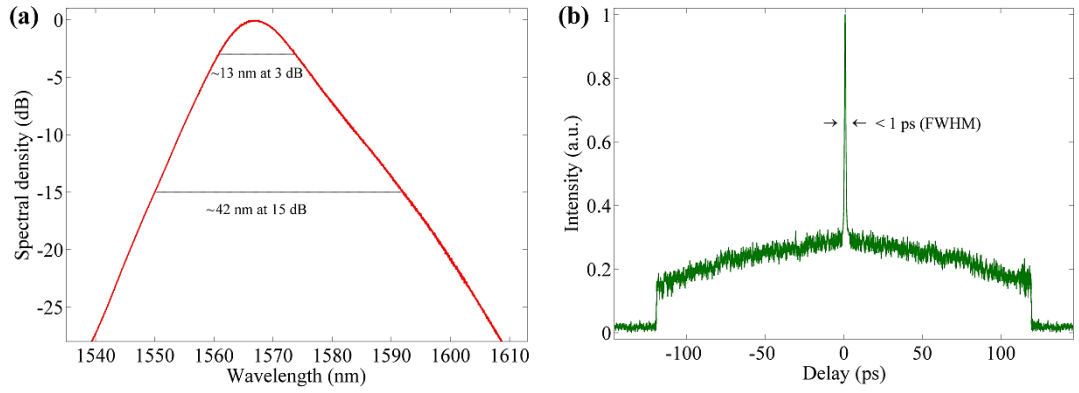

Fig. 2.17. (a) Typical spectrum of NLPs and (b) its double-scaled autocorrelation trace.

Due to the duration of the NLPs (~ns) and the absence or quasi-absence of temporal coherence through the packet, it has not been possible to characterize well its instantaneous frequency.

Since they were first reported in 1997 by Horowitz et al. [1], NLPs started to receive significant research attention because of their extraordinary and distinctive features contrasted with the ordinarily ML pulses. Besides, these complex pulses permit to study fairly stable and also non-stationary pulsed regimes by only modifying the polarization on the laser cavities (Cfr. [4,17] and [6,7]). In addition, NLPs allow energies per pulse up to 100s of nJ [2–4] which is a thousand times greater than that of a soliton, because a NLP is not a simple pulse but a large bunch of radiation (Fig. 2.16(a)).

NLPs are obtained in a wide variety of PML cavities (rings [5,14,16,47–49] and figure-eight lasers [4,15,17]) being generated in both normal and anomalous dispersion regimes [8,50], and using different kinds of fibers including standard and doped fibers, double-clad, and high-nonlinearity fibers (HNLF). In order to obtain this type of pulses, the ML cavity must be large enough (10s of m or much more), because the creation and interaction of nonlinear optical phenomena (SPM, XPM and SRS) becomes dominant as the length of the fiber increases; and although in short cavities with low dispersion, NLPs of few ps of duration have been obtained, in large cavities the pulses can be very energetic and their temporal duration becomes dependent on the power [51].

To date, the formation of NLPs is still a broad subject of study, but it is known that such formation may be a consequence of the combined effect of the collapse of solitons [47], but it may also be due to the use of very high pump powers, which could result in the increase of dispersive waves and noise background, thereby initiating their formation [52]. Besides, it has also been reported that their rising does not always occur smoothly but displaying a nearly step-like evolution, as well as their vanishing, having a sudden energy transfer with the background radiation [53].

On the other hand, the complex dynamics of NLPs has also been studied, among which is the releasing of sub-packets from the main bunch [6,7] and the pulse breaking process [54,55] (in some cases, this process allows obtaining the harmonic mode locking (HML) regime; see Section 4.2). Even the coexistence of NLPs with solitons in a hybrid regime was reported [56,57]. In addition, NLPs are also connected to the generation of the extreme events called optical rogue waves (RW) [8,9,58,59], with what it is sought at the same time to understand the oceanographic RW from where the concept was derived from before its extension to optics.

As well as the distinctive features of NLPs presented above, several applications have been developed based on the fundamental mode locking operation, such as low-coherence spectral interferometry [10], micromachining [11], nonlinear frequency conversion [60], optical coherence tomography (OCT) [13], and supercontinuum generation; the latter will be described in Section 2.8.

2.6 Mode locking

Mode locking (ML) is the most important technique for obtaining short and ultrashort pulses from lasers. When a laser is mode locked, one pulse (the fundamental ML) is circulating in the cavity. In this case, the phases of the axial modes are equalized, or locked together, and the superposition of their amplitudes generates a pulse train of period T, as depicted in Fig. 2.18(a), determined by the round-trip time. Nonetheless, multiple identical pulses with a constant spacing called *harmonic mode locking* (HML) can be circulating in the cavity (see Fig. 3.6 and Section 4.2). If the ML regimen is not achieved above the lasing threshold, this means modes having random phases, a free-running laser regime can be observed as in Fig. 2.18(b).

Depending on the mechanism of pulse formation into the laser resonator, the mode locking can be classified into two categories: active and passive mode locking.

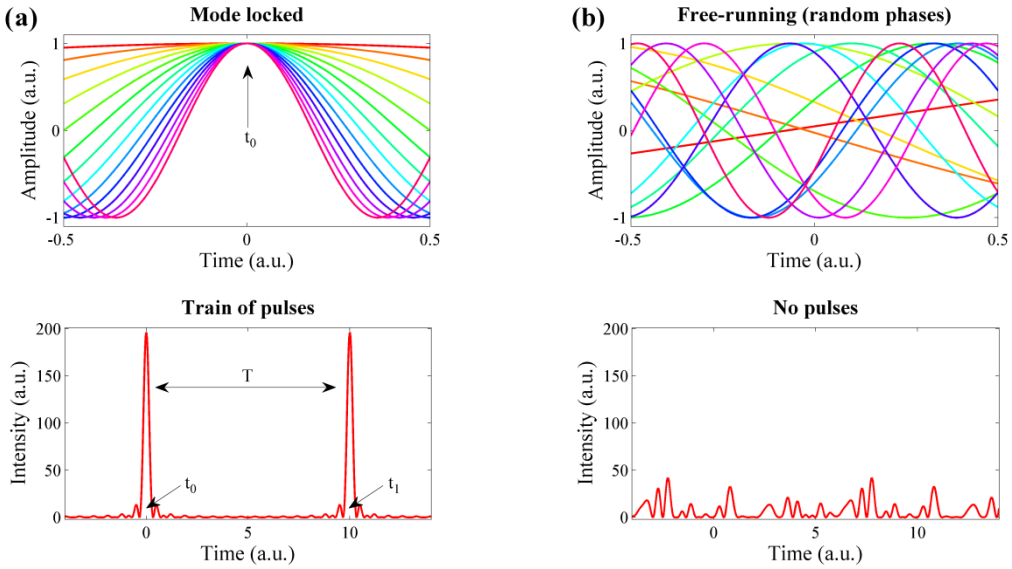

Fig. 2.18. Representation of (a) mode locking regime with a period T and (b) free-running regime.

2.6.1 Active mode locking

The formation of pulses involves the round-trip periodic modulation of the phase or of the resonator losses, when a modulator is introduced into the cavity; it may be an acousto-optical, electro-optical or a semiconductor modulator. A representation of this category of ML in a linear cavity is presented in Fig. 2.19.

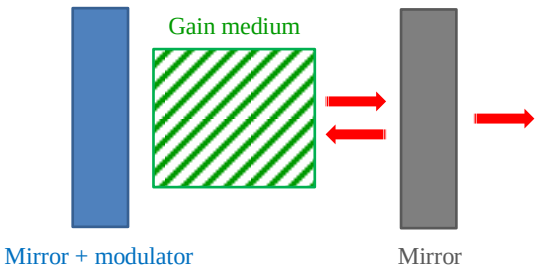

Fig. 2.19. Schematic of an actively mode locked laser. In this representation, the modulator is attached to a mirror in order to modulate once per cycle.

When the modulation frequency is synchronized with the cavity length resonance frequency, USPs are obtained. Hence, this technique can be used when the pulse train is required to be synchronized with some external signal.

2.6.2 Passive mode locking and Saturable absorber

The formation of pulses in this case is due to the introduction of a *saturable absorber* (SA) into the cavity, either physical or artificial. A SA is a nonlinear optical device that causes significant losses in the laser cavity, generating narrow and intense pulses: at low power, the SA absorbs and generates important losses; for high power, the SA is saturated and significant losses are no longer produced. As this operation is established without the need for an external signal it receives the *passive* name.

In particular, the *artificial SA* works through the Kerr effect, and since this effect is very fast, the SA action is too, allowing passive mode locking to be a very effective technique for obtaining (fs–ns) pulses. A SA has the capacity to compress pulses by attenuating low intensity signals and allowing the pass of intense signals in each round and back in the cavity. This type of mode locking allows the manufacture of very robust pulsed lasers as the case of the mode locked figure-eight laser (F8L) through a NOLM, where the latter works as an artificial SA that is adjusted for low low-power transmission. In this technique, several nonlinear optical phenomena are involved, such as SPM, XPM and NPR (for the latter, see Subsection 2.7.1.1). A representation of a PML laser in a linear cavity is shown in Fig. 2.20.

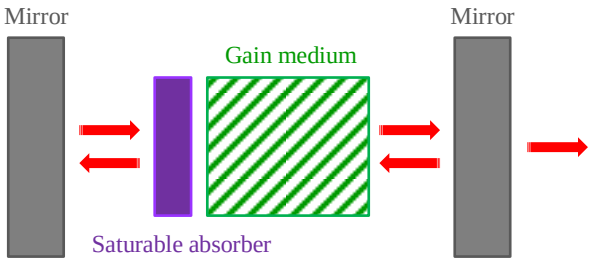

Fig. 2.20. Schematic of a passively mode locked laser.

2.7 Passively mode locked fiber lasers

In general terms and depending mainly by their active medium and their resonator, lasers can be encompassed in five categories: solid-state, gas, dye laser, semi-conductor and fiber laser. These types can in turn be classified into two modes of operation, according to the light produced: continuous wave (CW) and pulsed light. To generate pulses in fiber lasers we can use two techniques: Q-switching and Mode locking (the latter described in the previous Section). In this thesis one kind of pulsed light (NLPs) was generated in two cavities of F8L; this is one of the two passively mode locked fiber lasers (PML-FL) architectures. To better understand its setup and operation, both architectures are presented below: the ring laser and the F8L.

2.7.1 Fiber ring laser operation

Before presenting the ring configuration, the nonlinear phenomenon that allows its operation will be explained.

2.7.1.1 Nonlinear polarization rotation

When a pulse propagates in an optical fiber that does not maintain polarization (such as the SMF), a nonlinear effect through the intensity-dependent polarization variation is manifested: the nonlinear polarization rotation (NPR). Because all fibers support two orthogonally polarized modes (except for those polarization-maintaining fibers, PMFs), they exhibit in practice some modal birefringence. The cause of NPR is related not to the birefringence implicit in the fiber, but to the SPM and XPM. If high intensity light propagates in the fiber, its nonlinearity will also play a role on the evolution of polarization (so the NPR is also called *nonlinear polarization evolution*, NPE). When light passes through a polarizer, a dependence of its transmission on the intensity occurs because it selects one of the two modes of polarization traveling along the cavity. Then, using a wave plate or a polarization controller (PC), the adjustments can be performed to get low transmission through the polarizing element at low power, and maximal transmission for some higher value of power. The NPR is

then a result of a phase shift between circular components that depends on the power and polarization state of the light (ellipticity). When NPR is present in a laser cavity, it functions as an artificial SA, with the power transmission through the polarizer given by [61]

$$|T_{NPR}|^2 = \sin^2\theta_1 \sin^2\theta_2 + \cos^2\theta_1 \cos^2\theta_2 + \frac{1}{2}\sin(2\theta_1)\sin(2\theta_2)\cos(\Delta\phi_L + \Delta\phi_{NL}), \quad (2.24)$$

where $\Delta\phi_L$ and $\Delta\phi_{NL}$ are the linear and nonlinear phase delays between the two orthogonal modes induced by the fiber birefringence; θ_1 and θ_2 are the azimuth angles of the polarizer at the beginning of the fiber, and the analyzer, at the end of the fiber (Fig. 2.21).

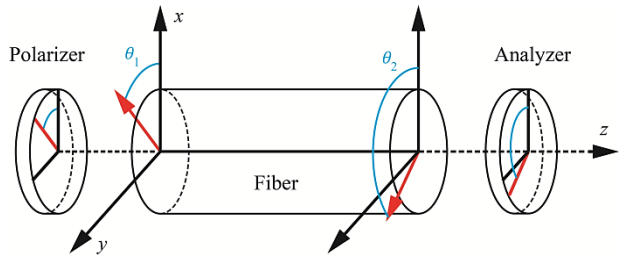

Fig. 2.21. Schematic of NPR based on a birefringent optical fiber between a pair of polarization-selective elements.

2.7.1.2 Fiber ring laser

A ring laser cavity is a fiber circular resonator operating on the basis of the NPR effect, where a power-dependent polarization change becomes a power-dependent transmission through an optical element of polarization. Figure 2.22 shows an example of a ring laser with a doped fiber (DF) as amplifier**.** In this figure, a polarizer (POL) is placed after the isolator (ISO), and a polarization controller (PC) changes the linear polarization state to elliptical; it evolves nonlinearly during propagation of the pulse due to the SPM- and XPM-induced phase shifts imposed on the orthogonally polarized components. Then, the PC placed before the polarizer forces

the polarization to be linear again, with an angle that is close to the polarizer angle for high-power components. The polarizer lets the central intense part of the pulse pass but filters out the low-intensity pulse wings. Hence, the SMF spool (where NPR takes place) and the polarizer make the pulse slightly shortened after each round trip inside the ring cavity. Examples of PML ring lasers can be found in [5,14,48,54,57].

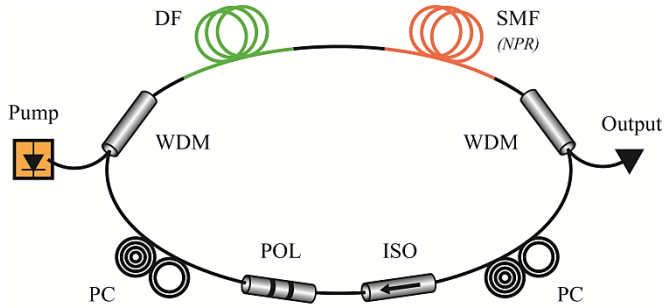

Fig. 2.22. Schematic PML ring laser based on NPR.

2.7.2 Figure-eight laser

Unlike the ring laser, a figure-eight laser (F8L) consists of two fiber loops where the former is a ring cavity indeed and the latter is a nonlinear optical loop mirror (NOLM); its 8-shape justifies its name. In this kind of fiber lasers, light is divided by a coupler and the counterpropagating beams travel in the NOLM; the interference condition for recombining the two beams at the coupler in the middle becomes power-dependent. The formation of pulses in F8Ls is generally not based on NPR in the ring section but on the action of the artificial SA in the NOLM. Examples of F8Ls can be found in [2,4,15,17]; the schemes in the last two references are depicted in Fig. 3.1 and Fig. 3.3.

2.7.2.1 Nonlinear optical loop mirror (NOLM)

Also known as *nonlinear Sagnac interferometer*, the NOLM is an ultrafast switch that is used as a modulator and optical commutator; in a F8L is used as an artificial SA, for pulse compression, pedestal suppression, laser tuning, among other. This

device, which operates through the nonlinear Kerr effect, is formed from the junction of the output ports of a 2×2 coupler by a piece of fiber to form a loop. Since its appearance in 1976 [62], this nonlinear interferometer has been used in many applications and it was initially built from bulk elements. Five years later, the first all-fiber Sagnac interferometer was presented [63] offering high stability and sensitivity. However, it was until 1988 when the Sagnac interferometer was treated as an optical mirror (NOLM) [64], using a four-port coupler focused on ultrafast switching. In 2000 [65], a polarization-independent NOLM was designed using a non-symmetric coupling and highly twisted fiber, through a 50/50 coupler, which gave rise to new possibilities for the construction of mode locking devices, intensity filters and demultiplexers. To date, several NOLM schemes have been reported; the most notable being those presented below.

2.7.2.1.1 *Power-asymmetric NOLM*

By using a power-asymmetric coupler $r/(1-r)$, this scheme allows a switching through the power imbalance between counterpropagating beams in the fiber loop, as can be seen in Fig. 2.23, causing different phases depending on the input power that will allow switching, through the SPM effect. By adjusting an inserted polarization controller (PC), the transition from the saturable absorber mode (positive slope) to the intensity limiter mode can be done. Nonetheless, this scheme has the disadvantage of being based on the coupling ratio r, which implies that the coupler must be replaced if the user requires different transmission characteristics, limiting the dynamic range. Another limitation is that the minimum transmission cannot be zero.

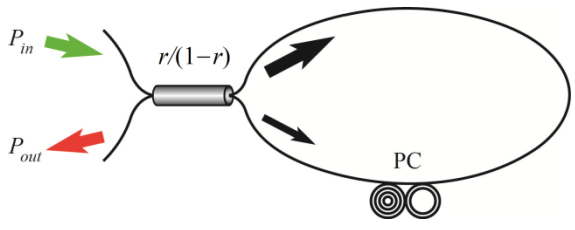

Fig. 2.23. Power-asymmetric NOLM scheme.

In fact [64], the output power is given as

$$P_{out} = P_{in} - 2r(1-r)P_{in}[1+\cos(D\phi_{NL})], \tag{2.25}$$

where P_{in} is the input power (green arrow in Fig. 2.23) and $D\phi_{NL} = \Delta\phi_{NL}^{cw} - \Delta\phi_{NL}^{ccw}$ is the nonlinear phase shift difference under the influence of SPM; $\Delta\phi_{NL}$ is described in Eq. (2.15). If

$$D\phi_{NL} = m\pi \tag{2.26}$$

for m odd, Eq. (2.25) shows that for any value of $r \neq 0.5$ (50%), the whole input power emerges from the red arrow port (100% transmission); Fig. 2.24 shows the power output for three values of r. The minimum transmission occurs for m even and Eq. (2.25) is given by

$$P_{out} = P_{in}[1-4r(1-r)]. \tag{2.27}$$

Note that if $r = 0.5$ (50/50 coupler), Eq. (2.27) becomes zero; however no switching takes place in this case (transmission $= 0$ for any value of input power).

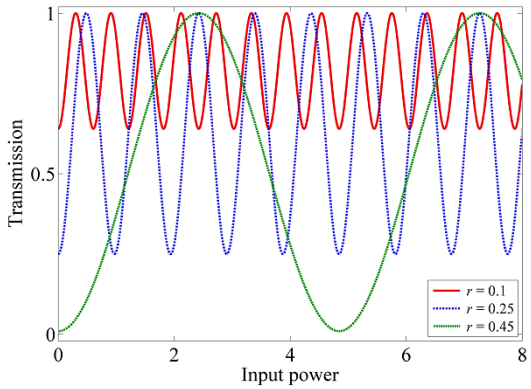

Fig. 2.24. Transfer function against input power for three different coupling ratios.

In this NOLM setup, the *switching power* P_π (also called the *critical power*), defined as the power at which the nonlinear differential phase shift reaches π, is given by

$$P_\pi = \frac{\lambda A_{eff}}{2(1-2r)n_2 L} = \frac{\pi}{(1-2r)\gamma L} \tag{2.28}$$

where the nonlinear coefficient γ (Eq. (2.16)) is written in terms of A_{eff}, the effective modal area (Eq. (2.17)). The output switches from the low-power value to 100% when the power increases from zero to the switching power P_π.

2.7.2.1.2 *NALM: Power-asymmetric NOLM scheme with an amplifier inserted asymmetrically inside the loop*

If a power-symmetric coupler (50/50) is used, and an asymmetrically located optical device is inserted in the loop (amplifier or attenuator), control over the power switching and the transmission will be taken. This is because the power difference between the counterpropagating beams can be controlled though the adjustable loss/amplification. In particular, if an externally pumped doped fiber (DF) as amplifying element is inserted in the NOLM, as depicted in Fig. 2.25, a *nonlinear amplifier loop mirror* (NALM) then will be obtained [66]. Considering the power-symmetric coupler, the power output [67] is given by

$$P_{out} = \frac{1}{2} g P_{in} \left[1 - \cos\left(\frac{1}{2}\gamma P_{in} L(g-1) - \Delta\phi\right)\right], \tag{2.29}$$

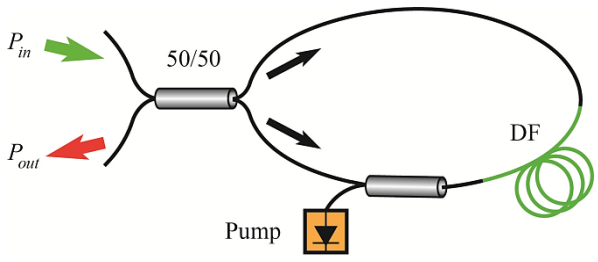

Fig. 2.25. Nonlinear amplifier loop mirror (NALM).

where g is the amplifier gain/attenuator loss, γ is the nonlinear coefficient, L the length of fiber and $\Delta\phi$ is the phase bias. In a NALM [68], the switching power is given by

$$P_{\pi} = \frac{\lambda A_{eff}}{n_2 L(g-1)} = \frac{2\pi}{\gamma L(g-1)}. \tag{2.30}$$

According to the scheme (Fig. 2.25), the input power P_{in} splits equally at the coupler and experiences a differential phase delay along the two propagation directions owing to the asymmetrically located amplifier/attenuator. However, in the case of an attenuator, since the loop presents loss, although complete switching is possible (minimal transmission $= 0$), the entire device displays attenuation (maximal transmission < 1), which represents a great disadvantage; besides, losses due to the introduction of optical devices in the loop, although low, must also be considered. In the case of an amplifier, the maximal transmission is greater than 1 and switching power can be very low; however, the device is no longer passive as it requires external pump power to operate.

2.7.2.1.3 *Power-symmetric, polarization-imbalanced NOLM*

During the development of the present thesis, this was the scheme used in the two F8Ls studied (see Fig. 3.1 and Fig. 3.3) to achieve NLPs and then to generate SC; therefore, this Subsection will be explained in more detail. This symmetrical scheme provides a well-defined transmission characteristic through the polarization control at the input and within the loop by means a quarter-wave retarder (QWR) and a highly twisted standard fiber section [69,70].

First of all, to understand how the Kerr effect affects the propagation of light in the NOLM, we can consider the coupled nonlinear Schrödinger equations describing the evolution of polarization in the CW case. In terms of the circular polarization states C^+ and C^- (right and left), and omitting linear birefringence terms, we have

$$\frac{dC^+}{dz} = \frac{2}{3} i\gamma(|C^+|^2 + 2|C^-|^2)C^+,$$
$$\frac{dC^-}{dz} = \frac{2}{3} i\gamma(|C^-|^2 + 2|C^+|^2)C^-, \tag{2.31}$$

where γ is the nonlinear coefficient for linear polarization (Eq. (2.16), with n_2 as the second-order nonlinear refractive index (Kerr coefficient)), and z is the propagation direction [23]. On the right side of Eq. (2.31), SPM and XPM between orthogonal polarization components are being considered. Since the *optical power* is written as $P = |C^+|^2 + |C^-|^2$, and the *first Stokes parameter* on the Poincaré sphere as $A_c = (|C^+|^2 - |C^-|^2)/P$, Eq. (2.31) becomes

$$\frac{dC^+}{dz} = i\gamma P\left(1 - \frac{A_c}{3}\right)C^+,$$
$$\frac{dC^-}{dz} = i\gamma P\left(1 + \frac{A_c}{3}\right)C^-. \tag{2.32}$$

In Eq. (2.32), the Stokes parameter varies during propagation, strictly speaking; however, in a first approximation it can be considered constant (weak nonlinearity limit [71]). The first terms to the right of Eq. (2.32) correspond to the nonlinear phase shift and the last are associated with NPR.

As the name implies, this NOLM switching requires the introduction of some imbalance in the polarization, so that the Kerr nonlinearities are not equal for each beam, and their difference does not cancel when recombined at the output of the device. Unlike the NOLM presented in Subsection 2.7.2.1.1, where it was based on power imbalance (to ensure that the counterpropagating beams acquire different nonlinear phase shifts), the switching of this NOLM is obtained through polarization imbalance in a power-symmetric scheme. From Eq. (2.32), the second terms on the right shows that a NPR difference can occur even if the powers are equal, provided that the Stokes parameters of the two beams and hence, their polarization states, are different. Details of this architecture can be seen in Fig. 2.26, which includes a

symmetrical coupling balanced in power (50/50, ideally), avoiding the limited dynamic range as when a power-asymmetric coupler $r/(1-r)$ is employed, making the device no longer passive as when an amplifier in the NALM case is inserted, or causing losses as when an attenuator in the loop is used. The proposed power-symmetric, polarization-imbalanced NOLM then bases its switching on NPR.

A QWR, inserted into the loop near one of the output ports of the coupler, creates the polarization asymmetry; the clockwise (cw) beam has the same polarization as the input beam just after entering the loop, whereas the counter-clockwise (ccw) beam polarization is modified by the QWR. A delay of a quarter of the wavelength allows to convert the linear polarization ($A_c = 0$) to elliptic or circular polarization ($A_c = \pm 1$) and inversely, thus ensuring a large difference in the NPR factor. It is very important to clarify that the optical activity introduced by twist induces ellipse rotation, but does not modify the ellipticity of the light, so that the Stokes parameters remain constant during propagation (Eq. (2.32)). In fact, if a substantial twist is applied, the standard fiber behaves as an ideal isotropic fiber [72]. In a twisted birefringent fiber, and as far as chromatic dispersion and group velocity mismatch can be ignored [23], the evolution of the nonlinear polarization can be described using the coupled equations in the case of continuous wave [73].

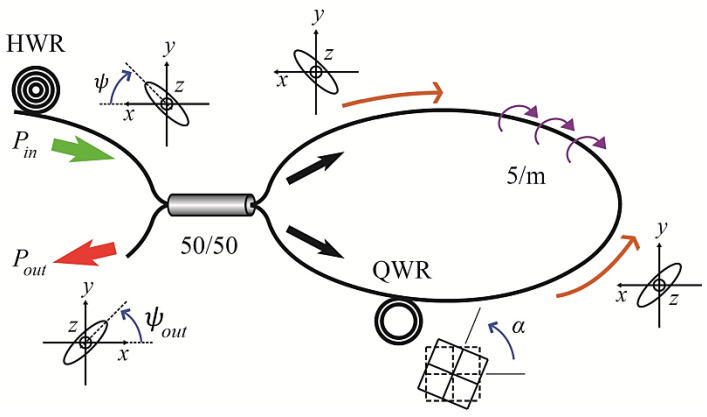

Fig. 2.26. Power-symmetric, polarization-imbalanced NOLM scheme.

In the circular polarization basis, Eq. (2.32) becomes

$$\frac{dC^+}{dz} = i\gamma P\left(1-\frac{A_c}{3}\right)C^+ + i\rho C^+ + i\exp(2iqz)kC^-$$
$$\frac{dC^-}{dz} = i\gamma P\left(1+\frac{A_c}{3}\right)C^- - i\rho C^+ + i\exp(-2iqz)kC^- \tag{2.33}$$

where $\rho = hq/2n$ is the rotational power with n the refractive index and $h \approx 0.13$–0.16 in silica fiber [71], q is the fiber twist rate (rad/m), and $k = \pi/L_B$ is the linear birefringence parameter, with L_B the beat length. The last two terms on the right side of Eq. (2.33) correspond to circular and linear birefringence, respectively. In practice, a few turns per meter (as much as five) may already be considered as high twist, taking into account the relatively large values of L_B associated with residual birefringence in the standard fiber. Next, if terms of linear birefringence are removed from Eq. (2.33) and if A_c is constant (weak nonlinearity approximation), then the two expressions in Eq. (2.33) are decoupled and can be integrated over the length of the fiber. By performing the correct algebraic procedure [69], the output field E_{out} can be calculated as the sum of the fields for *cw* and *ccw* in the output NOLM:

$$E_{out} = E_{out}^{cw} + E_{out}^{ccw} = \begin{bmatrix} C_{out}^+ \\ C_{out}^- \end{bmatrix}$$
$$= \sqrt{\frac{P_{in}}{2}}\begin{bmatrix} U\sin(R_d)\,\mathrm{e}^{i\left(\phi+R_m+\psi+\frac{3\pi}{4}\right)} + V\sin(-R_m+2\alpha)\mathrm{e}^{i\left(\phi-R_d-\psi+\frac{\pi}{4}\right)} \\ U\sin(R_m-2\alpha)\,\mathrm{e}^{i\left(\phi+R_m+\psi+\frac{\pi}{4}\right)} + V\sin(-R_d)\mathrm{e}^{i\left(\phi-R_m-\psi+\frac{3\pi}{4}\right)} \end{bmatrix} \tag{2.34}$$

with

$$R_m = \frac{r_{cw}+r_{ccw}}{2} = \rho L - \frac{\gamma}{12}(A_c^{cw}+A_c^{ccw})P_{in}L$$
$$R_d = \frac{r_{cw}-r_{ccw}}{2} = -\frac{\gamma}{12}(A_c^{cw}-A_c^{ccw})P_{in}L \tag{2.35}$$
$$r_{cw\backslash ccw} = L - (\phi/3)A_c^{cw\backslash ccw}$$

where U and V are the real parameters of the Jones vector from the input field (verifying $U^2 + V^2 = 1$), P_{in} is the power at the NOLM input, L is the loop length for the cw and ccw beams (each of which has a power $P_{in}/2$ after the 50/50 coupler), ψ is the input polarization angle and α is the QWR angle, $\phi = \gamma P_{in} L/2$ is the nonlinear phase shift and, r_{cw} and r_{ccw} are the linear-nonlinear ellipse rotations. Again after some algebra [69], the power transfer characteristic P_{out} of the NOLM writes as

$$\begin{aligned} P_{out} &= \frac{P_{out}}{P_{in}} = \frac{|C_{out}^{+}|^2 + |C_{out}^{-}|^2}{P_{in}} \\ &= \frac{1}{2} - \frac{1}{2}\cos(r_{cw} - 2\alpha)\cos(r_{ccw} - 2\alpha). \end{aligned} \tag{2.36}$$

Simplify Eq. (2.36) without loss of generality, it can be finally rewritten as

$$P_{out} = \frac{1}{2} - \frac{1}{2}\cos\left(\frac{\gamma}{6}A_c^{cw}P_{in}L + 2\alpha\right)\cos\left(\frac{\gamma}{6}A_c^{ccw}P_{in}L + 2\alpha\right). \tag{2.37}$$

Equation (2.37) shows that the NOLM nonlinear transmission characteristic is the product of two sinusoidal functions of power whose periodicities are defined by the Stokes parameters of the counterpropagating beams. If we consider that the coupler does not affect the polarization, $A_c^{cw} = A_c$. In contrast, the Stokes parameter of the ccw beam will be modified by the QWR; rewriting it, it becomes

$$A_c^{ccw} = -\sin(\alpha + \psi)\sqrt{1 - (A_c)^2}\,, \tag{2.38}$$

which depends on both the input Stokes parameter and the orientation of the input ellipse with respect to the QWR angle.

If now, in particular, the input polarization is considered to be circular, left or right ($A_c^{in} = 1, U = 1, V = 0$ or $A_c^{in} = -1, U = 0, V = 1$), it is no longer necessary to take into account the orientation of the input bias ψ, which simplifies NOLM analysis. If the input beam (and hence the cw beam) is circularly polarized, the ccw is

linearly polarized through the QWR regardless of its angle α, as shown from Eq. (2.38) ($A_c^{ccw} = 0$). Then Eq. (2.37) is written as

$$P_{out} = \frac{1}{2} - \frac{1}{2}\cos(2\alpha)\cos\left(\pm\frac{\gamma}{6}P_{in}L + 2\alpha\right). \tag{2.39}$$

The switching power (input power difference between minimal and maximal transmission) in Eq. (2.39) is given by

$$P_\pi = \frac{6\pi}{\gamma L}. \tag{2.40}$$

The dependence of the NOLM transmission on α and P_{in} is illustrated in Fig. 2.27. The sinusoidal low-power transmission is shown in Fig. 2.27(a), obtained from Eq. (2.39) for $P_{in} = 0$; it shows in particular that the QWR orientation α allows adjusting low-power transmission between 0 and 0.5. Otherwise, Fig. 2.27(b) shows that α also allows adjusting the initial slope of P_{out} (which can be made positive or negative), as well as its dynamic range, between 1 (no power dependence) and infinity (zero minimal transmission at low power), with 0 ($\alpha = \pi/4$, black line) and 1 ($\alpha = \pi/2$, red curve), minimal and maximal transmission values respectively.

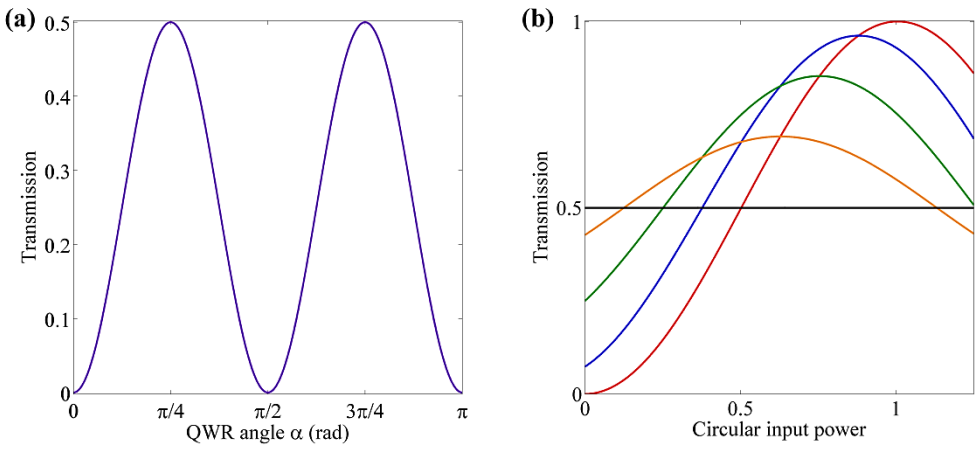

Fig. 2.27. (a) Low-power transmission as function of the angle α (with $P_{in} = 0$); (b) P_{out} under circular input polarization for different values of α ($\alpha = \pi/4 - \pi/2$).

Now, we consider that the input polarization is linear, this means $A_c^{in} = 0$. Hence, using Eqs. (2.37) and (2.38), the power transfer characteristic writes as

$$P_{out} = \frac{1}{2} - \frac{1}{2}\cos(2\alpha)\cos\left(-\frac{\gamma}{6}\sin[2(\alpha+\psi)]\,P_{in}L + 2\alpha\right). \tag{2.41}$$

In practice, linear input polarization (at a specific ψ angle) is obtained from non-polarized light by the use of a properly oriented polarizer. That is why in this case $A_c^{cw} = 0$ and $U = V = \sqrt{2}/2$. Again, the dynamic range and phase of P_{out} depend on α (the QWR angle); but in this case, the switching power depends on both α and the polarization direction ψ:

$$P_\pi = \frac{6\pi}{\gamma L \sin(2[\alpha+\psi])}. \tag{2.42}$$

So that it can be adjusted by tuning any of these two parameters. Under these conditions, it is not convenient to adjust the P_{out} through α as in the circular input polarization case, since the amplitude, phase and period of the sinusoidal dependence are modified simultaneously. In contrast, the input polarization orientation ψ offers a very convenient way to adjust the switching power, without affecting the other parameters. So, α can be set at a fixed value ensuring, for example, an infinite dynamic range.

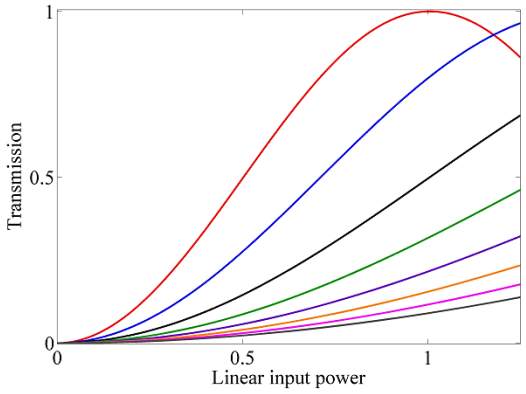

Fig. 2.28. P_{out} under linear input polarization, for different values of the angle ψ ($\psi = \pi/4 - \pi/32$); $\alpha = 0$ in all cases.

The parameter ψ allows adjusting the switching power between a minimal value and infinity, as depicted in Fig. 2.28. When $\psi = -\alpha \pm \pi/4$ occurs the minimal switching power and it is the same as the one obtained in the case of circular input polarization. Indeed, when the linear input polarization makes an angle of $\pi/4$ rad (45°) with the QWR axes, the *ccw* beam polarization is made circular through the QWR ($A_c^{ccw} = 1$), whereas the *cw* beam remains linearly polarized. Counterpropagating beams are thus polarized linearly and circularly in both cases, yielding the same expression for P_{out}. If the input polarization moves away from this orientation, the minimal switching power starts to grow, tending to infinity (if the input polarization is aligned with one of the QWR axes, $\psi = -\alpha$); in this particular case, both counterpropagating beams are linearly polarized, the polarization asymmetry disappears and the transmission no longer depends on power.

2.8 Supercontinuum generation using NLPs: state of the art

The nonlinear phenomenon known as supercontinuum (SC) generation refers to the massive creation of new frequencies beyond the input spectrum via the combination and interaction of multiple nonlinear optical effects such as SPM, XPM, SRS, MI, FWM and the formation of HOS, as it has been shown in various works published on the subject [23,74]. Although it was reported for the first time in 1970 by Alfano and Shapiro [18], the interest to continue developing SC light sources relies mainly on their potential applications, which include optical pulse compression [75], sensing and microscopy [76], telecommunications and optical fiber characterization [77], and imaging (OCT) [78]. As is well known, SC generation can be obtained using different sources for instance, continuous wave (CW) [79,80], ultrashort pulses [81–83], conventional ns-long pulses [20,84–86] and NLPs [4,14–17,87,88].

Nonetheless, in recent years the use of NLPs as the seed to generate wider and flatter SC spectra has gained a particular strength motivated by the need to improve SC sources in terms of efficiency and low cost. Some researchers have reported SC generation using NLPs produced in several fiber laser designs, demonstrating the

benefits of this type of pump pulses. For example, in [5] the authors present a comprehensive review on NLPs, including several SC spectra through these pulses from a ring cavity and different types of fibers, including SMF and HNLF. These spectra, which extend over a few hundreds of nm mainly towards longer wavelengths, contrast in terms of flatness with those generated in the same fibers by ultrashort pulses. In [15], for an average pump power as small as 20 mW, a spectrum over 200 nm at least was obtained in a piece of 750 m of SMF. In [16], by propagating NLPs through 100 m of SMF in the normal dispersion regime, the authors achieved a flat, broadband spectrum of about 200 nm with an average pump power of 3 W. If high laser pump powers are available, flat and broadband spectra covering 200 nm can also be obtained directly at the laser output if a long section of SMF is inserted in the cavity [4,55]. On the other hand, in order to further improve the SC flatness and extension, in particular to the short-wavelength side, some authors proposed using HNLF. In [14], the use of a piece 12-m-long HNLF inside a ring laser cavity allowed the generation of NLPs with a very flat spectrum over a bandwidth of 135 nm (at 3-dB points); a similar result was obtained in [89]. In [87], by adding at the laser output 1-km-long HNLF with near-zero dispersion at the pump wavelength, and for a moderate NLP power (~70 mW), a very broad spectrum of about 950 nm was achieved, extending in both directions and reaching the 2-μm region on the long-wavelength side. In [88], again using a HNLF at the laser output, a spectrum spanning from 1200 to 2100 nm was produced although with a reduced flatness. And in [49], by delivering NLPs into an external piece of 110-m-long HNLF, a flat spectral broadening over 500 nm 20-dB bandwidth on the short-wavelength side was achieved.

Chapter 3. Experimental developments to obtain noise-like pulses

In this Chapter the experimental work directly involved in the obtaining of NLPs carried out during the present thesis is presented. It shows the results obtained and some discussions about them. Section 3.1 presents a first set of experimental results, where fairly stable NLPs of about 350 ps of duration and a moderate output power were achieved in a conventional erbium F8L. Section 3.2 presents a setup which allowed the generation of high-energy NLPs over 300 nJ, where a wide and flat spectrum directly at a double-clad F8L output are also obtained. All these pulses presented in this Chapter will be used in Chapter 4 as the seed for SC generation.

3.1 NLPs through a F8L made up of standard telecom elements

By means of a conventional erbium F8L, NLPs were obtained to be used later as pump in SC generation (at Section 4.1). This F8L of total length of about 218 m (with an overall anomalous dispersion) is formed by a unidirectional ring cavity and a NOLM, as shown in Fig. 3.1. The ring section includes two pieces of erbium-doped fiber (Thorlabs ER30-4/125, EDF1 is 3-m-long and EDF2 is 2-m-long), pumped at 980 nm through a pair of wavelength-division-multiplexing (WDM) couplers. Also, a fiberized optical isolator (ISO1) to ensure unidirectional laser operation, a piece of 100 m of dispersion compensating fiber (DCF, $D = -3$ ps/nm/km), a polarizer (POL) to ensure linear polarization at the NOLM input, and a polarization controller (PC) were inserted. The PC consists of a half-wave retarder (HWR1) and a quarter-wave retarder (QWR1), used to maximize the power transmission through the polarizer. To control the angle of linear polarization at the NOLM input, a second half-wave retarder (HWR2) is implemented. The NOLM is a power-symmetric,

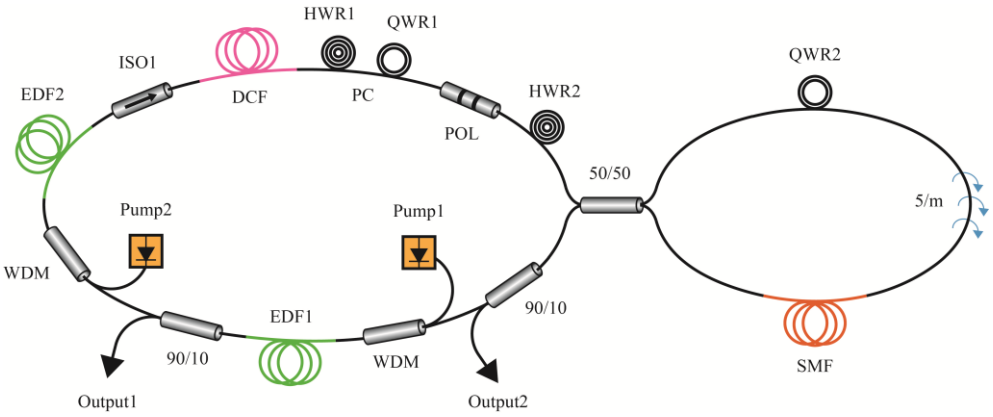

Fig. 3.1. F8L setup for the obtaining of NLPs.

polarization-imbalanced scheme, whose switching relies on NPR in the twisted loop (see Subsection 2.7.2.1.3) [71]; it is made of a 50/50 coupler, 100 m of low-birefringence SMF (D = 17 ps/nm/km) twisted at a rate of 5 turns per meter, and a quarter-wave retarder (QWR2) to break the polarization symmetry [69]. Finally, the output ports are provided by two 90/10 couplers, being the output 2 to monitor the pulses.

At proper configuration of the wave retarders, self-starting fundamental ML operation was obtained, and a nearly stationary NLP regime was achieved with some adjustments. Figure 3.2(a) presents the NLP envelope measured at output 2 with a 25-GHz photodetector and a 16-GHz real-time oscilloscope, which allows estimating a mean full-width at half-maximum (FWHM) pulse duration of 350 ps (average of 1000 traces). The pulse train was fairly stable (inset) with a period of T = 1.106 μs (which corresponds to a repetition rate of 904 kHz) and with an estimated pulse power of 100 W.

To verify that the obtained pulses were NLPs, besides their temporal profile, the optical spectrum and the autocorrelation trace were measured. For the former, we use an optical spectrum analyzer (OSA, Anritsu MS9740A) at output 2, measuring an average smooth and wide spectrum with a maximum at 1567 nm (Fig. 3.2(b), solid red line), with 13.4 nm 3-dB bandwidth and 53.4 nm 20-dB bandwidth (values at 3 dB do not show enough extension to correctly describe the actual extent

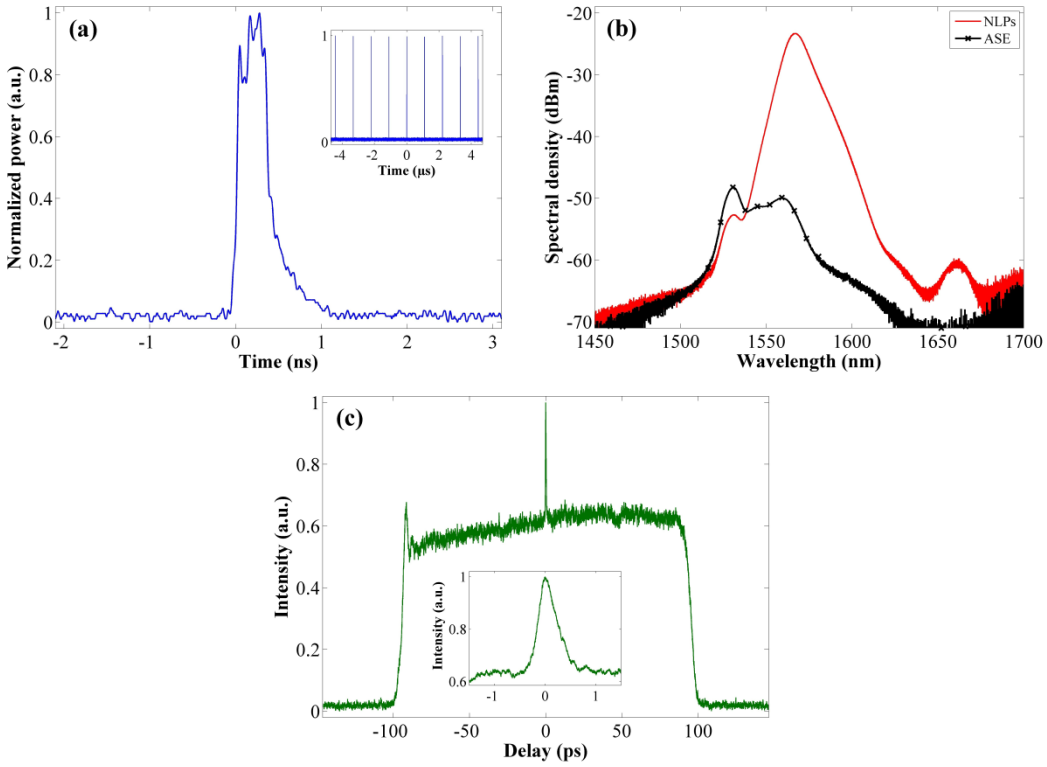

Fig. 3.2. NLPs fundamental mode locking: (a) time-domain envelope measured using a scope in average mode (inset: pulse train); (b) optical spectrum in mode locking regime and ASE emission below lasing threshold; (c) intensity auto-correlation trace of pulses (inset: close-up on central spur).

of the SC spectra, as we shall see below, we also present the bandwidth values measured at 20 dB of the maximum). A small shoulder attributed to amplified spontaneous emission (ASE) appeared at 1531 nm; this attribution was confirmed by the presence of a peak at the same wavelength in the spectrum measured below the lasing threshold (Fig. 3.2(b), marked black line). Besides, a small peak corresponding to the maximum of the Raman gain appeared at 1661 nm. Intrapulse Raman scattering (self-frequency shift) is may be present evidenced by the slight asymmetry of the main spectrum at 1567 nm and its red shift with respect to the gain maximum at 1557 nm. Finally, Fig. 3.2(c) shows the autocorrelation trace exhibiting a typical double-scaled structure with an ultrashort coherence spur of 391 fs (inset)

riding upon a broad pedestal of 189.5 ps (corresponding to the measurement window of the autocorrelator, narrower than the duration of the whole packet); the level of the pedestal is related to the density of the sub-pulses in the bunch and the statistical distribution of their intensities. Due to probably imperfect alignment of the autocorrelator (FR-103XL), the trace shows a slight left-right asymmetry.

3.2 High energy noise-like pulsing in a F8L without a polarizer

A different experimental configuration, shown in Fig. 3.3, is a F8L of about 215 m of length (at anomalous cavity dispersion), formed also by a ring cavity and a NOLM. In the ring section, a 980/1550 nm beam combiner was used to launch the pump power (6.5 W) from a 980 nm laser diode into the cavity. The active fiber is a piece of 1.6-m-long Nufern erbium/ytterbium double-clad fiber (EYDCF) with a core diameter of 12 µm (NA = 0.20) and an inner cladding diameter of 130 µm (70-dB/m core absorption at 1530 nm). A fiberized polarization-independent optical isolator (PI-ISO) is inserted to ensure unidirectional laser operation. It also includes a piece of standard fiber (SMF1, D = 18 ps/nm/km) of about 200 m of length and a polarization controller (PC) composed by QWR-HWR-QWR plates. The output port is provided by a 90/10 coupler, with the 90% output port connected to the combiner, closing the cavity. A power-symmetric, polarization-imbalanced NOLM scheme is used as the SA, consisting of a 50/50 coupler, a 10-m-long SMF2 twisted at a rate of 5 turns per

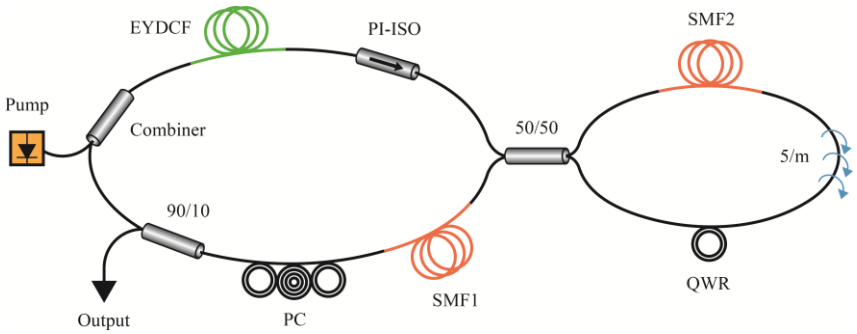

Fig. 3.3. F8L setup for the generation of high-energy NLPs.

meter, and a QWR inserted asymmetrically in the loop in order to break the polarization symmetry. It is very important to remark that in the present setup (Fig. 3.3) the state of polarization in the cavity is not fixed because of the absence of a polarizer, contrary to the previous scheme (Section 3.1) and other similar schemes reported formerly [6,90–92].

For appropriate settings of the PC and QWR we obtain a nearly stationary self-starting fundamental mode locking operation, as can be seen in Fig. 3.4(a), after 10 W of pump power. In single-shot acquisition mode, we observe a NLP envelope with FWHM pulse duration of ~13 ns and an estimated power of 6 W. For the maximal input power (25 W), the power reached by the envelope was about 23.3 W. The pulse was measured in the time-domain using a 2-GHz photodetector and a 2-GHz oscilloscope, with a period of T = 1.1 μs (inset of Fig. 3.4(a)), which corresponds to a fundamental repetition rate of 909 kHz. This result confirms that a polarizer at the input of the polarization-imbalanced NOLM is not necessary to obtain the mode locking regime in this scheme, although NPR may present and affect the operation even without polarizer because NOLM transmission depends on polarization. Nonetheless, the absence of a SA effect in the ring section was further confirmed by observing that, when we tested the setup (Fig. 3.3) prior to the NOLM insertion, no ML operation could be obtained from this ring laser configuration.

Likewise, in order to further confirm the NLP regime, the optical spectrum and the autocorrelation trace were obtained. A broad and flat SC spectrum extending over 200 nm (Fig. 3.4(b), solid red line) directly at laser output, whose measurement unfortunately limited on the right side by the range of the available OSA (Anritsu MS9740A) was achieved. The spectral maximum appears at 1566.5 nm in the region of erbium emission, with a pair of peaks close to 1536 nm and 1543 nm, which are attributed to residual CW emission. This spectrum also presents a significant red-shifted component that decays smoothly by 15 dB over 150 nm, from 1600 nm to the upper limit of the OSA (1750 nm). The 3-dB bandwidth of this spectrum is 18 nm, corresponding to the peak of erbium emission; however, it reaches 75 nm at 10 dB

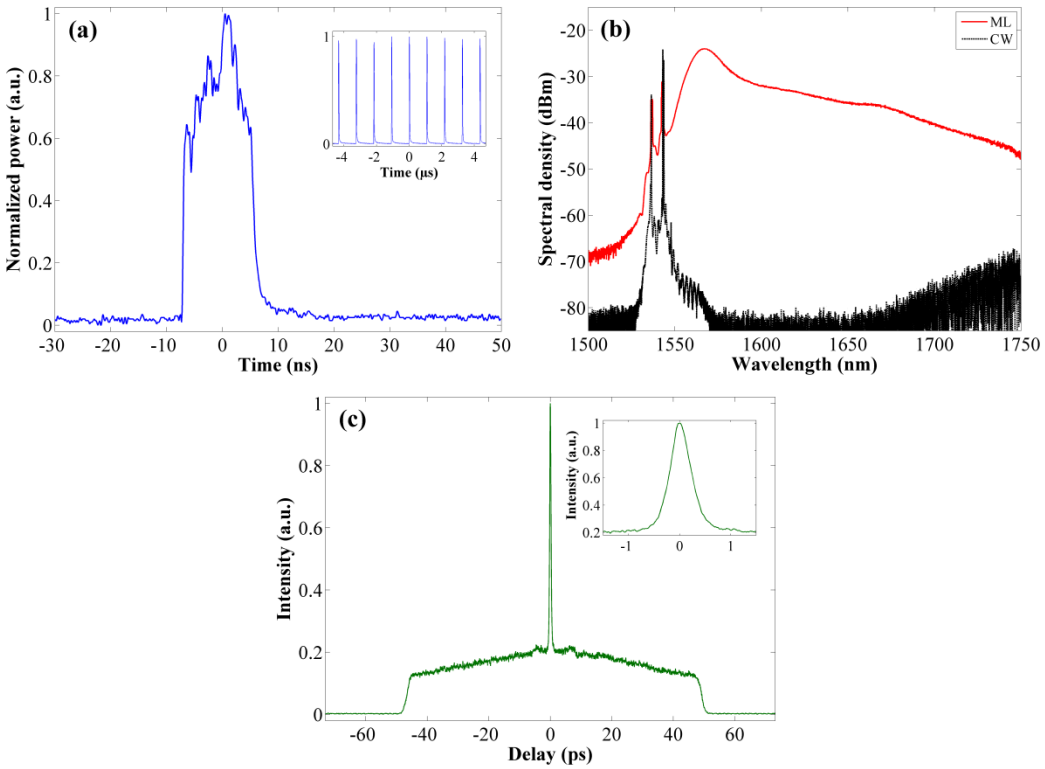

Fig. 3.4. Noise-like pulses fundamental mode locking: (a) time-domain envelope in single-shot mode (inset: pulse train); (b) optical spectra in mode locking and CW regimes; (c) intensity autocorrelation trace of pulse (inset: close-up on central spur).

and 145 nm at 15 dB from the peak. It is evident that when there is no ML operation, the spectrum (Fig. 3.4(b), dotted black line) is much narrower and only presents a few peaks in the erbium emission band at the mentioned wavelengths. Finally, the autocorrelation trace was obtained using an autocorrelator (FR-103XL) and a scope. A typical NLP double-scaled autocorrelation trace was obtained, with a narrow coherence peak riding a wide and smooth pedestal that extends beyond 200 ps, limited by the range of the autocorrelator as can be observed in Fig. 3.4(c). In spite of this, the pedestal presents a marked slope that allows estimating its extension to a few hundreds of ps (much narrower than the duration of the whole bunch), which is

consistent with the existence of sub-ns substructures within the NLPs. The peak-to-pedestal ratio is ~5:1, and the inset of Fig. 3.4(c) shows a close-up on the central spur with a FWHM time duration of about 1 ps.

It is noteworthy that a maximal average output power of 275.25 mW was measured with a maximal pump power of 25 W, in the fundamental ML regime. And although it corresponds to a laser efficiency slightly lower than 1%, the single pulse energy in this nearly stationary NLP regime is estimated to be 302.8 nJ, which was to the best of our knowledge the highest single NLP energy directly at the laser output reported at the time this result was published [4]. Recently a paper was published where authors presented NLPs with energy of 560 nJ without pulse splitting in a ring laser cavity [93]; these pulses that the authors call "self-mode-locked NLPs" have a temporal duration of hundreds of ns, so is not surprising that they reach such energy in this case. Nonetheless, authors did not present the autocorrelation trace, which is essential to know if the pulses are actually NLPs (Cfr. Subsections 2.5.3.1 and 2.5.4).

One of the factors that generally limit the maximum pumping energy in ML pulses, including NLPs, is the splitting that they suffer. The absence of a polarizer in the present scheme may be connected with the enhanced NLP properties, because the state of polarization along the cavity is no longer restricted; this means that the laser radiation has greater freedom to self-adjust, adapting its polarization and thereby selecting the NOLM switching power, in order to optimize the mode locking operation.

The low value of laser efficiency can be attributed mainly to the location of the output coupler in the scheme in Fig. 3.3, and to its coupling ratio. Inserting this coupler after the EYDCF, at the point where intracavity power is the highest, would improve the output power and the efficiency, which is currently affected by the PI-ISO insertion loss (~2 dB) and the nonlinear loss introduced by the NOLM. Besides, the output power and the efficiency of the laser could be maximized by optimizing the coupling ratio of the output coupler, by reducing splice losses between SMF and EYDCF

(caused by mode field diameter mismatch), and choosing a better length in the latter fiber.

Otherwise, a less stationary NLP regime was observed by varying the PC configuration, as can be seen in Fig. 3.5. In the first five planes of this figure we can see different samples of the waveform (in single-shot acquisition mode), where the presence of sub-pulses with an average duration on the order of ~1 ns is clearly visible. On the left side of the NLPs, towards shorter times, the waveform is compact and displays a steep slope, whereas on the right, the waveform tends to split into multiple sub-pulses with random temporal distribution; here we can see that their amplitudes decline smoothly from left to right, until they disappear completely on the scope. This smooth decay at the right side of the waveform is also visible in the last plane of this figure, where 10000 traces are averaged (labeled "Av"). This regime is similar to the dynamics reported in [6,7], where sub-structures at sub-ns scale were found to be released from the NLP, drifting away from the main packet on the right side and decaying progressively with increasing distance. It should be mentioned that in this part of the experiment, the optical spectrum and the autocorrelation trace are practically the same as those of Fig. 3.4.

It is noteworthy that mode locking is self-starting in all cases if the pump power is higher than 7 W, remaining stable for hours. Nonetheless, with some mechanical

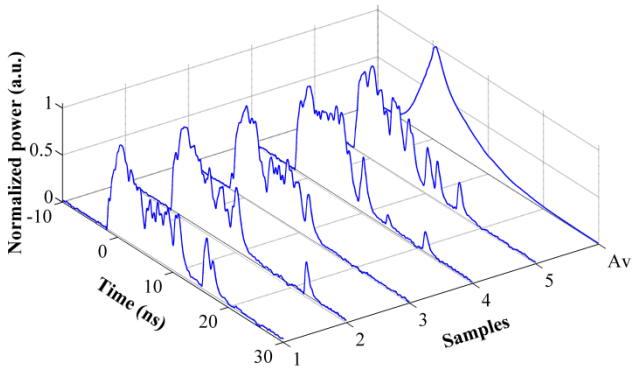

Fig. 3.5. Temporal profiles showing a less stationary NLP regime than in Fig. 3.4(a).

stimulation, it was possible to obtain mode locking at lower pump power. Once this regime is achieved, stable single-pulse operation is maintained although pump power is increased, even if it is tuned to the highest level (25 W), unlike results reported in other references where the main packet splits into several pulses if pump power is increased beyond some point [5,54].

On the other hand, from stable fundamental mode locking operation, slight QWR adjustments at high pump power allow observing a transition to multiple pulsing operation in the form of stable harmonic mode locking (HML) up to the 6th order, as shown in Fig. 3.6.

However, it can be seen how the pulse train is affected by amplitude fluctuations when the harmonic order increases. This regime allows the spectrum to be considerably flattened, especially when the order is large, as will be seen in Section 4.2. Although HML was evidenced, the low order values achieved in this development (only up to 6, which contrasts with more than 1000 in [54,94]) are consistent with the reduced tendency of the NLP to split into multiple pulses in the present scheme.

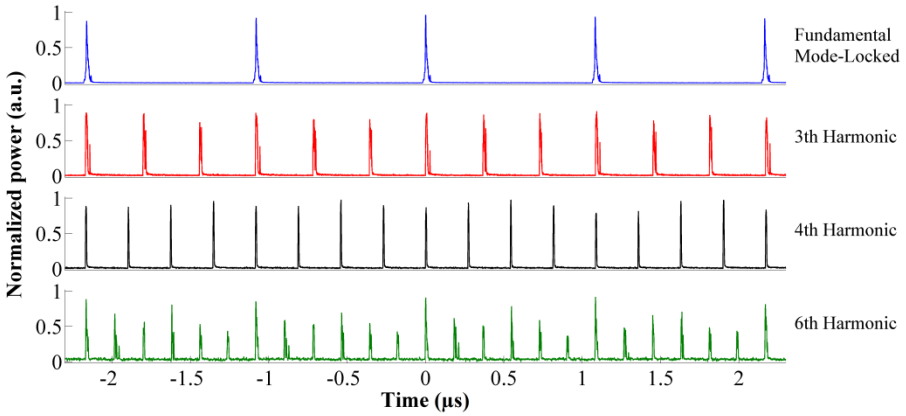

Fig. 3.6. Scope traces of harmonic mode locking up to the 6th order.

Chapter 4. Experimental SC generation using NLPs as pump

This Chapter is focused on the SC generation using the NLPs obtained by the two previous different F8Ls presented in Chapter 3. Section 4.1 shows the generation of very broad (almost 1000 nm) and flattened spectra by varying the length of a nonlinear medium outside the conventional F8L. In Section 4.2, the flattening of the SC spectrum directly achieved at the erbium/ytterbium double-clad F8L output is discussed in the harmonic mode locking regime. Finally, Section 4.3 presents the broadening of this SC spectrum with high-energy NLPs by adding a piece of HNLF.

4.1 Very wide and flattened SC spectra amplifying an external nonlinear medium composed by SMF and/or HNLF

To generate SC with those NLPs produced with the conventional F8L presented in Section 3.1, an external stage consisted of an EDF amplifier and a nonlinear element was implemented. At the output 1 of the F8L at Fig. 3.1, an isolator (ISO2) was placed to protect the laser cavity from the ASE and avoid destabilizing the NLP operation. As shown in Fig. 4.1, the amplifier includes a piece of 4-m-long EDF3 (same kind as in the F8L (Fig. 3.1)) pumped at 980 nm through a WDM coupler, with the optimal length to achieve better results (amplified average powers of 25 mW and 35 mW were used, the latter resulting in slightly broader SC spectra, as presented below). To monitor the pulses at the EDF3 input and output, two ports are provided by 99/1 couplers. Finally, as the nonlinear media to generate SC, we use several 2-by-2 combinations of spools of various lengths of SMF and/or high-nonlinearity fiber (HNLF, with high-index core surrounded by a deeply depressed ring yielding a mode field diameter of 3.9 μm, nonlinear coefficient of γ = 10.8/W/km, 1550-nm zero-dispersion wavelength, dispersion slope of 0.006 ps/nm^2/km).

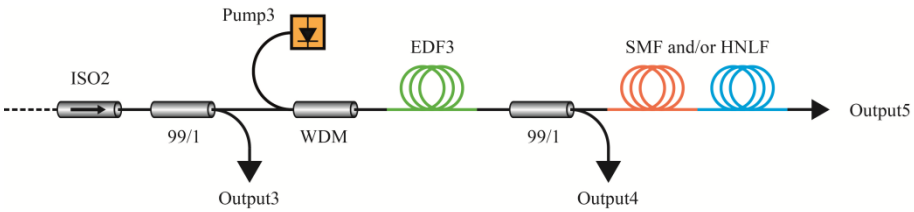

Fig. 4.1. External amplifier and nonlinear element for SC generation.

Once the stationary NLP operation was confirmed (Section 3.1), the pulses at output 1 in Fig. 3.1 were amplified using the scheme depicted in Fig. 4.1, and the resulting pulses were launched into the nonlinear element. As reference, the spectrum was measured directly at the output of the amplifier (Fig. 4.1, output 4). With 25 mW of average power at the EDF3 output, the spectrum (Fig. 4.2(a) and Fig. 4.3(a), cyan crosses line) presented a maximum at ~1563 nm and 21 nm 3-dB bandwidth (64 nm at 20 dB). The presence of residual pump at the amplifier output was attested by a narrow peak at 976 nm flanked by a pair of lobes (~900–1040 nm), as can be seen in the inset of Fig. 4.2(a). This structure presented its second-order diffraction at 1952 nm, with a similar pair of lobes (~1830–2130 nm). Due to the extension of the SC spectra discussed below, measurements required the simultaneous use of two Yokogawa optical spectrum analyzers (OSA AQ6370B and AQ6375), whose data were merged.

In a first set of experiments, the performances of SC generation through different lengths of SMF only were analyzed. During measurements, the average power of the injected NLPs was maintained constant at 25 mW. Figure 4.2 presents the results obtained with spools of 50 m, 100 m, 315 m, 600 m and 1000 m; for comparison, OSAs noise is also shown. For a fiber of 50 m, no spectral broadening is observed at the fiber output, and the resulting curve is indistinguishable from the input spectrum (labeled “0 m” in Fig. 4.2(a)). Then, with a length of 100 m, spectral broadening becomes noticeable, taking place exclusively towards longer wavelengths. As fiber length is increased, the spectral maximum in the 1560-nm region slightly shifts to the

right. The maximal spectral extension was reached with 315 m of SMF; in such a case, the spectrum covers more than 300 nm, from the 1560-nm region to ~1850 nm, where a secondary maximum (a hump) is observed. Here, the 20-dB bandwidth reaches a maximum of 323 nm, as depicted in Fig. 4.2(b). In spite of this, a relatively poor flatness is observed at this stage, as attested by the moderate value of the 3-dB bandwidth (~25 nm). If next the fiber length is further increased, spectral components grow in the 1700-nm region, filling the gap between the two maxima, which results in an improved spectral flatness. Therefore, the 3-dB bandwidth increases to ~40 nm with 600 m and 1000 m of SMF. In addition to an improved flatness, extending the fiber length beyond 315 m also has the consequence of reducing the long-wavelength limit of the spectrum. This effect is attributed to higher fiber losses when the 2-µm region is approached. As a result, the 20-dB bandwidth decreases to 247 nm for the 1000-m piece of fiber. Hence, although nonlinear effects are still operating after 500 m of SMF, fiber losses ultimately limit the maximal fiber length and the maximal spectral extension of the SC, as can be seen in Fig. 4.2(b); this figure is a nice illustration of the limits of using the 3-dB bandwidth alone for assessing the spectral extension of the SC. In particular, when the SMF length is extended beyond 315 m, the 3-dB bandwidth increases, although the 20-dB bandwidth actually decreases.

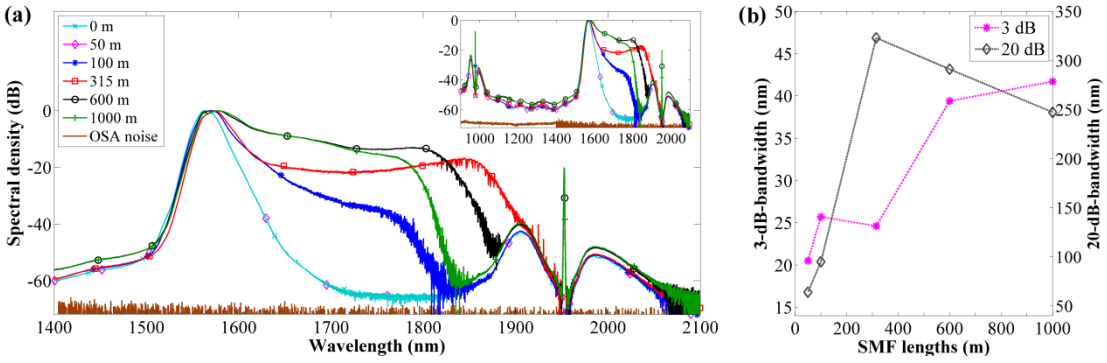

Fig. 4.2. (a) SC spectra at the output of the nonlinear element formed with SMF (inset: spectra with extended span including the residual pump); (b) evolution of bandwidths at 3 and 20 dB from the maximum, for the different lengths of SMF.

After this past is finished, a piece of HNLF of 50 m of length was added to each of the previous SMF spools, with the intention to further extend the spectrum, mainly towards shorter wavelengths. During measurements, the average power of the injected NLPs was again maintained constant at 25 mW. The results are presented in Fig. 4.3. Because the 50-m-long piece of SMF did not show measurable effects, it was omitted in this section.

At the beginning of this second set of experiments, the spectrum produced by the 50-m-long HNLF without SMF was studied (Fig. 4.3(a), orange triangles line); at 976 nm, spectra show the residual pump with a replica at double wavelength. In this case, the spectrum extended not only to the right but also to the left, reaching a bandwidth of 224 nm at 3 dB from the maximum and 542 nm at 20 dB, with the spectral maximum centered at ~1561 nm. This and the subsequent spectra overall were very smooth, although they presented two regions of water absorption bands: at 1350–1410 nm and 1800–1950 nm; these features were caused by the 30% humidity prevailing in the laboratory during the measurements. From ~1520 to 1550 nm, a small shoulder appeared with two humps, which can be attributed to ASE (see Fig. 3.2(b), marked black line).

If now the HNLF is preceded by a 100-m piece of SMF, the spectrum is further extended in both directions, covering 647 nm at 20 dB from the maximum. However this spectrum also presents a higher concentration of energy in the 1800-nm region, reducing the flatness. For the combination of 315 m of SMF plus the HNLF, the flattest and most extended spectrum is obtained (at 25-mW average power), with 234 nm 3-dB bandwidth and up to 772 nm at 20 dB, spanning from the 1260-nm region to 2040 nm (red squares line in Fig. 4.3(a), as well as in Fig. 4.4 and 4.5(a)). Finally, if the SMF piece is further extended to 600 m or 1000 m, the SC extension reduces significantly and it becomes comparable to the case of HNLF only; the benefits of using SMF in combination with the HNLF section to enhance spectral broadening thus vanish in these cases. This is probably due to the larger attenuation in long sections of SMF, in particular towards 2 microns. Hence, similarly to the first set of experiments, it turns out that attenuation sets an upper limit to the fiber length and

to the SC extension. Again, the evolution of bandwidths at 3 dB and 20 dB as SMF length is increased is presented (Fig. 4.3(b)).

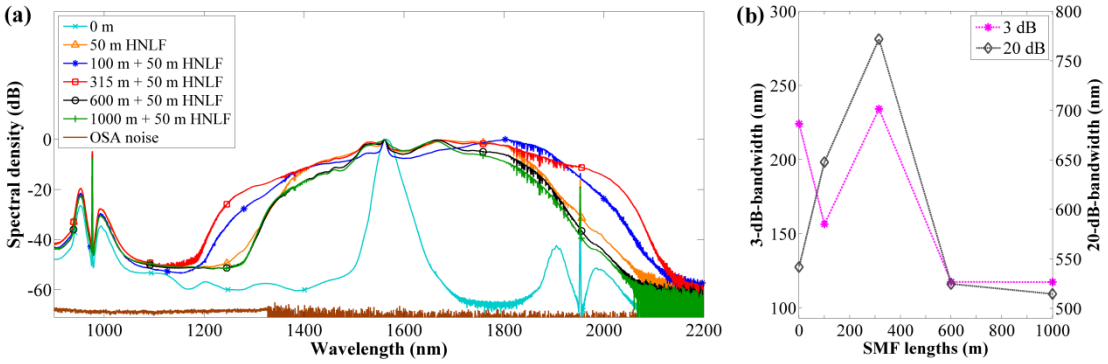

Fig. 4.3. (a) Extended SC spectra at the output of the nonlinear element formed with SMF plus HNLF (the 976-nm region of the spectra show the residual pump with a replica in the 1952-nm region), OSA noise is shown for comparison; (b) evolution of bandwidths at 3 and 20 dB for the different lengths of SMF plus 50 m of HNLF.

Finally, measurements were repeated with the SMF and HNLF fibers combined in the inverse order. For all lengths of SMF, the obtained spectra were similar to the case of the HNLF only, so that no benefit was obtained by using the SMF together with the HNLF in that configuration. This result could be related to losses of the taper at the HNLF output.

The most extended spectrum, towards both longer and shorter wavelengths obtained with the 315-m-long SMF plus 50-m-long HNLF, was presented in Fig. 4.3. The effect of replacing this piece of 50-m HNLF with a 100-m piece of the same fiber is depicted in Fig. 4.4. The differences between the two spectra demonstrate that the nonlinear effects continue to take place beyond 50 m of propagation in the HNLF; however, the main effect of lengthening the HNLF is a higher concentration of energy in the 1800–2000-nm region, which rises above the pump peak in the

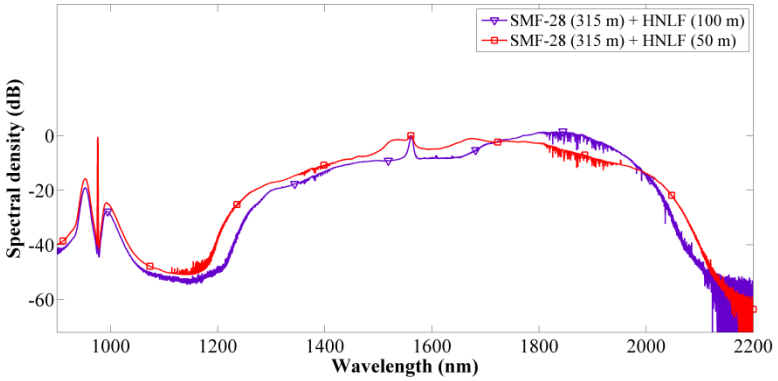

Fig. 4.4. Comparison of SC spectra by combining 315 m of SMF with 50 and 100 m of HNLF (in the 100-m-HNLF case the SC intensity in the 1900-nm region does not allow to see the replica of the residual pump). For the sake of comparison, both curves are normalized with respect to the residual peak in the 1560-nm region.

1560-nm region and reduces the SC flatness. Besides, the overall extension of the spectrum is slightly reduced on both sides (from 772 nm to 726 nm at 20-dB bandwidth), again presumably due to higher losses when fiber length is increased.

As a final point, Fig. 4.5(a) presents the evolution of the SC spectrum when the input power is varied by adjusting the pump power of the EDF3 amplifier. Again, choosing the combination of 315 m of SMF and 50 m of HNLF, this figure shows how the spectrum widens roughly symmetrically on both sides of the spectral maximum and how it becomes progressively flattened as the power level increases. The maximal spectral extension is reached (grey down triangles line; reproduced in Fig. 4.5(b)) by setting the maximum pumping level of the amplifier (408 mW, which corresponds to 35 mW average power of the injected NLPs). Although the spectrum presents a substantial reduction of its 3-dB bandwidth (167 nm) compared with the 25-mW case, its 20-dB bandwidth is as broad as 808 nm, extending from 1263 to 2071 nm. Its flatness is best characterized by considering that its bandwidth extends over 431 nm at 5.7 dB from the peak (1504–1935 nm), over 595 nm at 10 dB, and over

1000 nm at 50 dB, as can be seen in Fig. 4.5(b); also this spectrum presents an excellent dynamic range over 60 dB. It should be noted that we are not considering the water absorption bands in these measurements since they can be eliminated by controlling the humidity of the laboratory.

It can be seen that in this systematic and comparative study of SC generation, we obtained very wide and flattened spectra using NLPs with very low average power as the seed, through different pieces of various lengths of standard and HNLF and their combinations. Here we want to stress that the power reached by the envelope of the NLPs was about 100 W.

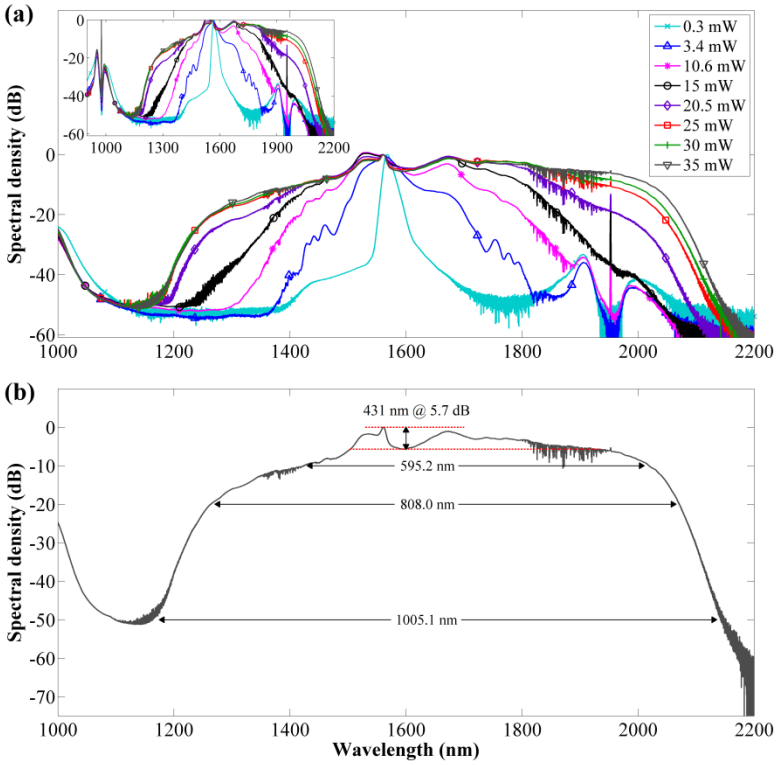

Fig. 4.5. (a) Evolution of SC spectrum by varying the amplifier pump power in the combination 315 m of SMF plus 50 m of HNLF (inset: spectra with extended span including the residual pump); (b) Maximal spectral extension with 315 m of SMF plus 50 m of HNLF (35 mW average input power).

In summary, when pieces of SMF of several hundreds of meters are pumped by NLPs, the spectrum extends to longer wavelengths (covering more than 300 nm for a SMF length of 315 m). As the fiber length is further extended, the spectral flatness improves whereas the long-wavelength edge of the spectrum erodes as a consequence of high fiber losses near 2 µm. Next, using a HNLF with zero dispersion at 1550 nm, bilateral spectral broadening is achieved; the nearly symmetrical broadening in Figs. 4.3–4.5 suggests that, besides the Raman and Kerr effects, parametric nonlinear phenomena such as DFWM are involved and play a major role. Here, the broadest and flattest spectrum is obtained with a piece of 315 m of SMF followed by 50 m of HNLF, reaching about 1000 nm of extension, with an excellent flatness over a region of 430 nm at 5.7 dB. Besides it has an outstanding dynamic range as high as 60 dB, which makes it an excellent source for some applications such as OCT or spectral device testing. It should be noted that the analysis carried out here indicates that nonlinear processes are still operating due to the NLPs characteristics after propagating into fibers of hundreds of meters in length, eventually limited to longer wavelengths by the strong fiber attenuation in the 2-µm region.

4.2 Flattening of SC spectra through high-energy harmonic NLPs

Through the high energy noise-like pulsing from the Er/Yb double-clad F8L presented in Section 3.2, flattened spectra were obtained by increasing the harmonic mode locking (HML) order and varying the length of the standard fiber (SMF1 in Fig. 3.3) in the ring section (from about 200 m to almost 1 km) [55].

A first important result obtained with this setup is the broad and smooth optical spectrum directly at the F8L output, presented previously (Section 3.2), obtained in the fundamental mode locking regime (T = 1.1 µs) which extends over more than 200 nm (Fig. 3.4(b)). And although these measurements are limited on the right side by the range of the available OSA (Anritsu MS9740A), they are at least comparable with those obtained in previous studies [14,89].

We observe that incrementing the HML order (number of equidistant identical pulses coexisting in the cavity) of the high-energy NLPs through some PC adjustments, the SC spectrum can be improved in flatness as shown in Fig. 4.6, from more than 20 dB with the fundamental ML up to ~15 dB with the third harmonic, in the 1580-nm region to 1750 nm (up to ~10 dB between 1580 and 1700 nm). This may be due to the fact that the spectra are generated by different pulses in the cavity, making it flatter because of the averaging, as the order of harmonics increases.

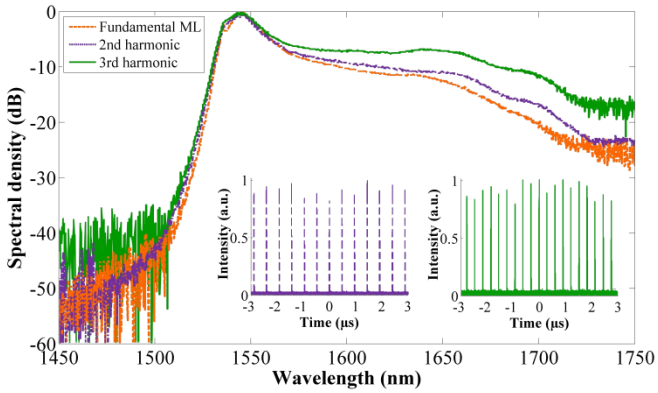

Fig. 4.6. Improved SC spectra obtained in second and third HML (~200 m of SMF1 in the cavity); inset: output pulse trains for second and third HML.

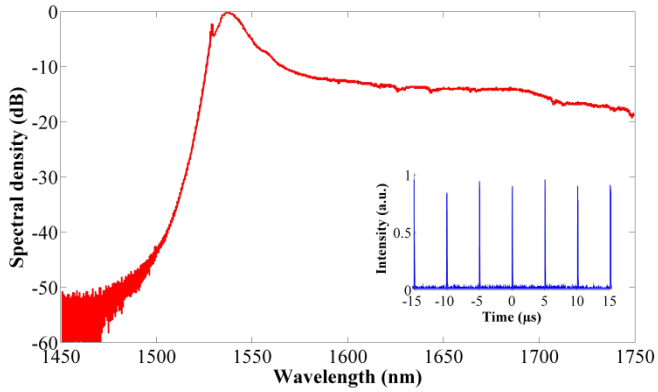

Fig. 4.7. SC spectrum obtained with the fundamental mode locking of the F8L using ~980 m as SMF1 in the cavity; inset: output pulse train.

On the other hand, by increasing the length of the SMF1 in the ring section of the F8L, a further flattening is obtained with regard to the original spectrum (Fig. 3.4(b), as depicted in Fig. 4.7. Using about 980 m as SMF1, a spectrum with a flatness of about 15 dB in the 1580-nm region to 1750 nm was achieved, with a pulse train period of T = 5 μs (inset), which corresponds to a repetition rate of 0.2 MHz in the fundamental mode locking.

Next, with the appropriate configurations of the PC, second and third harmonics were also obtained using the 980 m as SMF1, as depicted in Fig. 4.8, where a better flatness of less than 10 dB was achieved in the same region. Finally, Fig. 4.9 shows the improved SC spectrum obtained when a HML order as high as 100 is reached. The flatness increased significantly with greater length of the cavity (SMF1) and HML order, obtaining an excellent flatness less than about 3 dB, over at least 160 nm (1580–1750 nm) and possibly beyond (measurement limited by the range of the available OSA).

High HML allows the use of the source of NLPs as a SC source with potential applications. The advantages of the use of NLPs for SC generation are related to characteristics of these pulses formed in passively mode locked (PML) laser systems. We can see that the spectral flatness and smoothness exhibited by the present SC source based on NLPs suggests a mechanism similar to SC generation pumped with conventional ns-long pulses in the anomalous dispersion regime, where modulation instability (MI) causes the temporal breakup of the long input pulses and transforms them into a bunch of numerous stochastic fs-scale pulses in the initial phase before a dramatic spectral expansion takes place [95]. However, the use of NLPs as seed for the SC generation allows skipping the step of fragmentation of the conventional ns-pulses. Then, the spectra are dramatically extended driven by the fs-pulses dynamics, where the Raman-induced soliton self-frequency shift (SSFS) is mainly responsible for the generation of long-wavelength spectral components.

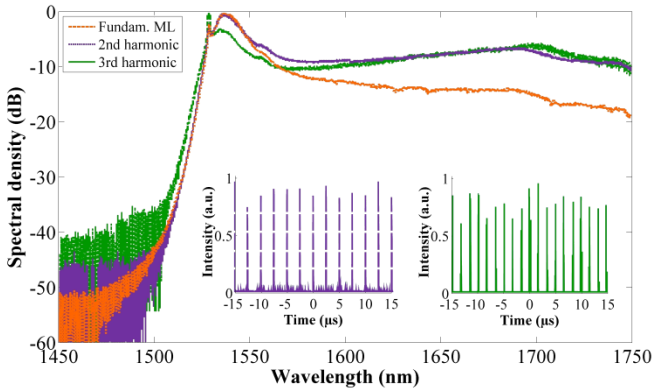

Fig. 4.8. Improved SC spectra obtained through second and third HML pulse regime (~980 m of SMF1 in the cavity); inset: output pulse trains for second and third HML.

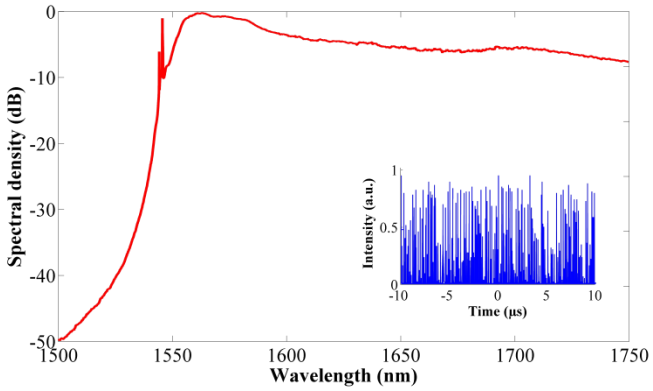

Fig. 4.9. High flattened SC spectrum obtained through the 100th HML order (~980 m of SMF1 in the cavity); inset: output pulse train.

4.3 Enhancement of SC launching the high-energy NLPs into a HNLF at the laser output without external amplification

Finally, in order to enhance the spectral broadening of the high-energy NLPs (setting again the laser in a stable fundamental regime, such as the one depicted in Fig. 3.4(a)), we spliced at the F8L output a piece of 100-m-long HNLF (the

available same kind of HNLF as in the previous scheme). An extended SC spectrum to both sides covering 450 nm, from below 1300 nm to 1750 nm (limited again by the OSA, Anritsu MS9740A) was observed, depicted in Fig. 4.10. Because of the prominence of the peak of erbium emission in the 1550-nm region, the 3-dB bandwidth is only of 30 nm; however, the bandwidth is as large as 375 nm at 15 dB and 400 nm at 20 dB from the peak. It has to be stressed that the use of an unpumped spool of HNLF at the Er/Yb F8L output results in a widening of the spectrum on the order of hundreds of nm not only towards longer wavelengths but also toward shorter wavelengths (down to 1300–1400 nm) with respect to the spectrum measured directly at the laser output (Fig. 3.4(b)). This result is quite similar to the case of the externally amplified HNLF in Section 4.1.

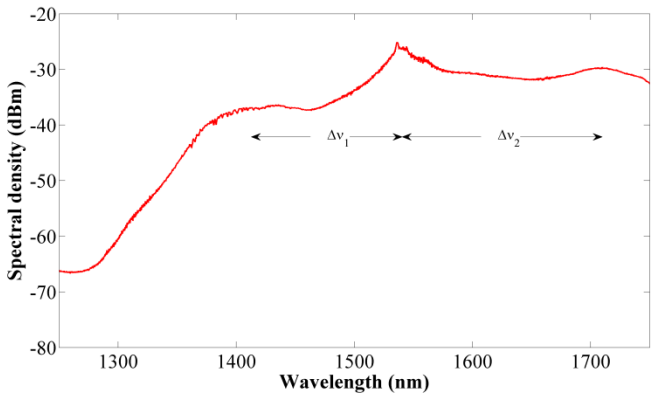

Fig. 4.10. Extended SC spectrum of fundamental mode locking with a 100-m-long HNLF at the laser output without an external amplifier.

It can be seen that there are a couple of very marked shoulders on either sides of the spectral maximum at 1536 nm: around 1400 nm and 1700 nm. To locate those peaks in terms of frequencies in relation to the central peak, we use the expression

$$\Delta\nu = \left|\frac{c}{\lambda_f} - \frac{c}{\lambda_c}\right|, \tag{4.1}$$

where λ_{f_1} = 1400 nm and λ_{f_2} = 1700 nm, and λ_c = 1536 nm. Therefore, we have that $\Delta\nu_1 = 18.96$ THz and $\Delta\nu_2 = 18.83$ THz, as depicted in Fig. 4.10; this means that these lateral shoulders are equidistant from the central peak in terms of frequency. Hence, we show that they are due to DFWM because the HNLF has zero second-order dispersion at 1550 nm, which favors phase-matching (see Subsection 2.4.6). Besides, according to the asymmetric shape of the spectrum, we conclude that intrapulse Raman scattering (self-frequency shift) also plays a part. In contrast, no SRS peak is observed at ~1660 nm, which is consistent with the fact that the SRS threshold is higher than the FWM threshold under phase matching conditions [23].

The results obtained in this experimental development were mainly due to the NLPs characteristics. In the scheme depicted in Fig. 3.3, NLPs could adopt different polarization states, corresponding to different switching powers (see Subsection 2.7.2.1.3). More generally stated, by allowing polarization to adjust freely, the absence of a polarizer in the present scheme adds an additional degree of freedom to the already complex nature of NLPs, and this may constitute a key ingredient to overcome the limitations imposed by the laser cavity on the pulse energy and bandwidth. The idea of the absence of a polarizing element may improve the NLP characteristics, in particular their spectral bandwidth and energy. Increasing the cavity length is a well-known strategy to increase the pulse energy; however, pulse splitting may set an upper limit to this energy, something we controlled at will in the present study because of the characteristics of our F8L cavity.

Chapter 5. Numerical study on NLPs and SC generation

In this Chapter some numerical results achieved in the frame of this thesis are presented. In a numerically modeled F8L, more than a thousand of NLPs were obtained; through a few hundreds of these pulses, a complex and very rich dynamics as those reported experimentally was observed, where it was possible to see how sub-packets are expelled from the main bunch, while others interact with sub-pulses rising by the appearance of optical extreme events. Besides, some hundreds of NLPs were propagated in different lengths of SMF via simulations with the intention to generate SC. In Section 5.1, the F8L model is presented whereas in Section 5.2 the two numerical methods used are exposed. Finally, both the NLPs and the SC spectra achieved are presented in Sections 5.3 and 5.4.

5.1 Numerical F8L model

To obtain numerically NLPs, a F8L model with field components in circular base, Real(C^+), Imag(C^+), Real(C^-) and Imag(C^-), was used. The scheme of the F8L model is depicted in Fig. 5.1, and is total length is only about 30 m due to computational time.

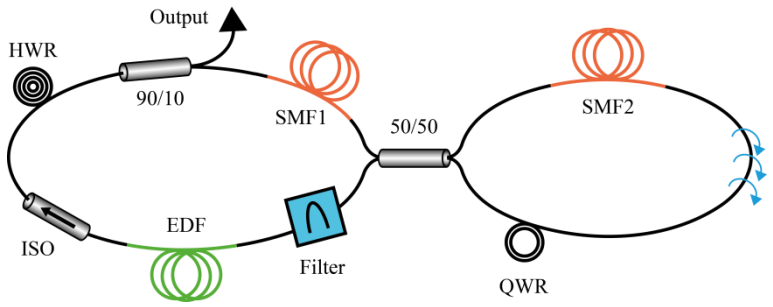

Fig. 5.1. Schematic of the F8L model.

The F8L consists of a ring cavity and a polarization-imbalanced NOLM. In the ring section, a doped fiber (EDF) of 4 m of length (D = –17 ps/nm/km) was defined; this active fiber has gain, considering a uniform small-signal gain g_0 over its entire length, and the gain saturates on pulse energy E_p:

$$g(E_p) = \frac{g_0}{1 + E_p/E_{sat}}. \tag{5.1}$$

At the NOLM input, a dispersive fiber (SMF1, D = 17 ps/nm/km) of 15 m of length was defined, and the polarization was assumed linear (a HWR was used to adjust the polarization angle). For simplicity, the gain dispersion (bounded bandwidth) distributed along the fiber is not considered; instead a lumped filter is assumed at the input of the doped fiber:

$$F(\lambda) = \exp\left[-\left(\frac{\lambda - \lambda_0}{\Delta\lambda_{FWHM}/1.66}\right)^2\right]. \tag{5.2}$$

A 30-nm FWHM bandpass filter takes into account the bandwidth limitation of the DF gain. Finally, the NOLM is formed by 10 m of standard fiber (SMF2, D = 17 ps/nm/km) twisted at a rate of 5 turns per meter, and a QWR whose angle was adjusted for small nonzero low-power NOLM transmission (≈ 0.1). The propagation in each fiber section is calculated by integrating the coupled extended nonlinear Schrödinger equations (NLSEs):

$$\begin{aligned}
\frac{dC^+}{dz} &= -i\frac{\beta_2}{2}\frac{\partial^2 C^+}{\partial t^2} + \frac{2}{3}i\gamma(|C^+|^2 + 2|C^-|^2)C^+ + \frac{g}{2}C^+, \\
\frac{dC^-}{dz} &= -i\frac{\beta_2}{2}\frac{\partial^2 C^-}{\partial t^2} + \frac{2}{3}i\gamma(|C^-|^2 + 2|C^+|^2)C^- + \frac{g}{2}C^-.
\end{aligned} \tag{5.3}$$

In the case of the NOLM loop, integration is carried out in both directions. In both equations the first term is dispersion, the second is Kerr nonlinearities (SPM and XPM) and the third one in gain (for the DF only).

A small-amplitude Gaussian white noise at 1550 nm is used as initial signal at 5 W. Integration is then performed over several cycles, until a steady state is obtained. It has to be noted however that, in the case of NLP operation, strictly speaking no steady state is reached, considering the chaotic nature of these pulses, whose internal structure changes after each round-trip. In this case however, it is considered that a "stable" NLP operation is obtained once the global properties of the NLP remain fairly stable over successive round-trips, and integration is then stopped. The NLPs obtained through the F8L were studied in their dynamics and then were used to simulate SC generation in some pieces of SMF.

5.2 The numerical methods

The two methods used in the present study are presented below. First, the Split-Step Fourier (SSF) method, used to model the laser that produces the NLPs, and then the Fourth-Order Runge–Kutta in the Interaction Picture (RK4IP) method, used to generate SC spectra. To understand the philosophy behind these methods, we consider first the general nonlinear Schrödinger equation (GNLSE) written as

$$\frac{\partial}{\partial z}A(z,T) = -\frac{\alpha}{2}A(z,T) - \left(\sum_{m=2}^{N}\beta_m\frac{i^{m-1}}{m!}\frac{\partial^m}{\partial T^m}\right)A(z,T)$$
$$+ i\gamma\left(1+\frac{i}{\omega_0}\frac{\partial}{\partial T}\right)\left[A(z,T)\left((1-f_R)|A(z,T)|^2 + f_R\int_0^{\infty}h_R(\tau)|A(z,T-\tau)|^2 d\tau\right)\right], \quad (5.4)$$

where $A(z,T)$ is the complex field envelope propagating in the z direction, T is the retarded time for a reference frame travelling a distance L at the envelope group velocity, α is the wavelength-dependent attenuation constant, γ is the nonlinear coefficient of the fiber fundamental mode, β_m are the mth-order dispersion coefficients around the carrier frequency ω_0, and f_R is the Raman effect value

(fractional contribution of $h_R(\tau)$), which has been obtained from the maximum Raman gain [32]. We can observe that Eq. (5.4) is composed of two main sections: the dispersive effects (first line) and the nonlinear effects (second and third lines). In this equation, the delayed Raman response function $h_R(\tau)$ is defined as

$$h_R(\tau) = (f_a + f_c)\, h_a(\tau) + f_b\, h_b(\tau) \tag{5.5}$$

with

$$h_a(\tau) = \frac{\tau_1^2 + \tau_2^2}{\tau_1 \tau_2^2} \exp\left(-\frac{\tau}{\tau_2}\right) \sin\left(\frac{\tau}{\tau_1}\right), \tag{5.6}$$

$$h_b(\tau) = \frac{2\tau_b - \tau}{\tau_b^2} \exp\left(-\frac{\tau}{\tau_b}\right), \tag{5.7}$$

where Eq. (5.6) and (5.7) are the isotropic and anisotropic parts of Eq. (5.5), respectively, with $\tau_1 = 1/\Omega_R$ as the inverse average phonon circular frequency, τ_2 as the damping time of phonons, and f_b as the relative contribution of the boson peak. Particular values for Eqs. (5.4) to (5.7) have been taken from Tables 1 and 2 [96].

Table 1. Raman parameters.

Parameter	Value
τ_1	12.2 fs
τ_2	32 fs
τ_b	96 fs
f_a	0.75
f_b	0.21
f_c	0.04
f_R	0.18

Table 2. Standard fiber parameters.

Parameter	Value
β_2	$-21.68\ \mathrm{ps}^2/\mathrm{km}$
γ	$1.5/\mathrm{W/km}$

In the case of using PCF as the nonlinear medium for SC generation instead of SMF (this is not the case), values of β_m can be calculated numerically for an integer m [23], such as those exemplified in Table 3 [97], by solving the transcendental equation

$$\left[\frac{\mu_1\varepsilon_1\omega}{\gamma}\frac{J_m'(\gamma R)}{J_m(\gamma R)}+\frac{\mu_0\varepsilon_0\omega}{\beta}\frac{K_m'(\beta R)}{K_m(\beta R)}\right]\left[\frac{\omega}{\gamma}\frac{J_m'(\gamma R)}{J_m(\gamma R)}+\frac{\omega}{\beta}\frac{K_m'(\beta R)}{K_m(\beta R)}\right] = \frac{k_z^2 m^2}{R^2}\left(\frac{1}{\gamma^2}+\frac{1}{\beta^2}\right)^2, \tag{5.8}$$

where J_m and K_m are Bessel functions, and J_m' and K_m' are their respective derivatives. A detailed procedure to obtain Eq. (5.8) can be found in [98].

Table 3. Parameters for a PCF.

Parameter	Value
β_2	$-12.76\ \mathrm{ps}^2/\mathrm{km}$
β_3	$8.119\times10^{-2}\ \mathrm{ps}^3/\mathrm{km}$
β_4	$-1.321\times10^{-4}\ \mathrm{ps}^4/\mathrm{km}$
β_5	$3.032\times10^{-7}\ \mathrm{ps}^5/\mathrm{km}$
β_6	$-4.196\times10^{-10}\ \mathrm{ps}^6/\mathrm{km}$
β_7	$2.570\times10^{-13}\ \mathrm{ps}^7/\mathrm{km}$
γ	$45/\mathrm{W/km}$

To be solved the differential equation (5.4) by conventional explicit methods such as the SSF or RK4IP, it must be rewritten as

$$\frac{\partial}{\partial z}A(z,T) = \left(\widehat{D}+\widehat{N}\right)A(z,T), \tag{5.9}$$

where $\widehat{D}$ is a differential operator that accounts for dispersion and losses within a linear medium, and $\widehat{N}$ (non-dispersive term) is a nonlinear operator that governs the effect of fiber nonlinearities on pulse propagation [23]; these operators are given by

$$\widehat{D} = -\frac{\alpha}{2}-\left(\sum_{m=2}^{N}\beta_m\frac{i^{m-1}}{m!}\frac{\partial^m}{\partial T^m}\right), \tag{5.10}$$

$$\widehat{N} = \frac{i\gamma}{A}\left(1+\frac{i}{\omega_0}\frac{\partial}{\partial T}\right)\left[(1-f_R)A|A|^2+f_R\int_0^\infty h_R(\tau)|A(z,T-\tau)|^2 d\tau\right].$$

5.2.1 Split-Step Fourier method

In general, dispersion and nonlinearity act together along the length of the fiber. The SSF method obtains an approximate solution by assuming that in propagating the optical field over a small distance h, the dispersive and nonlinear effects can be assumed to act independently. More specifically, propagation from z to $z + h$ is carried out in two steps. In the first step, the nonlinearity acts alone, and $\widehat{D} = 0$ in Eq. (5.9); and in the second step, dispersion acts alone, and $\widehat{N} = 0$ in the same equation [23]. Mathematically,

$$A(z + h, T) \approx \exp\left(h\widehat{D}\right) \exp\left(h\,\widehat{N}\right) A(z, T). \tag{5.11}$$

The first exponential operator of Eq. (5.11) can be evaluated in the Fourier domain using the prescription

$$\exp\left(h\widehat{D}\right) B(z, T) = \mathcal{F}^{-1} \exp\left[h\widehat{D}(-i\omega)\right]\, \mathcal{F}\, B(z, T), \tag{5.12}$$

where $\mathcal{F}$ denotes the Fourier-transform operation, ω is the circular frequency in the Fourier domain, and $\widehat{D}(-i\omega)$ is obtained from the dispersion operator of Eq. (5.4), by replacing the differential operator by $-i\omega$. The integration of the dispersion terms is performed in the frequency domain where the derivatives become simple multiplications whereas the nonlinear terms are integrated in the time domain. At each integration step, the method alternates between the time and frequency domains.

5.2.2 Fourth-Order Runge–Kutta in the Interaction Picture method

In this method, it is necessary to transform $A(z, T)$ from Eq. (5.11) into an interaction picture representation as follows:

$$A_I = \exp\left((z' - z)\widehat{D}\right) A(z, T). \tag{5.13}$$

Equation (5.13) allows the use of explicit techniques to put the solution forward; then [27], its evolution is given by

$$\frac{\partial}{\partial z}A_I = \exp\left((z'-z)\widehat{D}\right)\widehat{N}\exp\left((z-z')\widehat{D}\right)A_I. \tag{5.14}$$

The RK4IP method has midpoints which allow making half of the exponential transformations in Eq. (5.14). This is achieved with an appropriate choice of z': the separation distance between the interaction and normal pictures, defined as $z' = z + h/2$. As the integration is over the longitudinal step h, we have $h/2 = z' - z$. Therefore, expressing the interaction picture in the normal one, we have $A(z+h,T)$ instead of $A(z,T)$:

$$A_I = \exp\left(\frac{h\widehat{D}}{2}\right)A(z,T) \tag{5.15}$$

with

$$\begin{aligned}
k_1 &= \exp\left(\frac{h\widehat{D}}{2}\right)\left[h\,\widehat{N}\big(A(z,T)\big)\right]A(z,T)\\
k_2 &= h\,\widehat{N}\left(A_I + \frac{k_1}{2}\right)\left[A_I + \frac{k_1}{2}\right]\\
k_3 &= h\,\widehat{N}\left(A_I + \frac{k_2}{2}\right)\left[A_I + \frac{k_2}{2}\right]\\
k_4 &= h\,\widehat{N}\left(\exp\left(\frac{h\widehat{D}}{2}\right)(A_I + k_3)\right)\exp\left(\frac{h\widehat{D}}{2}\right)[A_I + k_3].
\end{aligned} \tag{5.16}$$

And finally, we have

$$A(z+h,T) = \exp\left(\frac{h\widehat{D}}{2}\right)\left[A_I + \frac{k_1}{6} + \frac{k_2}{3} + \frac{k_3}{3}\right] + \frac{k_4}{6}. \tag{5.17}$$

To obtain Eq. (5.17) in the normal picture representation it is necessary to perform four evaluations for each step of the nonlinear operator $\widehat{N}$ and four more of the exponential dispersion operator. This means that eight FFTs are necessary in the process which has four predictions, each refining the previous one.

5.3 Obtainment and study of NLPs

The integration, using the SSF method, was performed over several cycles until convergence is reached. The NLPs duration is limited to 100 ps (0.1 ns) due to computational time. An example of a NLP achieved with the F8L model is shown in Fig. 5.2(a), where we can appreciate the fine inner structure of this complex pulse; the spectrum of this same unique pulse is presented in Fig. 5.2(b), showing a noisy structure (Cfr. Fig. 2.17(a)).

If we see the spectra of experimental NLPs, as those presented in Fig. 3.2(b) and 3.4(b), we will find very smooth curves. This is because in experimental measurements, an OSA always shows averaged spectra. If we consider for example the NLPs obtained experimentally in the present thesis (see Chapter 3) with a period of about 1 μs, it would imply that the OSA is receiving almost a million pulses per second, averaging several of them. For this reason, in this numerical work, more than 1000 NLPs were achieved trying to obtain comparable spectra to those that could be obtained experimentally. As in Fig. 3.5, some waveforms (non-consecutive cycles) are depicted in Fig. 5.3.

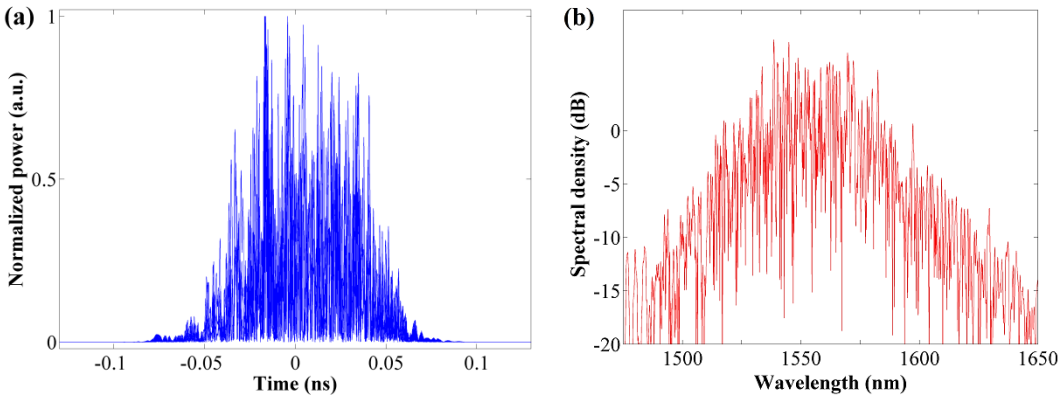

Fig. 5.2. (a) Single NLP obtained numerically; (b) spectrum of this same unique pulse.

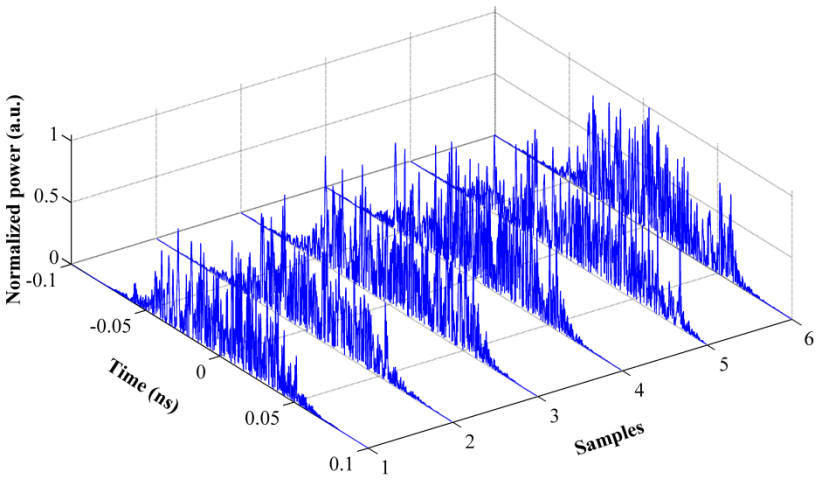

Fig. 5.3. Temporal waveforms of NLPs in non-consecutive cycles obtained numerically with the F8L model.

However, if we observe sequences of dozens of pulses (consecutive cycles), complex dynamics similar to those reported experimentally in [7,53] and even the close relationship that exists with extreme optical events (rogue waves, RW) reported experimentally in [9] are manifested. For example, in a first sequence of 50 cycles of NLPs depicted in Fig. 5.4, it can be seen that the main bunch remains fairly stable while sub-packets are ejected towards longer times. We can even see how one of them is extinguished by cycle 40, labeled "ext" and marked with a yellow circle in Fig. 5.4(b), while other subsequently ejected sub-packets do not vanish before cycle 50 (Fig. 5.4(a) and 5.4(b)).

By knowing that an extreme event is one whose amplitude exceeds 2.2 times the significant wave-height (SWH, average amplitude of the highest third of all events), Fig. 5.4(a) shows some extreme events because there are peaks that exceed that mean highest power (~25 W) even reaching almost three times this value (~65 W), as the extreme event depicted in Fig. 5.4(c), in cycle 10.

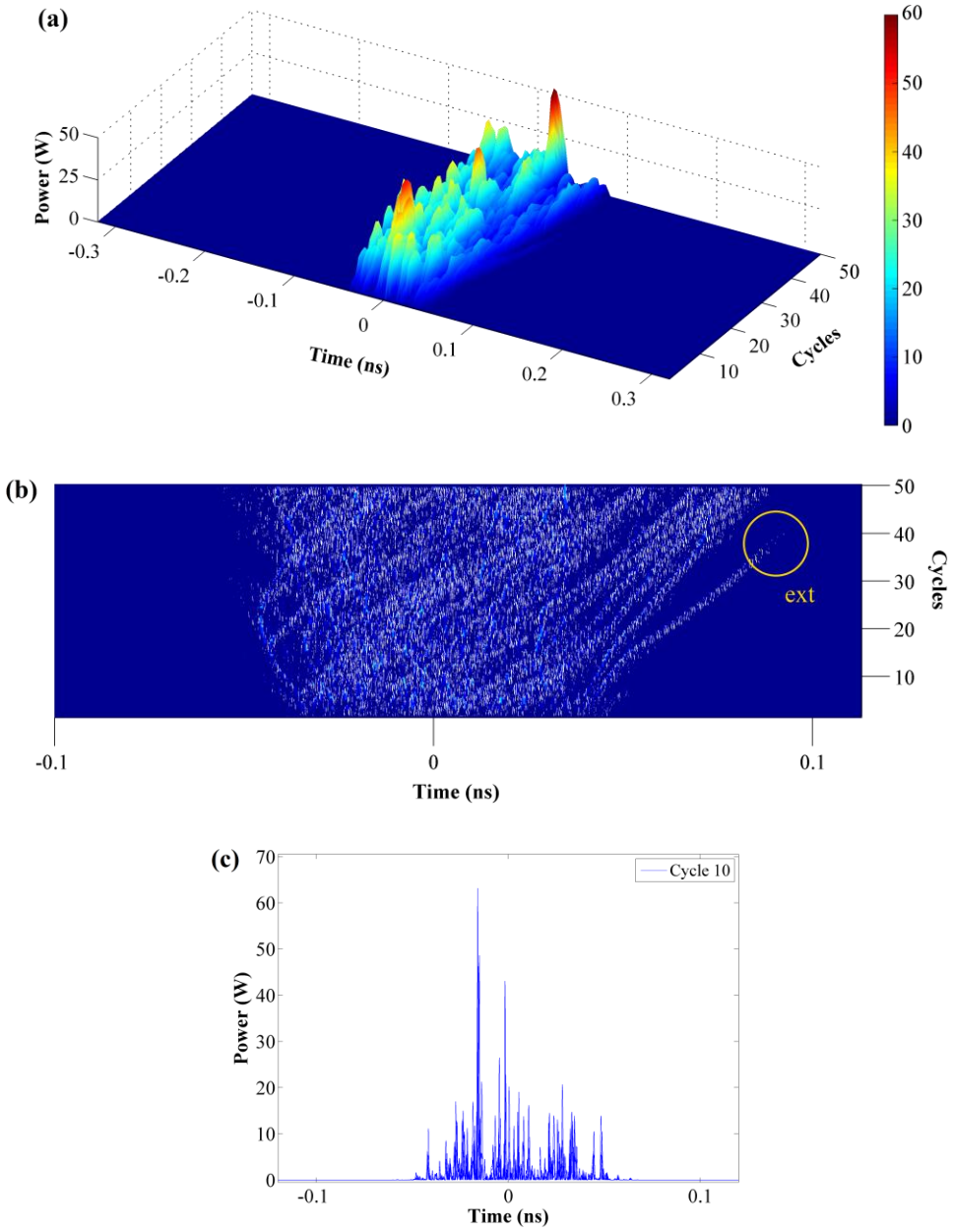

Fig. 5.4. Sequence of 50 consecutive cycles of a NLP from the numerical F8L model: (a) time evolution of a quite stable NLP envelope (with color scale of power, W); (b) top view, showing the detachment of sub-packets on the right and the extinction of one of them close to cycle 40; (c) single waveform of the rising of an extreme event.

In a second sequence of NLPs of little more than 100 cycles, depicted in Fig. 5.5(a), several sub-packets are expelled at longer times with very well-defined trajectories. It can be seen in Fig. 5.5(b) how one sub-packet (labeled "sp1") detached after cycle 53 collides with another sub-packet (labeled "sp2") of different sub-pulses very possibly formed by the rising of an extreme event in cycle 53, shown in Fig. 5.5(d). After this collision, sp1 and sp2 are extinguished but a third sub-packet (labeled "sp3") rises from the background radiation after a couple of cycles. In Fig. 5.5(b) this extreme event is marked with a dotted red circle, the trajectories of sp1 and sp2 with green and white arrows respectively, and the sp1-sp2 collision in a continuous yellow circle; Fig. 5.5(c) is a close-up view of Fig. 5.5(b), showing that sp2 travels at a speed higher than sp1 and the first three packets detached, so we demonstrated that there are sub-packets that move faster than others in a NLP internal dynamic. This can also be seen in the inset of Fig. 5.5(a). On the other hand, to the left of the main bunch, a C-shaped protruding trajectory can be observed in Fig. 5.5(b): this sub-packet, once expelled from the main bunch near cycle 60, drives away until completely stopped and then returns near cycle 90; even more examples of this type of dynamics can be noticed throughout the sequence, but within the main packet. Similar dynamics were also reported experimentally in [7,53].

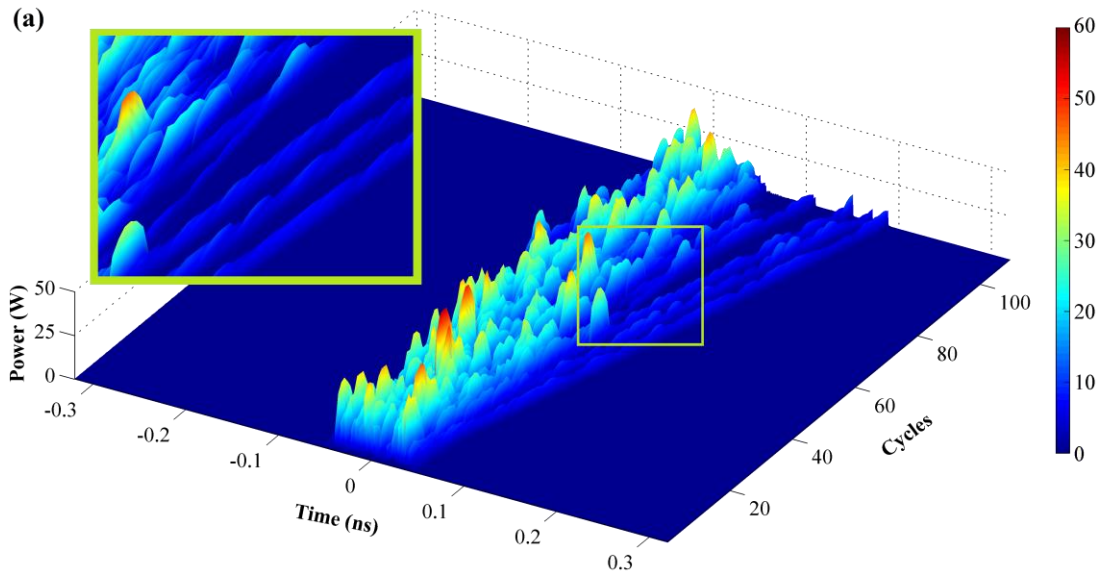

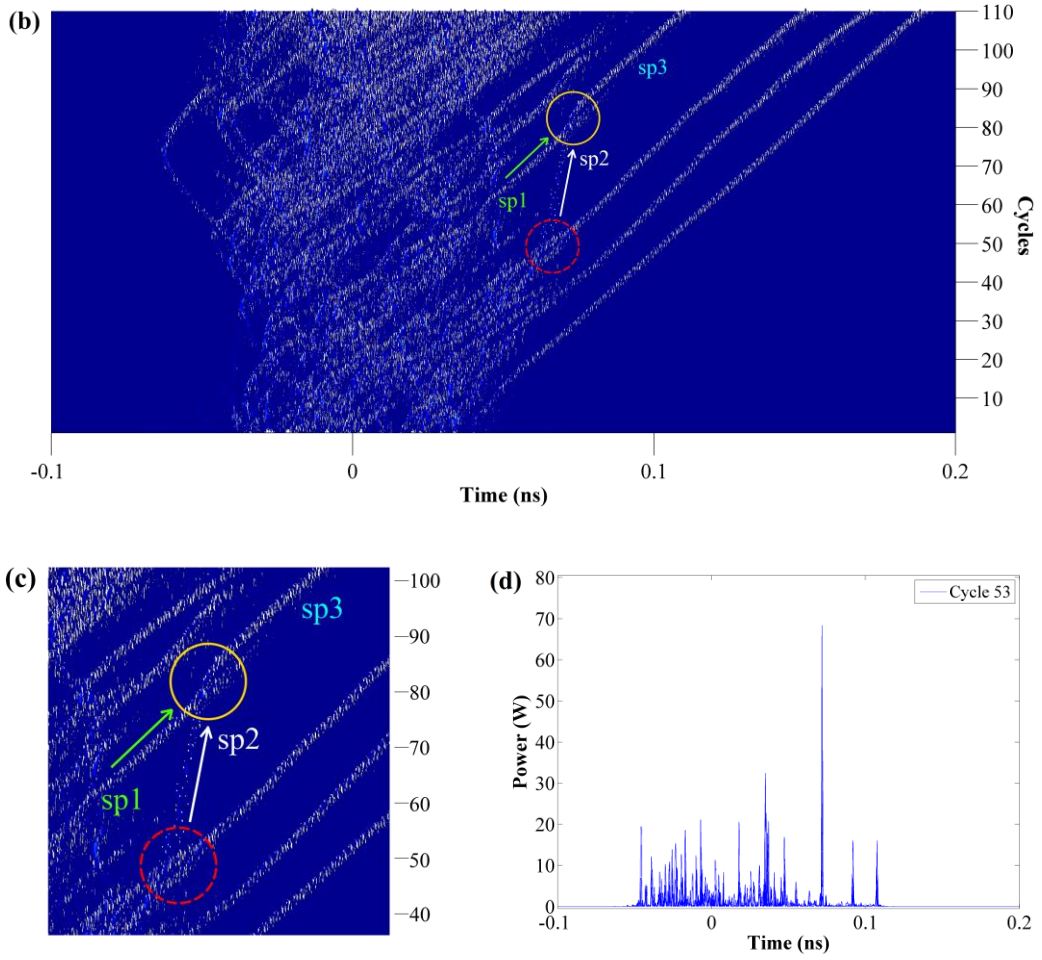

Fig. 5.5. Second sequence of NLPs (110 consecutive cycles): (a) detachment of some sub-packets at right traveling at the same speed (inset: close-up view of an extreme event whose produced sub-pulses collide with a sub-packet at different speeds); (b) top view, showing the extreme event, the collision and the sub-packets involved; (c) close-up view of (b) around this extreme event; (d) single waveform of the extreme event in question.

5.4 Supercontinuum generation using NLPs

Although the F8L model yields results in terms of real and imaginary part of C^+ and C^-, only the right circular polarization states is taken into account for the SC generation simulation: $\mathrm{Real}(C^+) + i \cdot \mathrm{Imag}(C^+)$.

To obtain SC spectra using the RK4IP method, NLPs were propagated in different pieces of standard fiber (D = 17 ps/nm/km). As the NLPs obtained by the model described in Section 5.1 have an average peak power of ~20 W at the output, they were amplified to about 100 W to match these results with the experimental ones described in Section 3.1, since the configurations of these F8Ls are made mainly of standard telecom elements, despite the size of the cavities and the duration of the pulses. In order to ensure that the spectra did not expand indefinitely, and to take into account the large fiber attenuation far away from the 1550-nm region, a simple attenuation function was defined with parabolic shape; the attenuation function α is shown in Fig. 5.6:

$$\alpha = \begin{cases} 10^{\frac{(\lambda - 1305\ \mathrm{nm})^2}{3\times10^5}} - 0.65, & \lambda < 1402 \\ 10^{\frac{(\lambda - 1550\ \mathrm{nm})^2}{2.4\times10^5}} - 0.81, & \lambda \geq 1402. \end{cases} \tag{5.18}$$

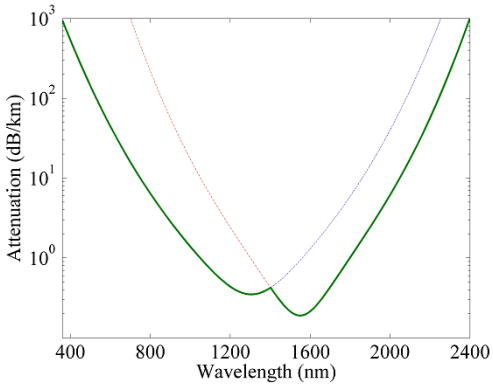

Fig. 5.6. Attenuation function defined in Eq. (5.18) for the SC generation simulation.

However, a factor of 4.34 in α was used because there are two attenuation functions: one in terms of dB (in the computational code) and the other in arbitrary units (a.u.):

$$\alpha_{dB} = \frac{10}{L}\log\frac{P_{in}}{P_{out}} \qquad \text{and} \qquad \alpha = \frac{1}{L}\ln\frac{P_{in}}{P_{out}}, \tag{5.19}$$

where P_{in} and P_{out} are the input and output powers, and L is the length of the fiber. By some algebra, we can write α_{dB} in terms of α from Eq. (5.19), Then, we have

$$\alpha_{dB} = 4.34\ \alpha. \tag{5.20}$$

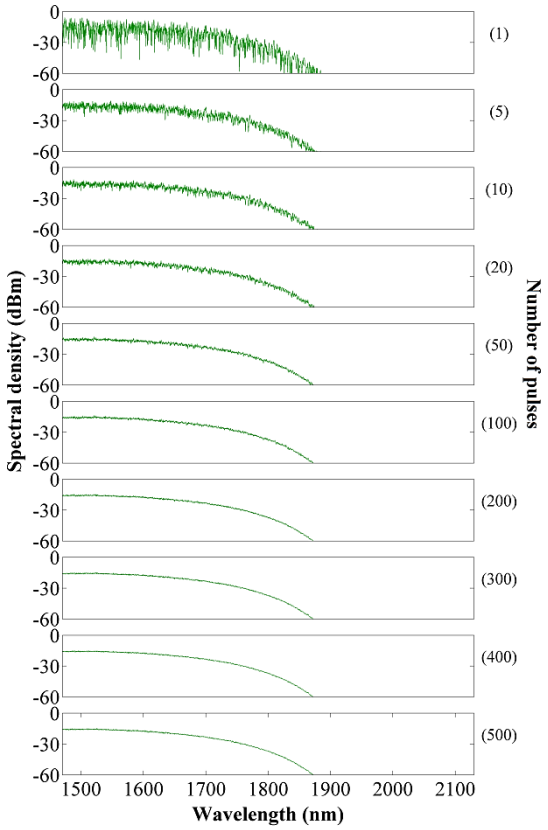

Fig. 5.7. Comparison of averaged spectra based on the number of pulses (1 to 500 NLPs) for the 1000-m-SMF case.

Now, according to Section 4.1, four lengths of SMF fiber were defined as nonlinear medium: 100 m, 300 m, 600 m and 1000 m. Once SC spectra were obtained for one NLP, 500 NLPs were propagated in a piece of SMF averaging their spectra to obtain smooth curves, similar to those measured experimentally. It was observed that curves are fairly smooth starting from 100 NLPs, and for more than 200 pulses the curves show minimal improvements in terms of smoothness, as it can be seen in Fig. 5.7.

In Fig. 5.8, the spectra for different lengths of SMF are compared taking the average of 200 NLPs, a number of pulses that we consider acceptable enough. According to the results shown in Fig. 4.2, the spectrum extends to longer wavelengths if length increases from 100 m to 300 m. In the numerical work, for as much as 300 m, the maximum spectral extension is practically reached and only flatness is improved for 600 m and 1000 m. These preliminary numerical results are consistent with the experimental results presented in the first part of Section 4.1.

Otherwise, for even much longer SMF lengths from 1 to 3 km, as shown in Fig. 5.9, the spectrum suffers more erosion due to attenuation and it is shortened some few of nm, which is consistent as well with the results of the aforementioned Section 4.1.

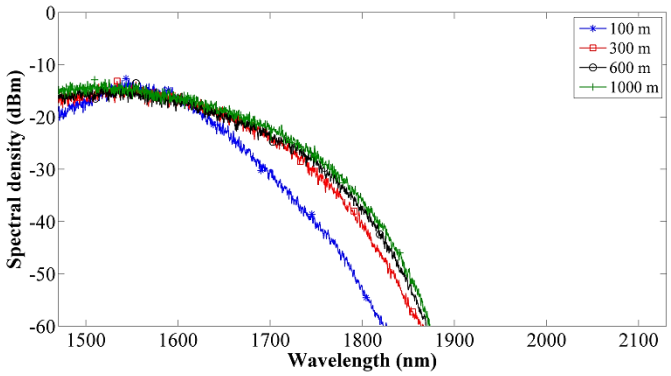

Fig. 5.8. SC spectra at the output of the nonlinear element consisting of SMF.

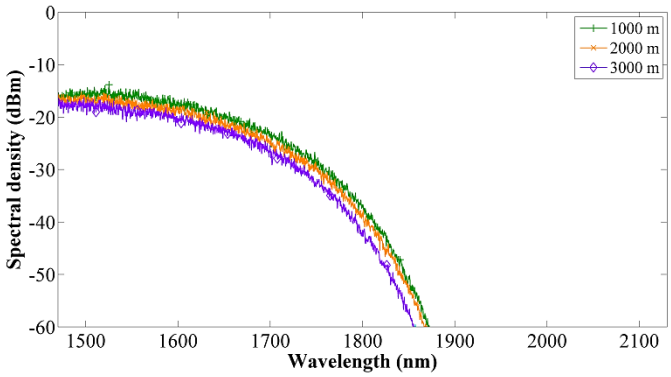

Fig. 5.9. Comparison of spectra for three SMF long lengths.

Although it is necessary to further improve the numerical work on SC generation, in particular to identify clearly the nonlinear phenomena involved in the formation of these spectra, these preliminary results present an acceptable behavior, at the light of the experimental results.

Final Remarks

In this thesis we report the experimental study on the production of NLPs in two all-fiber F8Ls and their use for SC generation in SMF and HNLF (1550-nm zero-dispersion wavelength). By the appropriate polarization settings in both laser cavities, fairly stable regimes of NLPs were established; in this way, they allowed obtaining wide and very flattened spectra through optical fibers that are not optimized for this purpose like the SMF.

In a first cavity, a conventional erbium F8L, NLPs were obtained and then were amplified and launched in an external nonlinear medium made of different sections of fiber, generating spectra extending over more than 300 nm using SMF only, and reaching almost 1000 nm by adding a piece of HNLF, using low pump power (25–35 mW); besides, these spectra present an excellent dynamic range of about 60 dB. Our numerical simulations confirmed our experimental demonstrations: the best spectral widening, optimizing the standard fiber length is given for about 300 m; shorter lengths of SMF do not extend enough the spectrum of NLPs and longer lengths erode the spectral extension near the 2-μm region due to the strong absorption of silica.

On the other hand, in an Er/Yb double-clad F8L, we obtained NLPs with energy per pulse as high as 300 nJ where the absence of a polarizing element increased the degrees of freedom in the nonlinear evolution of the intracavity radiation. This is assumed to help avoiding the splitting of the pulses as the pumping power is increased, and to allow the generation of SC spectra of more than 200 nm directly at the laser output (limited by the range of the available OSA). In addition, by increasing the HML order and extending the length of the SMF in the ring section of the F8L, a spectrum over 160 nm of less than 3 dB of flatness was obtained. Finally, an extended SC spectrum of more than 450 nm was achieved in the fundamental

mode locking regime, launching the high-energy NLPs into a 100-m-long HNLF at the laser output without external amplifier.

In a numerical F8L model more than 1000 NLPs were produced. Analyzing some dozens of consecutive cycles we could observe complex dynamics such as those we have already reported experimentally: extinction of sub-packets, production of sub-pulses from extreme events, and collision of sub-packets with different speeds inside the main bunch. On the other hand, the other hundreds of NLPs were propagated numerically in sections of different lengths of standard fiber to generate SC, which confirmed our experimental results as mentioned above.

As future work, we will continue with the experimental study on the generation of high-energy NLPs and their applications. Among these will be SC generation (with possible applications to OCT and optical device testing) and micro-drilling or micro-marking. Besides, we shall work on the possible correlation between some dynamics of NLPs and the biological responses of some organisms. On the other hand, the numerical work will be followed up: the production and study of NLPs and their very rich dynamics and otherwise, a deeper study on SC generation in different kinds of fibers.

References

[1] M. Horowitz, Y. Barad and Y. Silberberg, "Noiselike pulses with a broadband spectrum generated from an erbium-doped fiber laser", *Opt. Lett.* **22**, 799 (1997).

[2] X.W. Zheng, Z.C. Luo, H. Liu, N. Zhao, Q.Y. Ning, M. Liu, X.H. Feng, X.B. Xing, A.P. Luo and W.C. Xu, "High-energy noiselike rectangular pulse in a passively mode-locked figure-eight fiber laser", *Appl. Phys. Express* **7**, 42701 (2014).

[3] J. Li, Z. Zhang, Z. Sun, H. Luo, Y. Liu, Z. Yan, C. Mou, L. Zhang and S.K. Turitsyn, "All-fiber passively mode-locked Tm-doped NOLM-based oscillator operating at 2-μm in both soliton and noisy-pulse regimes", *Opt. Express* **22**, 7875 (2014).

[4] J.P. Lauterio-Cruz, J.C. Hernandez-Garcia, O. Pottiez, J.M. Estudillo-Ayala, E.A. Kuzin, R. Rojas-Laguna, H. Santiago-Hernandez and D. Jauregui-Vazquez, "High energy noise-like pulsing in a double-clad Er/Yb figure-of-eight fiber laser", *Opt. Express* **24**, 13778 (2016).

[5] Y. Jeong, L.A. Vazquez-Zuniga, S. Lee and Y. Kwon, "On the formation of noise-like pulses in fiber ring cavity configurations", *Opt. Fiber Technol.* **20**, 575–592 (2014).

[6] H. Santiago-Hernandez, O. Pottiez, M. Duran-Sanchez, R.I. Alvarez-Tamayo, J.P. Lauterio-Cruz, J.C. Hernandez-Garcia, B. Ibarra-Escamilla and E.A. Kuzin, "Dynamics of noise-like pulsing at sub-ns scale in a passively mode-locked fiber laser", *Opt. Express* **23**, 18840 (2015).

[7] E. Garcia-Sanchez, O. Pottiez, Y. Bracamontes-Rodriguez, J.P. Lauterio-Cruz, H.E. Ibarra-Villalon, J.C. Hernandez-Garcia, M. Bello-Jimenez and E.A. Kuzin, "Complex dynamics of a fiber laser in non-stationary pulsed operation", *Opt. Express* **24**, 18917 (2016).

[8] C. Lecaplain and P. Grelu, "Rogue waves among noiselike-pulse laser emission: An experimental investigation", *Phys. Rev. A* **90**, 13805 (2014).

[9] O. Pottiez, H.E. Ibarra-Villalon, Y.E. Bracamontes-Rodríguez, J.A. Minguela-Gallardo, E. García-Sanchez, J.P. Lauterio-Cruz, J.C. Hernandez-Garcia, M. Bello-Jimenez and E.A. Kuzin, "Soliton formation from a noise-like pulse during extreme events in a fibre ring laser", *Laser Phys. Lett.* **14**, 105101 (2017).

[10] S. Keren and M. Horowitz, "Interrogation of fiber gratings by use of low-coherence spectral interferometry of noiselike pulses", *Opt. Lett.* **26**, 328 (2001).

[11] K. Özgören, B. Öktem, S. Yilmaz, F.Ö. Ilday and K. Eken, "83 W, 31 MHz, square-shaped, 1 ns-pulsed all-fiber-integrated laser for micromachining", *Opt. Express* **19**, 17647 (2011).

[12] V. Goloborodko, S. Keren, A. Rosenthal, B. Levit and M. Horowitz, "Measuring temperature profiles in high-power optical fiber components", *Appl. Opt.* **42**, 2284 (2003).

[13] Y.J. You, C. Wang, Y.L. Lin, A. Zaytsev, P. Xue and C.L. Pan, "Ultrahigh-resolution optical coherence tomography at 1.3 μm central wavelength by using a supercontinuum source pumped by noise-like pulses", *Laser Phys. Lett.* **13**, 25101 (2016).

[14] L.A. Vazquez-Zuniga and Y. Jeong, "Super-Broadband Noise-Like Pulse Erbium-Doped Fiber Ring Laser With a Highly Nonlinear Fiber for Raman Gain Enhancement", *IEEE Photonics Technol. Lett.* **24**, 1549–1551 (2012).

[15] J.C. Hernandez-Garcia, O. Pottiez and J.M. Estudillo-Ayala, "Supercontinuum generation in a standard fiber pumped by noise-like pulses from a figure-eight fiber laser", *Laser Phys.* **22**, 221–226 (2012).

[16] A. Zaytsev, C.H. Lin, Y.J. You, C.C. Chung, C.L. Wang and C.L. Pan, "Supercontinuum generation by noise-like pulses transmitted through normally dispersive standard single-mode fibers", *Opt. Express* **21**, 16056 (2013).

[17] J.P. Lauterio-Cruz, O. Pottiez, Y.E. Bracamontes-Rodríguez, J.C. Hernández-García, E. García-Sánchez, M. Bello-Jimenez and E.A. Kuzin, "Comparative study of supercontinuum generation using standard and high-nonlinearity fibres pumped by noise-like pulses", *Laser Phys.* **27**, 65107 (2017).

[18] R.R. Alfano and S.L. Shapiro, "Emission in the Region 4000 to 7000 Å Via Four-Photon Coupling in Glass", *Phys. Rev. Lett.* **24**, 584–587 (1970).

[19] J.M. Dudley, G. Genty and S. Coen, "Supercontinuum generation in photonic crystal fiber", *Rev. Mod. Phys.* **78**, 1135–1184 (2006).

[20] M. Kumar, C. Xia, X. Ma, V.V Alexander, M.N. Islam, F.L. Terry, C.C. Aleksoff, A. Klooster and D. Davidson, "Power adjustable visible super-continuum generation using amplified nanosecond gains-witched laser diode", *Opt. Express* **16**, 6194 (2008).

[21] J. Hult, "A Fourth-Order Runge–Kutta in the Interaction Picture Method for Simulating Supercontinuum Generation in Optical Fibers", *J. Light. Technol.* **25**, 3770–3775 (2007).

[22] A.A. Rieznik, A.M. Heidt, P.G. Konig, V.A. Bettachini and D.F. Grosz, "Optimum Integration Procedures for Supercontinuum Simulation", *IEEE Photonics J.* **4**, 552–560 (2012).

[23] G.P. Agrawal, *Nonlinear Fiber Optics*, 5th ed. (Academic Press, 2012).

[24] K.J. Blow and D. Wood, "Theoretical description of transient stimulated Raman scattering in optical fibers", *IEEE J. Quantum Electron.* **25**, 2665–2673 (1989).

[25] Z. Zhang, L. Chen and X. Bao, "A fourth-order Runge–Kutta in the interaction picture method for numerically solving the coupled nonlinear Schrödinger equation", *Opt. Express* **18**, 8261 (2010).

[26] S. Balac, A. Fernandez, F. Mahé, F. Méhats and R. Texier-Picard, "The Interaction Picture method for solving the generalized nonlinear Schrödinger equation in optics", *ESAIM Math. Model. Numer. Anal.* **50**, 945–964 (2016).

[27] B.M. Caradoc-Davies, *(Ph.D. Thesis) Vortex Dynamics in Bose-Einstein Condensates* (University of Otago, New Zealand, 2000).

[28] R.H. Stolen and A. Ashkin, "Optical Kerr effect in glass waveguide", *Appl. Phys. Lett.* **22**, 294 (1973).

[29] R.H. Stolen and C. Lin, "Self-phase-modulation in silica optical fibers", *Phys. Rev. A* **17**, 1448–1453 (1978).

[30] M.N. Islam, J.R. Simpson, H.T. Shang, L.F. Mollenauer and R.H. Stolen, "Cross-phase modulation in optical fibers", *Opt. Lett.* **12**, 625 (1987).

[31] K. Tai, A. Hasegawa and A. Tomita, "Observation of modulational instability in optical fibers", *Phys. Rev. Lett.* **56**, 135–138 (1986).

[32] R.H. Stolen, W.J. Tomlinson, H.A. Haus and J.P. Gordon, "Raman response function of silica-core fibers", *J. Opt. Soc. Am. B* **6**, 1159 (1989).

[33] D. Mahgerefteh, D.L. Butler, J. Goldhar, B. Rosenberg and G.L. Burdge, "Technique for measurement of the Raman gain coefficient in optical fibers.", *Opt. Lett.* **21**, 2026–8 (1996).

[34] J.G. Rarity, J. Fulconis, J. Duligall, W.J. Wadsworth and P.St.J. Russell, "Photonic crystal fiber source of correlated photon pairs", *Opt. Express* **13**, 534–544 (2005).

[35] N.J. Zabusky and M.D. Kruskal, "Interaction of "Solitons" in a Collisionless Plasma and the Recurrence of Initial States", *Phys. Rev. Lett.* **15**, 240–243 (1965).

[36] A. Hasegawa and F. Tappert, "Transmission of Stationary Nonlinear Optical Pulses in Dispersive Dielectric Fibers.1. Anomalous Dispersion", *Appl. Phys. Lett.* **23**, 142–144 (1973).

[37] K. Tamura, E.P. Ippen, H.A. Haus and L.E. Nelson, "77-fs pulse generation from a stretched-pulse mode-locked all-fiber ring laser", *Opt. Lett.* **18**, 1080 (1993).

[38] P. Grelu and N. Akhmediev, "Dissipative solitons for mode-locked lasers", *Nat. Photonics* **6**, 84–92 (2012).

[39] A. Chong, W.H. Renninger and F.W. Wise, "All-normal-dispersion femto-second fiber laser with pulse energy above 20nJ", *Opt. Lett.* **32**, 2408 (2007).

[40] F.W. Wise, A. Chong and W.H. Renninger, "High-energy femtosecond fiber lasers based on pulse propagation at normal dispersion", *Laser Photonics Rev.* **2**, 58–73 (2008).

[41] V. Lazarev, A. Krylov, D. Dvoretskiy, S. Sazonkin, A. Pnev, S. Leonov, D. Shelestov, M. Tarabrin, V. Karasik, A. Kireev and M. Gubin, "Stable Similariton Generation in an All-Fiber Hybrid Mode-Locked Ring Laser for Frequency Metrology", *IEEE Trans. Ultrason. Ferroelectr. Freq. Control* **63**, 1028–1033 (2016).

[42] F.Ö. Ilday, J.R. Buckley, W.G. Clark and F.W. Wise, "Self-Similar Evolution of Parabolic Pulses in a Laser", *Phys. Rev. Lett.* **92**, 213902 (2004).

[43] O. Prochnow, A. Ruehl, M. Schultz, D. Wandt and D. Kracht, "All-fiber similariton laser at 1 mum without dispersion compensation.", *Opt. Express* **15**, 6889–6893 (2007).

[44] K. Krzempek and K. Abramski, "6.5 μJ pulses from a compact dissipative soliton resonance mode-locked erbium–ytterbium double clad (DC) laser", *Laser Phys. Lett.* **14**, 15101 (2017).

[45] K. Krzempek, J. Sotor and K. Abramski, "Compact all-fiber figure-9 dissipative soliton resonance mode-locked double-clad Er:Yb laser", *Opt. Lett.* **41**, 4995 (2016).

[46] Z.C. Luo, W.J. Cao, Z.B. Lin, Z.R. Cai, A.P. Luo and W.C. Xu, "Pulse dynamics of dissipative soliton resonance with large duration-tuning range in a fiber ring laser", *Opt. Lett.* **37**, 4777 (2012).

[47] D.Y. Tang, L.M. Zhao and B. Zhao, "Soliton collapse and bunched noise-like pulse generation in a passively mode-locked fiber ring laser", *Opt. Express* **13**, 2289 (2005).

[48] L.M. Zhao and D.Y. Tang, "Generation of 15-nJ bunched noise-like pulses with 93-nm bandwidth in an erbium-doped fiber ring laser", *Appl. Phys. B* **83**, 553–557 (2006).

[49] H. Xia, H. Li, G. Deng, J. Li, S. Zhang and Y. Liu, "Compact noise-like pulse fiber laser and its application for supercontinuum generation in highly nonlinear fiber", *Appl. Opt.* **54**, 9379 (2015).

[50] J.U. Kang, "Broadband quasi-stationary pulses in mode-locked fiber ring laser", *Opt. Commun.* **182**, 433–436 (2000).

[51] M. Horowitz and Y. Silberberg, "Control of noiselike pulse generation in erbium-doped fiber lasers", *IEEE Photonics Technol Lett.* **10**, 1389–91 (1998).

[52] L.M. Zhao, D.Y. Tang, J. Wu, X.Q. Fu and S.C. Wen, "Noise-like pulse in a gain-guided soliton fiber laser", *Opt. Express* **15**, 2145 (2007).

[53] E. Garcia-Sanchez, O. Pottiez, Y.E. Bracamontes-Rodriguez, J.P. Lauterio-Cruz, H.E. Ibarra-Villalon, J.C. Hernandez-Garcia, M. Bello-Jimenez and E.A. Kuzin, "A temporal insight into the rich dynamics of a figure-eight fibre laser in the noise-like pulsing regime", *Laser Phys. Lett.* **13**, 105106 (2016).

[54] O. Pottiez, J.C. Hernández-García, B. Ibarra-Escamilla, E.A. Kuzin, M. Durán-Sánchez and A. González-García, "High-order harmonic noise-like pulsing of a passively mode-locked double-clad Er/Yb fibre ring laser", *Laser Phys.* **24**, 115103 (2014).

[55] J.C. Hernandez-Garcia, J.M. Estudillo-Ayala, O. Pottiez, J.D. Filoteo-Razo, J.P. Lauterio-Cruz, J.M. Sierra-Hernandez and R. Rojas-Laguna, "Flat super-continuum generation by a F8L in high-energy harmonic noise-like pulsing regime", *Laser Phys. Lett.* **13**, 125104 (2016).

[56] Y.Q. Huang, Z.A. Hu, H. Cui, Z.C. Luo, A.P. Luo and W.C. Xu, "Coexistence of harmonic soliton molecules and rectangular noise-like pulses in a figure-eight fiber laser", *Opt. Lett.* **41**, 4056 (2016).

[57] Y.E. Bracamontes-Rodríguez, O. Pottiez, E. García-Sánchez, J.P. Lauterio-Cruz, H.E. Ibarra-Villalón, J.C. Hernandez-Garcia, M. Bello-Jimenez, G. Beltrán-Pérez, B. Ibarra-Escamilla and E.A. Kuzin, "Dual noise-like pulse and soliton operation of a fiber ring cavity", *J. Opt.* **19**, 35502 (2017).

[58] A.F.J. Runge, C. Aguergaray, N.G.R. Broderick and M. Erkintalo, "Raman rogue waves in a partially mode-locked fiber laser", *Opt. Lett.* **39**, 319 (2014).

[59] O. Pottiez, R. Paez-Aguirre, J.L. Cruz, M.V. Andrés and E.A. Kuzin, "Statistical characterization of the internal structure of noiselike pulses using a nonlinear optical loop mirror", *Opt. Commun.* **377**, 41–51 (2016).

[60] S.V. Smirnov, S.M. Kobtsev and S.V. Kukarin, "Efficiency of non-linear frequency conversion of double-scale pico-femtosecond pulses of passively mode-locked fiber laser", *Opt. Express* **22**, 1058 (2014).

[61] W.S. Man, H.Y. Tam, M.S. Demokan, P.K.A. Wai and D.Y. Tang, "Mechanism of intrinsic wavelength tuning and sideband asymmetry in a passively mode-locked soliton fiber ring laser", *J. Opt. Soc. Am. B* **17**, 28 (2000).

[62] V. Vali and R.W. Shorthill, "Fiber Laser Gyroscopes", *Proc. Soc. Photo-Opt. Instrum. Eng.* **110**, 77 (1976).

[63] R.A. Bergh, H.C. Lefevre and H.J. Shaw, "All-single-mode fiber-optic gyroscope", *Opt. Lett.* **6**, 198 (1981).

[64] N.J. Doran and D. Wood, "Nonlinear-optical loop mirror", *Opt. Lett.* **13**, 56 (1988).

[65] E.A. Kuzin, N. Korneev, J.W. Haus and B. Ibarra-Escamilla, "Polarization independent nonlinear fiber sagnac inteferometer", *Opt. Commun.* **183**, 389–393 (2000).

[66] M.E. Fermann, F. Haberl, M. Hofer and H. Hochreiter, "Nonlinear amplifying loop mirror", *Opt. Lett.* **15**, 752 (1990).

[67] K. Sponsel, K. Cvecek, C. Stephan, G. Onishchukov, B. Schmauss and G. Leuchs, "Optimization of a Nonlinear Amplifying Loop Mirror for Amplitude Regeneration in Phase-Shift-Keyed Transmission", *IEEE Photonics Technol. Lett.* **19**, 1858–1860 (2007).

[68] I.N. Duling, "All-fiber ring soliton laser mode locked with a nonlinear mirror", *Opt. Lett.* **16**, 539 (1991).

[69] O. Pottiez, E.A. Kuzin, B. Ibarra-Escamilla and F. Méndez-Martínez, "Theoretical investigation of the NOLM with highly twisted fibre and a λ/4 birefringence bias", *Opt. Commun.* **254**, 152–167 (2005).

[70] R. Grajales-Coutiño, B. Ibarra-Escamilla, E.A. Kuzin, J. Gutiérrez-Gutiérrez, O. Pottiez and P. Zaca-Morán, "Láser de fibra de amarre de modos de figura ocho basado en un espejo de lazo óptico no lineal simétrico", *Rev. Mex. Fis.* **53**, 380–385 (2007).

[71] E.A. Kuzin, N. Korneev, J.W. Haus and B. Ibarra-Escamilla, "Theory of nonlinear loop mirrors with twisted low-birefringence fiber", *J. Opt. Soc. Am. B* **18**, 919 (2001).

[72] T. Tanemura and K. Kikuchi, "Circular-Birefringence Fiber for Nonlinear Optical Signal Processing", *J. Light. Technol.* **24**, 4108–4119 (2006).

[73] S.F. Feldman, D.A. Weinberger and H.G. Winful, "Polarization instability in a twisted birefringent optical fiber", *J. Opt. Soc. Am. B* **10**, 1191 (1993).

[74] E.A. Kuzin, S. Mendoza-Vazquez, J. Gutierrez-Gutierrez, B. Ibarra-Escamilla, J.W. Haus and R. Rojas-Laguna, "Intra-pulse Raman frequency shift versus conventional Stokes generation of diode laser pulses in optical fibers", *Opt. Express* **13**, 3388 (2005).

[75] G. Genty, S. Coen and J.M. Dudley, "Fiber supercontinuum sources (Invited)", *J. Opt. Soc. Am. B* **24**, 1771 (2007).

[76] C.F. Kaminski, R.S. Watt, A.D. Elder, J.H. Frank and J. Hult, "Super-continuum radiation for applications in chemical sensing and microscopy", *Appl. Phys. B* **92**, 367–378 (2008).

[77] S.V. Smirnov, J.D. Ania-Castañón, S. Kobtsev and S.K. Turitsyn, *The Super-continuum Laser Source: The Ultimate White Light 3th ed.* Ch. 10, R.R. Alfano, Ed. (Springer New York, 2016), 371–403.

[78] M. Yamanaka, H. Kawagoe and N. Nishizawa, "High-power supercontinuum generation using high-repetition-rate ultrashort-pulse fiber laser for ultrahigh-resolution optical coherence tomography in 1600 nm spectral band", *Appl. Phys. Express* **9**, 22701 (2016).

[79] A.V. Avdokhin, S.V. Popov and J.R. Taylor, "Continuous-wave, high-power, Raman continuum generation in holey fibers", *Opt. Lett.* **28**, 1353 (2003).

[80] J.C. Travers, A.B. Rulkov, B.A. Cumberland, S.V. Popov and J.R. Taylor, "Visible supercontinuum generation in photonic crystal fibers with a 400W continuous wave fiber laser", *Opt. Express* **16**, 14435 (2008).

[81] J.K. Ranka, R.S. Windeler and A.J. Stentz, "Visible continuum generation in air–silica microstructure optical fibers with anomalous dispersion at 800 nm", *Opt. Lett.* **25**, 25 (2000).

[82] T.A. Birks, W.J. Wadsworth and P.St.J. Russell, "Supercontinuum generation in tapered fibers", *Opt. Lett.* **25**, 1415 (2000).

[83] A.M. Zheltikov, "Let there be white light: supercontinuum generation by ultrashort laser pulses", *Phys. Usp.* **49**, 605 (2006).

[84] S.V. Chernikov, Y. Zhu, J.R. Taylor and V.P. Gapontsev, "Supercontinuum self-Q-switched ytterbium fiber laser", *Opt. Lett.* **22**, 298 (1997).

[85] C. Xia, M. Kumar, M.Y. Cheng, O.P. Kulkarni, M.N. Islam, A. Galvanauskas, F.L. Terry, M.J. Freeman, D.A. Nolan and W.A. Wood, "Supercontinuum Generation in Silica Fibers by Amplified Nanosecond Laser Diode Pulses", *IEEE J. Sel. Top. Quantum Electron.* **13**, 789–797 (2007).

[86] C.R. Petersen, P.M. Moselund, C. Petersen, U. Møller and O. Bang, "Spectral-temporal composition matters when cascading supercontinua into the mid-infrared", *Opt. Express* **24**, 749 (2016).

[87] Y. Takushima, K. Yasunaka, Y. Ozeki and K. Kikuchi, "87 nm bandwidth noise-like pulse generation from erbium-doped fibre laser", *Electron. Lett.* **41**, 399 (2005).

[88] S.S. Lin, S.K. Hwang and J.M. Liu, "Supercontinuum generation in highly nonlinear fibers using amplified noise-like optical pulses", *Opt. Express* **22**, 4152–4160 (2014).

[89] T. North and M. Rochette, "Raman-induced noiselike pulses in a highly nonlinear and dispersive all-fiber ring laser", *Opt. Lett.* **38**, 890 (2013).

[90] O. Pottiez, R. Grajales-Coutiño, B. Ibarra-Escamilla, E.A. Kuzin and J.C. Hernández-García, "Adjustable noiselike pulses from a figure-eight fiber laser", *Appl. Opt.* **50**, E24 (2011).

[91] H. Santiago-Hernandez, O. Pottiez, R. Paez-Aguirre, H.E. Ibarra-Villalon, A. Tenorio-Torres, M. Duran-Sanchez, B. Ibarra-Escamilla, E.A. Kuzin and J.C. Hernandez-Garcia, "Generation and characterization of erbium-Raman noise-like pulses from a figure-eight fibre laser", *Laser Phys.* **25**, 45106 (2015).

[92] B. Ibarra-Escamilla, O. Pottiez, E.A. Kuzin, J.W. Haus, R. Grajales-Coutiño and P. Zaca-Moran, "Experimental investigation of self-starting operation in a F8L based on a symmetrical NOLM", *Opt. Commun.* **281**, 1226–1232 (2008).

[93] K. Li, J. Tian, H. Guoyu, R. Xu and Y. Song, "Observation of self-mode-locked noise-like pulses from a net normal dispersion erbium-doped fiber laser", *Laser Phys. Lett.* **14**, 45101 (2017).

[94] A. Boucon, B. Barviau, J. Fatome, C. Finot, T. Sylvestre, M.W. Lee, P. Grelu and G. Millot, "Noise-like pulses generated at high harmonics in a partially-mode-locked km-long Raman fiber laser", *Appl. Phys. B* **106**, 283–287 (2012).

[95] J.M. Dudley, G. Genty, F. Dias, B. Kibler and N. Akhmediev, "Modulation instability, Akhmediev Breathers and continuous wave supercontinuum generation", *Opt. Express* **17**, 21497 (2009).

[96] Q. Lin and G.P. Agrawal, "Raman response function for silica fibers", *Opt. Lett.* **31**, 3086 (2006).

[97] J.M. Dudley and S. Coen, "Numerical simulations and coherence properties of supercontinuum generation in photonic crystal and tapered optical fibers", *IEEE J. Sel. Top. Quantum Electron.* **8**, 651–659 (2002).

[98] J.P. Lauterio-Cruz, *(M.Sc. Thesis) Acoplamiento de Modos Electromagnéticos en Cilindros Metálicos Paralelos* (Universidad de Sonora, México, 2010).